ISBN 91-7874-105-X
LUNFD6/(NFFL-7190)2000

Measurement of azimuthal asymmetries in the hadronic final-state of deep inelastic scattering at HERA.

Thesis Submitted for the Degree of
Doctor of Philosophy in Physics
by

Magnus Lindström

Department of Particle Physics
Lund University

1666

ISBN 91-7874-105-X
LUNFD6/(NFFL-7190)2000

Measurement of azimuthal asymmetries in the hadronic final-state of deep inelastic scattering at HERA.

By due permission of the faculty of mathematics and natural sciences
at Lund University, to be publicly discussed in lecture hall A of the
Department of Physics, December 8, 2000, at 10:15, for the degree of
Doctor of Philosophy
by

Magnus Lindström

Department of Particle Physics
Lund University
Box 118
S-221 00 Lund
Sweden

DOKUMENTDATABLAD enl SIS 61 41 21

Organization LUND UNIVERSITY Department of Physics Box 118 S-221 00 Lund	Document name DOCTORAL DISSERTATION
	Date of issue October 30, 2000
	Sponsoring organization
Author(s) Magnus Lindström	CODEN: LUNDFD6/(NFFL-7190)2000

Title and subtitle

Measurement of azimuthal asymmetries in the hadronic final state of deep inelastic scattering at HERA.

Abstract

Azimuthal asymmetries of the hadronic final state in deep inelastic scattering at HERA provide the opportunity to study the helicity of the interacting particles. We present a theoretical overview of the origin of these effects up to leading order in the strong coupling constant, α_S. A review of previous measurements is given and the results are discussed. The effects of the intrinsic transverse momentum of the partons inside the proton is investigated and implemented into a Monte Carlo program. We develop an analysis method insensitive to the intrinsic transverse momentum, including an unfolding algorithm to correct the data for detector effects.

The result of the measurement is consistent with the expected signal in LO and NLO QCD from the CTEQ-4m parameterization of the structure function in the kinematic region investigated.

Key words:

DIS, jets, azimuthal asymmetries, structure function, unfold

Classification system and/or index termes (if any):

Supplementary bibliographical information:		Language English
ISSN and key title:		ISBN 91-7874-105-X
Recipient's notes	Number of pages	Price
	Security classification	

Distribution by (name and address) Magnus Lindström, Department of Physics,
Box 118, S-221 00 Lund

I, the undersigned, being the copyright owner of the abstract of the above-mentioned dissertation, hereby grant to all reference sources permission to publish and disseminate the abstract of the above-mentioned dissertation.

Signature__________________ Date October 30,2000

Abstract

Azimuthal asymmetries of the hadronic final state in deep inelastic scattering at HERA provide the opportunity to study the helicity of the interacting particles. We present a theoretical overview of the origin of these effects up to leading order in the strong coupling constant, α_s. A review of previous measurements is given and the results are discussed. The effects of the intrinsic transverse momentum of the partons inside the proton is investigated and implemented into a Monte Carlo program. We develop an analysis method insensitive to the intrinsic transverse momentum, including an unfolding algorithm to correct the data for detector effects.

The result of the measurement is consistent with the expected signal in LO and NLO QCD from the CTEQ-4m parameterization of the structure function in the kinematic region investigated.

Contents

1

Introduction and acknowledgments.

To investigate the structure of the proton by scattering electrons on a proton target can be compared to exploring the structure of the sea surface by studying the sun light which is reflected from it. A glassy surface reflects all of the sun light into the eyes of the observer, while a choppy sea reflects almost nothing. We can study how much has been reflected by comparing with a direct observation of the sun and thus determine the structure of the surface. By making a detailed study of the amount of reflected light in different angles as well as an absolute measurement of the intensity we gain more knowledge.

There is, however, one more thing we can look at. Normal sun light is said to be transverse unpolarized, which means that the electromagnetic wave, making up the light, is oscillating in random direction (see fig. 1.1 left). When the light is reflected on the surface there will be some transverse linearly polarized light reflected. This means that the light is oscillating in a specific plane, in the case of the sea it will oscillate horizontally (see fig. 1.1 right). This phenomenon can be dangerous to the eyes and to protect ourselfs we frequently use Polaroid sun glasses, which simply is a vertical raster filtering out the horizontally oscillating light.

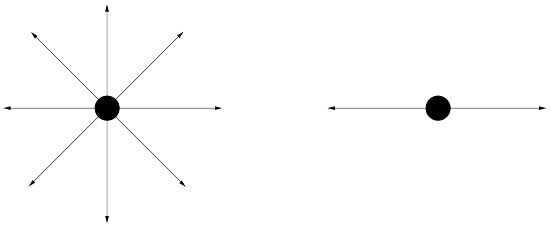

Figure 1.1: Transverse unpolarized light is pictured on the left and transverse linearly polarized light on the right.

The proton is a composite object, consisting of quarks and gluons, whereas the electron according to our present knowledge is elementary. In deep inelastic scattering, highly energetic electrons are used to probe the partonic structure of the proton. The reaction can be described as an exchange of a virtual photon between the electron and one of the constituents of the proton. The exchanged photon can be polarized in the same way as normal light. This polarization can be measured through the azimuthal distributions of the hadronic final state relative the electrons. For these kind of reactions we have an exact theory, perturbative Quantum Chromo Dynamics, describing the features of the reaction including the magnitude of polarization. It will only depend on whether the electron interacts with a quark or a gluon. We will thus be able to add some knowledge about the composition of the proton by determining the ratio of these polarizations.

In contrast to a real photon, which can only be transversely polarized, a virtual photon can also be longitudinally polarized, and therefore we will in addition to the transverse linear polarization also study a polarization related to the longitudinal component.

The thesis is structured as follows:

- Theoretical background; A discussion of semi-inclusive deep inelastic scattering, and the contributions to the polarizations from the leading order QCD processes.
- Previous experiments; Presentation of results, a discussion of non-perturbative contributions to the signal, and of problems arising from QED-corrections to the kinematics which can fake a signal.
- Jets; A description of the jet-definition used and results on the resolution of jet parameters for the relevant kinematic range estimated from a Monte-Carlo simulation, together with a discussion of the effects of acceptance of the detector.
- Hera and H1; A description of the accelerator complex and the H1-detector, and a presentation of the efficiencies and resolutions of the jet parameters on detector level.
- Detector corrections and unfolding; Development of an unfolding algorithm with comparison to bin-to-bin correction.
- The measurement; Comparisons of key distributions for the measured data and the simulated Monte Carlo sample, unfolding of the data to hadron level, and presentation of the final results.

Acknowledgments.

2

Theoretical background.

2.1 Introduction.

In this chapter an overview of the theory behind the azimuthal distributions of the hadronic-final state will be given. It will start with an introduction to deep inelastic scattering (DIS), including definitions of the various structure functions, appearing in the expression for the cross section. After that a review of the QCD-corrections up to first order in the strong coupling constant will be given. In order to illustrate the analogy between the azimuthal distributions and the ratio between the two traditional structure-functions, $R = F_L/2x_BF_T$, the collinear limit will be discussed. Finally, by changing the spin of the gluon, it will be shown that the asymmetries are a consequence of helicity conservation.

2.2 Deep inelastic scattering.

Inclusive deep inelastic scattering of an unpolarized lepton-beam against a proton-target can be written as: $l(e)+p(P) \rightarrow l'(e')+x(X)$. The four-momenta of the incoming lepton (l) and the proton (p) are denoted e and P, respectively, whereas those of the scattered lepton (l') and the hadronic system (x) are e' and X, respectively. This process, is, for a fixed total center-of-mass energy $s = (P+e)^2$, kinematically completely defined by two independent variables[*]. The variables we have chosen are the negative mass-square of the photon and the scaling variable Bjorken x_B, which can be interpreted as the fraction of the proton energy carried by the struck parton in the most basic scattering process.

$$Q^2 = -(e-e')^2 = -q^2 \quad , \quad x_B = \frac{Q^2}{P \cdot q} \tag{2.1}$$

The variable Q^2 is convenient to use since it is inversely proportional to the wavelength of the probe squared. Using these variables the total

---

[*] In the case of unpolarized beams the cross-section is not depending on the azimuthal angle of the scattered lepton.

invariant mass squared of the hadronic system can be expressed as:

$$W^2 = X^2 = (P+q)^2 = M_P^2 + Q^2 \frac{1-x_B}{x_B}, \tag{2.2}$$

where M_P is the rest mass of the proton.

We can distinguish between three different kinds of scattering processes. *Elastic scattering* takes place in the case $W^2 \approx M_P^2$, or in other words if the proton recoils elastically. In *photo production* the wave-length of the probe is comparable or larger than the proton, but the proton can break up and the final-state mass W^2 can be much larger than the proton mass. *Deep inelastic scattering* is defined as [Halzen & Martin 1984]:

$$Q^2 \gg D_P^2 \approx 0.05\, GeV^2 \qquad \text{and} \qquad W^2 \gg M_P^2 \approx 1\, GeV^2 \tag{2.3}$$

where $D_P = \hbar c/d_p$, with $d_p = 1\, fm$ being the size of the proton. The first criterion ensures that the wave-length of the probe is smaller than the proton, and the second that one is far away from the elastic peak. The kinematic regions covered by the previous investigations which are relevant to this analysis, are indicated in fig. 2.1 together with the range comprised by this measurement. Lines in Q^2 and M_P^2 corresponding to multiples of 10 and 100 of D_P^2 and M_P^2, respectively, are also given.

A semi-inclusive DIS event, $l(e) + p(P) \to l'(e') + H(h) + x(X)$, is sketched in fig. 2.2. One final state hadron (H) of four-momentum h is detected. In this case, assuming massless hadrons, we need three more kinematic variables to specify the hadron. We choose the transverse momentum, $p_\perp^{*2}$, of the detected hadron relative to the photon direction and, z, the fraction of the leptonic energy transfer carried by the detected hadron:

$$p_\perp^{*2} = h_+ h_- \quad , \quad z = \frac{P \cdot h}{P \cdot q} \tag{2.4}$$

where $h_\pm$ indicates the light-cone momenta, $E \pm p_z$ along the z-axis. The variables are defined in a system where the photon proceeds along the z-axis. The third variable is ϕ^*, defined as the angle between the lepton-plane and the plane spanned by the detected hadron and the exchanged photon. This variable is here defined using the three-vectors of the leptons and the hadron.

$$\cos\phi^* = \frac{\overline{e} \times \overline{e}'}{\mid \overline{e} \times \overline{e}' \mid} \cdot \frac{\overline{q} \times \overline{h}}{\mid \overline{q} \times \overline{h} \mid}. \tag{2.5}$$

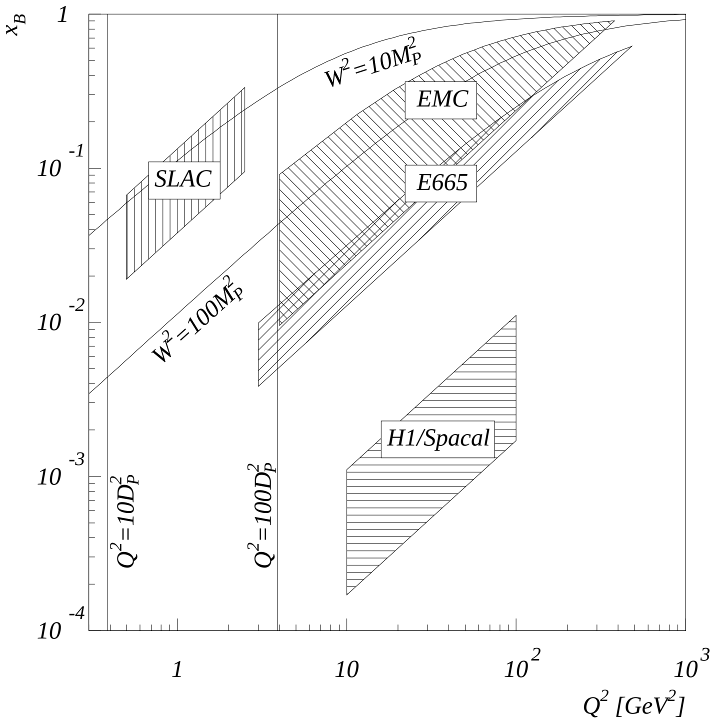

Figure 2.1: The kinematic regions covered by three previous ϕ^* correlation measurements performed at SLAC [Dakin et al. 1972], EMC [Arneodo et al. 1987] and E665 [Adams et al. 1993], together with the acceptance of the H1-Spacal calorimeter which will be used in this analysis. In addition lines where W^2 is a multiple of the proton mass squared M_P^2 and where Q^2 is a multiple of the proton diameter squared D_P^2 are drawn. The DIS-region is the lower right part of the kinematic-plane.

The variables Q^2, x_B and z are invariant under all Lorentz transformations while $p_\perp^{*2}$ and ϕ^* are only invariant when the transformation is performed along the z-axis.

The cross-section for a semi-inclusive process is given by [Levelt & Mulders 1994]

$$\frac{d^5\sigma}{dQ^2 dx_B dp_\perp^{*2} dz d\phi^*} = \frac{4\pi\alpha_{em}^2}{4zQ^4}\mathcal{L}_{\mu\nu}\mathcal{W}^{\mu\nu} \tag{2.6}$$

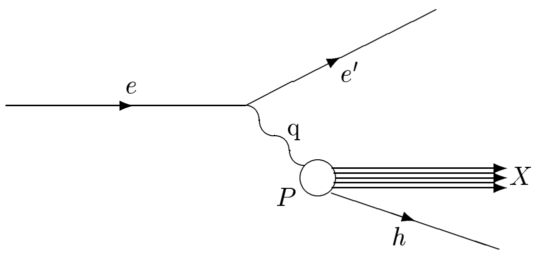

Figure 2.2: A semi-inclusive deep inelastic scattering event, $P + e \rightarrow e' + h + X$, with one detected hadron in the final-state, is sketched in the proton rest-frame.

where $\mathcal{L}_{\mu\nu}$ is the leptonic tensor and $\mathcal{W}^{\mu\nu}$ is the hadronic tensor. These two tensors can be written as functions of $g^{\mu\nu}$ and the independent four-momenta of the process. For the leptonic tensor the momenta are e and e' and for the hadronic tensor they are P^μ, h^μ and q^μ. We will here only consider the special case of neutral boson exchange, far below the Z_0 peak, with unpolarized lepton-beams and protons. The spin-averaged leptonic tensor is then given by [Levelt & Mulders 1994]:

$$\mathcal{L}_{\mu\nu} = 2e_\mu e'_\nu + 2e_\nu e'_\mu - Q^2 g_{\mu\nu}. \tag{2.7}$$

In the hadronic-tensor combinations of the momenta are multiplied with functions W where we have collected everything we do not know about the proton, [Halzen & Martin 1984]. There are 7 possible combinations of the independent four-momenta but the hadronic tensor has to be contracted with the leptonic tensor to obtain the cross-section. This has the consequence that combinations with q^μ have not to be considered since $q^\mu \mathcal{L}_{\mu\nu} = 0$ and therefore these terms give no contribution to the cross section. That leaves us with four linear combinations, $g^{\mu\nu}$ and three combinations of P^μ and h^μ. If we now proceed by choosing the four combinations as $g^{\mu\nu}, P^\mu P^\nu, h^\mu h^\nu$ and $P^\mu h^\nu$[†], we can by visual inspection of the cross section expression note that only combinations containing h^μ will produce a dependence on ϕ^* and it is thus enough to study those. The contraction of $P^\mu h^\nu$ with the leptonic tensor will produce terms proportional to $\cos\phi^*$. As long as we define our vectors in a

---

[†] The hadronic tensor is symmetric in exchanging μ and ν, so the last combination is technically a sum of two, but for the reasoning here we only consider one of them.

system where the photon and proton collide head-on we have $e^*_\perp = e'^*_\perp$, and the two first terms in eq. 2.7 will both contain terms $e^*_\perp p^*_\perp \cos\phi^*$. The contraction of $h^\mu h^\nu$ will produce terms proportional to $e^*_\perp p^*_\perp \cos\phi^*$ and terms proportional to $e^{*2}_\perp p^{*2}_\perp \cos^2\phi^* = e^{*2}_\perp p^{*2}_\perp \frac{1}{2}(1+\cos 2\phi^*)$. The cross-section can thus be written as a Fourier cosine-series with three terms, i.e. $d\sigma = a_0 + a_1\cos\phi^* + a_2\cos 2\phi^*$. The factors $e^*_\perp p^*_\perp$ and $e^{*2}_\perp p^{*2}_\perp$ will be discussed later in this chapter when we analyze the contributions to the structure-functions

Writing the hadronic tensor in terms of photon polarizations, at least one of the terms in the Fourier series has to be written as a sum of two polarizations. It is then natural to split the constant term, a_0, in the transverse and the longitudinal polarizations [Levelt & Mulders 1994].

$$\begin{aligned} \mathcal{W}_T &= \frac{1}{2}\left(\epsilon_x \cdot \mathcal{W} \cdot \epsilon_x + \epsilon_y \cdot \mathcal{W} \cdot \epsilon_y\right) & (2.8) \\ \mathcal{W}_L &= \epsilon_L \cdot \mathcal{W} \cdot \epsilon_L \propto p^{*2}_\perp & (2.9) \end{aligned}$$

where the indices T and L refer to the polarization of the virtual photon, where T is the unpolarized transverse and L is longitudinal state. The two polarizations projecting $\cos\phi^*$ and $\cos 2\phi^*$ out of the hadronic tensor are the transverse linear (TT) for $\cos 2\phi^*$ and the interference between longitudinal and transverse photons (LT) for $\cos\phi^*$ [Levelt & Mulders 1994].

$$\begin{aligned} \mathcal{W}_{LT}\cos\phi^* &= -\left(\epsilon_x \cdot \mathcal{W} \cdot \epsilon_L + \epsilon_L \cdot \mathcal{W} \cdot \epsilon_x\right) \propto p^*_\perp \cos\phi^* & (2.10) \\ \mathcal{W}_{TT}\cos 2\phi^* &= \frac{1}{2}\left(\epsilon_x \cdot \mathcal{W} \cdot \epsilon_x - \epsilon_y \cdot \mathcal{W} \cdot \epsilon_y\right) \propto p^{*2}_\perp \cos 2\phi^* & (2.11) \end{aligned}$$

Considering the semi-inclusive structure-functions we define them such that they after integration over the hadronic variables $p^{*2}_\perp, z$ and ϕ^*, can be immediately interpreted in terms of the inclusive structure-functions F_i. The phase-space factor $(d^3h/2h_0 \approx dz dp^{*2}_\perp d\phi^*/4z$ in the deep-inelastic limit) is included in the structure-functions.

$$\begin{aligned} \tilde{F}_1 &= \tilde{F}_T = \frac{1}{4z} M_P \mathcal{W}_T & (2.12) \\ \frac{\tilde{F}_2}{2\,x_B} - \tilde{F}_1 &= \frac{\tilde{F}_L}{2\,x_B} = \frac{1}{4z} M_P \mathcal{W}_L & (2.13) \\ \tilde{F}_4 &= \tilde{F}_{LT} = \frac{1}{4z} M_P \mathcal{W}_{LT} & (2.14) \\ \tilde{F}_6 &= \tilde{F}_{TT} = \frac{1}{4z} M_P \mathcal{W}_{TT} & (2.15) \end{aligned}$$

Thus, an integration over all hadrons results in the inclusive definition of the structure functions (F_i) times the average number of hadrons, $\langle n_h(Q^2,x_B)\rangle$, produced at (Q^2,x_B) [Levelt & Mulders 1994].

$$\langle n_h(Q^2,x_B)\rangle F_i(Q^2,x_B) = \int dz dp_\perp^{*2} d\phi^* \tilde{F}_i(Q^2,x_B,z,p_\perp^{*2}) \tag{2.16}$$

$$where \quad i = \begin{cases} 1,2,4,6 \\ or \\ L,T,LT,TT \end{cases}$$

The semi-inclusive neutral-current cross-section, for unpolarized beams and targets, can then be written in terms of the structure-functions $\tilde{F}_i$ [Hagiwara, Hikasa & Kai 1983, Levelt & Mulders 1994]

$$\frac{d^5\sigma}{dQ^2 dx_B dp_\perp^{*2} dz d\phi^*} = \kappa\, [\underbrace{(1+(1-y_B)^2)\tilde{F}_T + 2\,(1-y_B)\frac{\tilde{F}_L}{2\,x_B}}_{a_0/\kappa} +$$

$$\underbrace{\sqrt{1-y_B}(2-y_B)\tilde{F}_{LT}}_{a_1/\kappa}\cos\phi^* + \underbrace{2(1-y_B)\tilde{F}_{TT}}_{a_2/\kappa}\cos 2\phi^*] \tag{2.17}$$

where y_B is the energy fraction of the electron energy carried by the exchanged photon in the rest frame of the proton.

$$\kappa = \frac{4\pi\alpha_{em}^2}{Q^4}\ ,\ y_B = \frac{Q^2}{s\,x_B} = \frac{P\cdot q}{P\cdot e}. \tag{2.18}$$

We will, in this chapter, discuss the results in two different ways. In the first a detailed analysis of these structure-functions will be made, and in the second the more practical view, where the cross-section is seen as a Fourier-expansion which leads to the observable modulations in ϕ^*, will be taken. If we consider $d\sigma = a_0 + a_1\cos\phi^* + a_2\cos 2\phi^*$, it is common to present the results as the mean values $\langle\cos\phi^*\rangle$ and $\langle\cos 2\phi^*\rangle$. To calculate these averages we need the norm $\int d\sigma d\phi^* = 2\pi a_0$ and the first moments of the observables, i.e. $\int d\sigma\cos\phi^* d\phi^* = \pi a_1$ and $\int d\sigma\cos 2\phi^* d\phi^* = \pi a_2$. The averages are then:

$$\langle\cos\phi^*\rangle = \frac{a_1}{2\,a_0} \qquad \text{and} \qquad \langle\cos 2\phi^*\rangle = \frac{a_2}{2\,a_0}. \tag{2.19}$$

The individual structure-functions will be reviewed up to first order in α_s, but the main emphasis of this thesis is on the measurement of the averages in eq. 2.19.

2.3 Historical background.

Already in 1965 azimuthal distributions were discussed by Jones in connection with lepton nucleon scattering where one pion was detected, $N + e \to N' + e' + \pi$ [Jones 1965]. Here the angular distribution was calculated in terms of the matrix element as given by the leptonic and hadronic tensors, much in the same way as has been presented above. By inserting the helicity formalism into the matrix element the contributions from final states of different spin and parity to the angular distribution of pions were extracted.

In 1972, Ravndal treated the same topic now based on the structure functions and their relations [Ravndal 1973]. His article was written as a comment to Callan and Gross's findings concerning the relation between the longitudinal and transverse cross-sections [Callan & Gross 1969]. In the naive quark parton model F_L is identical to zero i.e. the photon is interacting with a point-like spin 1/2 constituent of the proton, and no further processes takes place. If this constituent emits one or more spin 1 particles in a bremsstrahlung process, as described by QCD and QED, F_L would get a non-zero value. Ravndal pointed out that the bremsstrahlung process would produce a non-zero value also for $\tilde{F}_{LT}$ and $\tilde{F}_{TT}$. He furthermore pointed out that the structure of $\tilde{F}_{LT}$ and $\tilde{F}_{TT}$ is very similar to $\tilde{F}_L$. We will later study the collinear limit of the cross-section to check this statement.

During the 70's QCD was formulated in it's current form. The basic idea of QCD follows the theory of QED in which the interaction between spin 1/2 fermions, carrying electric-charge, takes place via the exchange of a photon, which is a spin 1 bosons without electric charge. In QCD the interaction between fermions carrying colour charge is described. This interaction is mediated by gluons which themselves carry colour charge and therefore may couple to each other e.g. $g \to g + g$. The fact that the force mediator in QED does not carry electric charge whereas the force mediators in QCD do carry colour charge, is the reason for the different properties of the electro-magnetic- and the strong-force.

In the early 80's, when QCD was an established theory a number of articles concerning the perturbative treatment of leading order processes in α_s where written. The most elaborate was by presented Hagiwara et al. where a complete treatment of polarized beams and γ, Z^0 and $W^\pm$ exchange is done [Hagiwara et al. 1983]. In the following we restrict the discussion to γ exchange for unpolarized beams. Using deep inelastic eP scattering to investigate the proton there are two leading order processes: A quark, stemming from the proton, interacts with the virtual photon and emits QCD bremsstrahlung (QCD-Compton), or a gluon splitting in a quark and an anti-quark from which one is interacting with the photon (Boson-gluon-fusion or in shorthand BGF). Both of these processes produces a non-zero $p_\perp^*$ of the hadron which will result in contributions to $\tilde{F}_{LT}$ and $\tilde{F}_{TT}$. The QCD specific process, $g \rightarrow g + g$, only occurs in next to leading order calculations since one of the gluons will have to split in a quark anti-quark pair in order to interact with the photon, $\gamma + g \rightarrow q + \bar{q} + g$, and we will not treat this case except for using a numerical NLO-calculation to estimate the total effect of NLO QCD [Catani & Seymour 1997]. It is also worth mentioning that an approximative treatment of the higher-orders in α_s was done by I. Knowles using a parton shower approach introducing spin-density matrices [Knowles 1988], where the helicity is conserved for up to five final-state partons.

In 1994 Levelt and Mulders discussed azimuthal asymmetries due to non-perturbative effects using twist calculations [Levelt & Mulders 1994]. This work has been followed up during the 90' [Mulders & Tangerman 1996, Boer, Jakob & Mulders 1999] with an emphasis on experiments using polarized beams and targets. There is a way of estimating the effects of the twist using the intrinsic $p_\perp^*$ of the partons in the proton. This turns out to be a special case of the calculation of Levelt and Mulders.

The contributions to the structure functions are depending on the spin of the participating partons. So far, we have only considered processes where one parton from the proton is participating in the hard scattering, but it is of course possible to have processes with multi parton interaction. One example is diffractive scattering for which there exist alternative models to describe the interaction. One- and two gluon exchange has been calculated, [Bartels, Ewerz, Lotter, Wusthoff & Diehl 1995], and it was predicted that $\tilde{F}_{TT}$ for two gluon exchange would have opposite sign to that of one gluon exchange. Thus, a measurement of the average azimuthal dependence would provide a strong test of such models.

2.4 Contributions to the structure-functions in zeroth order in α_s.

In order to calculate the contributions to the individual structure-functions in eqs. 2.12-2.15 we will take the complete matrix-elements from the literature and expand those in the kinematic variables. We then proceed to identify the contributions in the expansion by comparing the kinematic factors involving y_B in front of the structure-functions in eq. 2.17.

These calculations are most easily carried out in the Breit-frame which is defined by

$$P = \frac{\sqrt{Q^2}}{2\,x_B}\,(1,0,0,1)\,, \qquad q = \left(0,0,0,-\sqrt{Q^2}\right). \tag{2.20}$$

This frame is reached from the proton rest frame, fig. 2.2, through a boost along the photon-axis, and is thus not changing any of the definitions given above. The Breit-system four-vectors of the leptons and partons are listed in appendix A.

Using this reference frame, DIS processes of zeroth order in α_s, $l(e)+q(p_i) \to l'(e')+q(p_f)$, can be described as a head on collision between the virtual photon and the interacting parton. The four-momentum of the incoming parton is $p_i = x_b P = \frac{\sqrt{Q^2}}{2}\,(1,0,0,1)$ and that of the outgoing is $p_f = p_i + q = \frac{\sqrt{Q^2}}{2}\,(1,0,0,-1)$. Thus, the momenta of the incoming and outgoing partons are of the same magnitude but they are oppositely directed, which is the reason why the Breit-system is also known as the brick-wall frame.

According to [Ellis, Stirling & Webber 1996] the cross-section can be written as:

$$\frac{d^5\sigma}{dQ^2 dx_B dp_\perp^{*2} dz d\phi^*} = \Gamma \sum_i \delta(p_\perp^{*2})\delta(1-z)\delta(\phi^*) f_i(x_B,Q^2) \times |\overline{\mathcal{M}_2}|^2 \tag{2.21}$$

with

$$\Gamma = \frac{y_B^2}{16\pi\,Q^4} \tag{2.22}$$

and the matrix-element

$$|\overline{\mathcal{M}_2}|^2 = 32\pi^2 e_q^2 \alpha_{em}^2 \frac{(p_i \cdot e)^2 + (p_i \cdot e')^2}{(e \cdot e')^2}. \tag{2.23}$$

Using the four-vector expressions from appendix A renders the standard result

$$\frac{d^5\sigma}{dQ^2 dx_B dp_\perp^{*2} dz d\phi^*} = \frac{4\pi\alpha_{em}^2}{Q^4} \sum_i \delta(p_\perp^{*2})\delta(1-z)\delta(\phi^*) \times \frac{e_q^2}{2} f_i(x_B,Q^2)(1+(1-y_B)^2) \tag{2.24}$$

where the parton-density $f_i(x_B, Q^2)$ is the probability to find a parton i carrying a fraction x_B of the proton momentum at the four-momentum transfer squared Q^2. The cross-section is independent of ϕ^*. Comparing with eq. 2.17 tell that only $\tilde{F}_T$ gets contributions in this order. The ϕ^* dependence, and thus the contributions to the other three structure-functions, only appears in higher-order processes.

Calculations of the zeroth order process will be revived in chapter 3, where the intrinsic Fermi motion of partons inside the proton will be included.

2.5 Corrections to the cross-section from leading order α_s processes.

Leading order contributions to the DIS cross section come from boson-gluon-fusion processes $e^+(e) + g(k) \to e^+(e') + \bar{q}(p_1) + q(p_2)$ and QCD-Compton scattering $e^+(e) + q(p_1) \to e^+(e') + q(p_2) + g(k)$, which usually are calculated separately. If we, however, notice that the matrix-elements for these processes can be derived from $e^-(e) + e^+(e') \to \bar{q}(p_1) + q(p_2) + g(k)$, shown in fig. 2.3, by using crossing symmetry[‡] we can shorten the calculation [Seymour 1995]. Thus we need to redefine the incoming positron as an outgoing electron, and in the BGF case the outgoing gluon as an incoming gluon whereas for QCD-Compton the outgoing anti-quark is redefined as an incoming quark.

In leading order processes the variable x_B no longer corresponds to the fractional parton momentum in the proton but is related to the parton momentum at the photon vertex after additional parton emission. In this case it is convenient to use the partonic scaling variable x_p to make the final cross-section expression shorter.

$$x_p = \frac{Q^2 z(1-z)}{p_\perp^{*2} + Q^2 z(1-z)} \tag{2.25}$$

The fractional energy carried by the struck parton, x_B/x_p, eq. A.7 can now be larger than x_B.

The cross-section can be written [Seymour 1995]:

$$\frac{d^5\sigma}{dQ^2 dx_B dp_\perp^{*2} dz d\phi^*} = \Gamma_3 \sum_i f_i\left(\frac{x_B}{x_p}, Q^2\right) \times |\overline{\mathcal{M}_3}|^2/N \tag{2.26}$$

[‡] I.e. CPT-invariance, which allows any incoming particle to be redefined as an outgoing anti-particle or vise versa

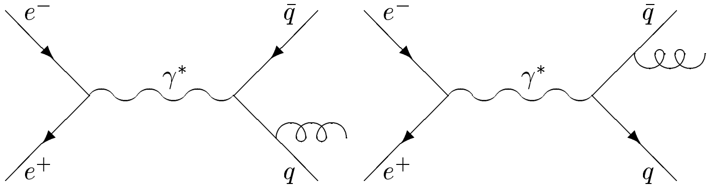

Figure 2.3: The tree-level diagrams for electron-positron annihilation $e^+(e)+e^-(e') \to \bar{q}(p_1)+q(p_2)+g(k)$. The corresponding DIS diagrams, $e^+(e)+q(-p_1) \to e^+(-e')++q(p_2)+g(k)$ and $e^+(e)+g(-k) \to e^+(-e')+\bar{q}(p_1)+q(p_2)$, can be derived using crossing-symmetries.

where

$$\Gamma_3 = \frac{1}{128(2\pi)^4}\frac{y_B^2}{Q^2}\frac{1}{p_\perp^{*2}+Q^2z(1-z)}, \tag{2.27}$$

and the matrix-element

$$|\overline{\mathcal{M}_3}|^2 = 24C_F e_q^2 e^4 g_s^2 \frac{(p_1\cdot e)^2+(p_1\cdot e')^2+(p_2\cdot e)^2+(p_2\cdot e')^2}{(e\cdot e')(p_1\cdot k)(p_2\cdot k)} \tag{2.28}$$

N being the DIS colour averaging factor (3 for Compton scattering, and 8 for BGF).

Inserting the Breit frame four-vectors from appendix A and separating out the factor κ in front of eq. 2.17 leads to:

$$\frac{d^5\sigma}{dQ^2dx_Bdp_\perp^{*2}dzd\phi^*} = \frac{4\pi\alpha_{em}^2}{Q^4}\sum_i \frac{e_q^2}{2} f_i\left(\frac{x_B}{x_p},Q^2\right)\frac{\alpha_s}{4\pi^2}\frac{1}{d} \times K_i \tag{2.29}$$

where the phase-space factor is

$$d = p_\perp^{*2} + Q^2z(1-z) \tag{2.30}$$

and the $K_{i=b,c}$'s for BGF and QCD-Compton, respectively, contains the pieces of the cross-section which the two processes do not have in common. They are separately calculated, again using the four-vectors in appendix A.

For convenience the four vectors used will now be denoted v_{in},v_1 and v_2 (see appendix A), corresponding to the incoming and the two outgoing partons, respectively. Where both processes can be written as $e + v_{in} = e' + v_1 + v_2$. For BGF v_{in} is the incoming gluon and v_1 and v_2 are the outgoing quark and anti-quark. For QCD-Compton v_{in} is the incoming quark, v_1 is the outgoing gluon and v_2 is the outgoing quark.

For boson gluon fusion this renders the following expression for K_b:

$$K_b = \frac{y_B^2}{2} \frac{(v_1 \cdot e)^2 + (v_1 \cdot e')^2 + (v_2 \cdot e)^2 + (v_2 \cdot e')^2}{(v_1 \cdot v_{in})(v_2 \cdot v_{in})} \tag{2.31}$$

If we now consider the Breit system we know that the two leptons, the incoming and outgoing, have the same transverse momentum and we define them as being in the xz-plane. The third term can be expanded as follows:

$$\begin{aligned}
(v_2 \cdot e)^2 &= ((v_{02}^*, v_{\perp 2}^* \cos\phi^*, v_{\perp 2}^* \sin\phi^*, v_{z2}^*) \cdot (e_0^*, e_\perp^*, 0, e_z^*))^2 = \\
&= ([v_{02}^* e_0^* - v_{z2}^* e_z^*] - v_{\perp 2}^* e_\perp^* \cos\phi^*)^2 = \\
&= [v_{02}^* e_0^* - v_{z2}^* e_z^*]^2 - 2[v_{02}^* e_0^* - v_{z2}^* e_z^*] v_{\perp 2}^* e_\perp^* \cos\phi^* + \\
&\qquad\qquad v_{\perp 2}^{*2} e_\perp^{*2} \cos^2\phi^* = \\
&= \left([v_{02}^* e_0^* - v_{z2}^* e_z^*]^2 + \frac{1}{2} v_{\perp 2}^{*2} e_\perp^{*2}\right) - \\
&\quad 2[v_{02}^* e_0^* - v_{z2}^* e_z^*] v_{\perp 2}^* e_\perp^* \cos\phi^* + \frac{1}{2} v_{\perp 2}^{*2} e_\perp^{*2} \cos 2\phi^*
\end{aligned}$$

We further know that the momenta of the two quarks, v_1^* and v_2^*, must balance,.i.e $v_{x1}^* = -v_{x2}^* = -v_{\perp 2}^* \cos\phi^*$ and $v_{y1}^* = -v_{y2}^* = -v_{\perp 2}^* \sin\phi^*$. All of the squared scalar-products in the nominator of the matrix element can thus be written in the general form $a_0' + a_1' \cos\phi^* + a_2' \cos 2\phi^*$ where ϕ^* is the azimuthal opening angle between the quark and the lepton. It is consequently possible to write K_b in the following way:

$$K_b = k_b(b_0 + b_1 \cos\phi^* + b_2 \cos 2\phi^*) \tag{2.32}$$

with

$$k_b = \frac{2z(1-z)}{d^2}. \tag{2.33}$$

The full expressions for the factors, $b_{0,1,2}$, are rather lengthy so we will here just notice that the expression for K_b had the predicted form. The full expressions can be found in appendix B. In order to simplify the expressions and make an interpretation possible, the collinear limit will be taken in the next section and some interesting features of these equation will then be pointed out.

For QCD-Compton scattering the factor K_c can be written

$$K_c = \frac{4y_B^2}{3}\frac{(v_{in}\cdot e)^2 + (v_{in}\cdot e')^2 + (v_2\cdot e)^2 + (v_2\cdot e')^2}{(v_1\cdot v_{in})(v_1\cdot v_2)} \tag{2.34}$$

where, in the Breit frame, the incoming quark, v_{in}, is collinear with the proton and is thus independent of the azimuthal angle. Only the two terms containing v_2 are depending of ϕ^*. This means that we have two constant terms and two which, just as for BGF, can be written as $a'_0 + a'_1 \cos\phi^* + a'_2 \cos 2\phi^*$, and that the matrix-element also in this case can be written in the expected form:

$$K_c = k_c(c_0 + c_1 \cos\phi^* + c_2 \cos 2\phi^*) \tag{2.35}$$

where

$$k_c = \frac{16z^2(1-z)}{3p_\perp^{*2}d}. \tag{2.36}$$

The expressions for the mean values $\langle\cos\phi^*\rangle$ and $\langle\cos 2\phi^*\rangle$ can, in terms of these variables, be written as (neglecting the zeroth order contributions to $\tilde{F}_T$):

$$\langle\cos\phi^*\rangle = \frac{1}{2}\frac{f_g k_b b_1 + \sum_q f_q k_c c_1}{f_g k_b b_0 + \sum_q f_q k_c c_0} \tag{2.37}$$

$$\langle\cos 2\phi^*\rangle = \frac{1}{2}\frac{f_g k_b b_2 + \sum_q f_q k_c c_2}{f_g k_b b_0 + \sum_q f_q k_c c_0} \tag{2.38}$$

where the parton densities f_g and f_q are functions of x_B/x_p and Q^2. This result is independent of the strong-coupling constant, which only enters in higher order processes where it just contribute a correction while the dependence on the parton-densities is retained. Thus a measurement of these moments provides a linear independent way of obtaining the parton-densities of the proton with only a second order dependence on the coupling constant. The sensitivity to the gluons and quarks, respectively, is of course depending on the exact shape of the factors k, b and c as a function of the kinematic variables and we will investigate that in the next section.

2.6 Leading-order corrections in the collinear limit.

We would now like to simplify the expressions for the leading-order corrections obtained above, but preferably in a way where we can separate

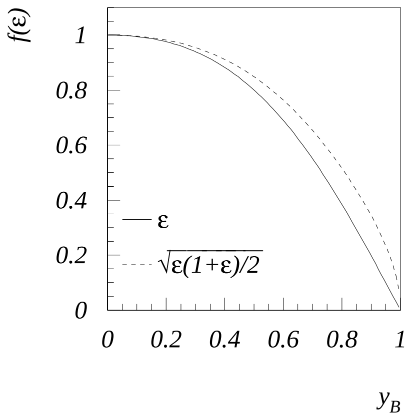

Figure 2.4: The kinematic factors $\sqrt{\varepsilon(1+\varepsilon)/2}$ (dashed line) and ε (full line) in the expressions for $\langle\cos\phi^*\rangle$ and $\langle\cos 2\phi^*\rangle$, respectively, as function of y_B.

out the $p_\perp^{*2}$ dependence since we already obtained such factors when we contracted the hadronic- with the leptonic-tensor. It turns out that in the collinear limit, given by $z \to 1$, this is fulfilled.

If we take the collinear limit of the explicit expressions for the matrix elements in eqs. B.2-B.6, and identify the contributions using the kinematic factors in eq. 2.17 we reach the following leading-order corrections to the structure-functions:

$$\tilde{F}_T = \kappa\frac{Q^2}{p_\perp^{*2}}\left(\frac{1-x_p}{2x_p}(x_p^2+(1-x_p)^2)f_g+\sum_q\frac{4}{3}\frac{1+x_p^2}{x_p}f_q\right) \quad (2.39)$$

$$\frac{\tilde{F}_L}{2x_B} = \kappa\left(4x_p(1-x_p)f_g+\sum_q\frac{16}{3}x_pf_q\right) \quad (2.40)$$

$$\tilde{F}_{LT} = -\kappa\frac{Q}{p_\perp^*}\left(2(1-x_p)(2x_p-1)f_g+\sum_q\frac{16}{3}x_pf_q\right) \quad (2.41)$$

$$\tilde{F}_{TT} = \kappa\left(2x_p(1-x_p)f_g+\sum_q\frac{8}{3}x_pf_q\right) \quad (2.42)$$

where we have collected the electric charge, coupling constant, phase-space factors and various constants in κ.

$$\kappa = \frac{e_q^2}{2}\frac{\alpha_s}{4\pi^2}\frac{1}{d} \tag{2.43}$$

The $p_\perp^{*2}$ dependence has for convenience been separated out of the expressions for the structure functions.

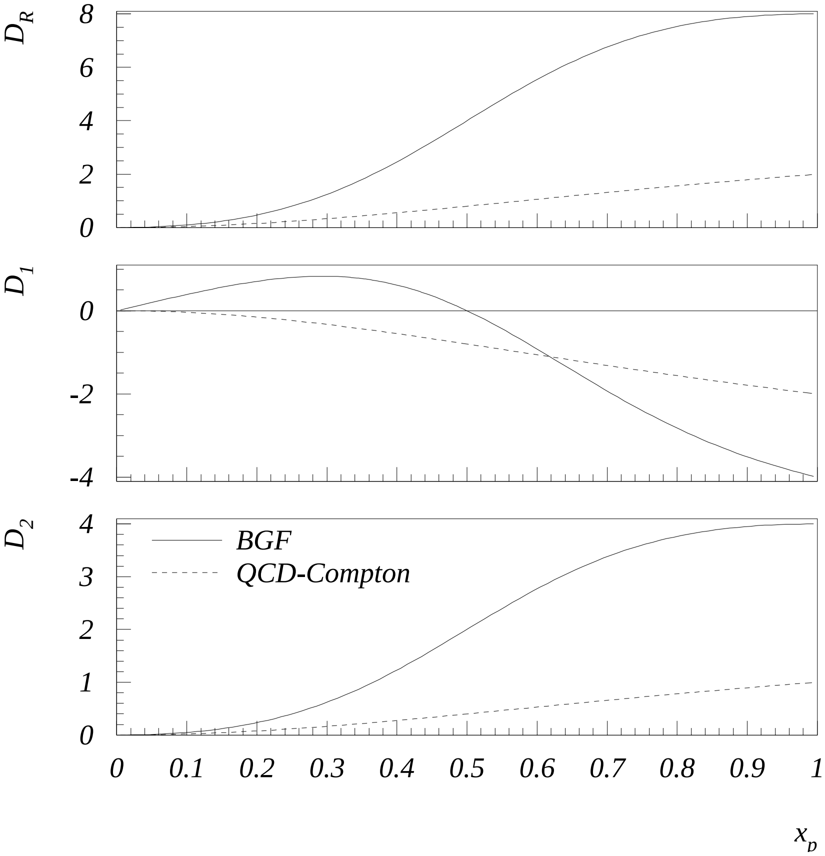

Figure 2.5: The functions D_R, D_1 and D_2 versus x_p, plotted separately for gluons (full line) and quarks (dashed line).

The calculation of $R = \tilde{F}_L/2x_B\tilde{F}_T$ is straight-forward using the above expressions while the calculation of $\langle\cos\phi^*\rangle$ and $\langle\cos 2\phi^*\rangle$ requires some considerations. The observable $\langle\cos\phi^*\rangle$ is the fraction of the first term in the Fourier expansion divided with two times the zeroth term (see eq. 2.19). This means that the nominator is $\tilde{F}_{LT}$ times the kinematic factor $(2-y_B)\sqrt{1-y_B}$ (see eq. 2.17), and the denominator is two times the sum of $\tilde{F}_T$ and $\tilde{F}_L$ multiplied by their respective kinematic factors. $\tilde{F}_L$ is much smaller than $\tilde{F}_T$ if $p_\perp^{*2}$ is small compared to Q^2 and we will therefore neglect it in the calculations here. The resulting expression for $\langle\cos\phi^*\rangle$ then becomes just the ratio of $\tilde{F}_{LT}$ and $\tilde{F}_T$ multiplied by the fraction of the kinematic factors. In the same way an approximate expression can be obtained for $\langle\cos 2\phi^*\rangle$ giving a ratio of $\tilde{F}_{TT}$ and $\tilde{F}_T$. If we collect the partonic scaling variable x_p and the parton-densities f_i in the functions D_R, D_1 and D_2 we can write R ,$\langle\cos\phi^*\rangle$ and $\langle\cos 2\phi^*\rangle$ in the following way:

$$R = \frac{p_\perp^{*2}}{Q^2}\, D_R(f_i, x_p) \tag{2.44}$$

$$\langle\cos\phi^*\rangle = \frac{\sqrt{\varepsilon(1+\varepsilon)/2}}{2}\, \frac{p_\perp^*}{Q}\, D_1(f_i, x_p) \tag{2.45}$$

$$\langle\cos 2\phi^*\rangle = \frac{\varepsilon}{2}\, \frac{p_\perp^{*2}}{Q^2}\, D_2(f_i, x_p) \tag{2.46}$$

with

$$\varepsilon = \frac{2(1-y_B)}{1+(1-y_B)^2} \tag{2.47}$$

The equations now contain a kinematic factor, depending on y_B, a factor depending on $p_\perp^{*2}$, and finally a function D describing how the individual observable varies as a function of the parton densities and x_p.

In fig. 2.4 it can be seen that the kinematic factors vary from 1 at low y_B to zero at high y_B. These factors stem from the contraction of the tensors we did earlier and are not process dependent.

The $p_\perp^{*2}$-factor is $p_\perp^*/Q$ for $\langle\cos\phi^*\rangle$ and $p_\perp^{*2}/Q^2$ for $\langle\cos 2\phi^*\rangle$. These can also be found in the tensor equations and are common for the different partons (quarks and gluons).

The disparity between different partons are contained in the D functions, where contrasting behavior will be seen depending on the spin of the participating particles. The explicit expressions for these functions can be found in appendix B. In fig. 2.5 we have separated quarks and gluons, i.e. setting $f_g = 1$ and $f_q = 0$ for the gluon curves and vice versa for the quark curves. It can be seen that gluons and quarks show quite different behaviors, especially for $\langle \cos\phi^* \rangle$ where the gluons even changes sign at $x_p = 0.5$.

The similar structure of $\tilde{R}$, $\langle \cos\phi^* \rangle$ and $\langle \cos 2\phi^* \rangle$ is emphasized by the observation that in leading order the following relation holds: $\tilde{F}_L/2x_B = 2\tilde{F}_{TT}$. This is however due to a degeneracy of the matrix-element,[Kramer 2000], and is not true when higher order corrections are added.

2.7 Helicity conservation.

To confirm that the underlying reason for the azimuthal asymmetries really is helicity conservation, a simple test is to change the spin of one of the participating partons.

From [Plehn 1998] the matrix-element for $e^+(e) + e^-(e') \to \bar{q}(p_1) + q(p_2) + g(k)$ for scalar gluons is

$$|\overline{\mathcal{M}_3}|^2 = 24 C_F e_q e^4 \frac{(k \cdot e)^2 + (k \cdot e')^2}{(e \cdot e')(p_1 \cdot k)(p_2 \cdot k)}. \tag{2.48}$$

As explained in section 2.5 crossing-symmetries can be used to derive the BGF process $e^+(e) + g(k) \to e'^+(e) + \bar{q}(p_1) + q(p_2)$:

$$|\overline{\mathcal{M}_3}|^2_{BGF} \propto \frac{(v_{in} \cdot e)^2 + (v_{in} \cdot e')^2}{(v_1 \cdot v_{in})(v_2 \cdot v_{in})}. \tag{2.49}$$

If we now follow the reasoning in section 2.5, where we deduced the contributions from BGF for vector gluons, and look at the terms in the nominator we can see that, since the gluon is collinear with the proton, none of the terms will exhibit any ϕ^* dependence. If we insert the four-vectors from appendix A we get the explicit factors:

$$b_0 = 2\,(e_0^{*2} + e_z^{*2})\,p_{zi}^{*2} \tag{2.50}$$

$$= (1 + (1 - y_B)^2)\,Q^2 p_{zi}^{*2} \tag{2.51}$$

$$b_1 = 0 \tag{2.52}$$

$$b_2 = 0 \tag{2.53}$$

Looking at the kinematic factor and compare to eq. 2.17 we see that only the transverse structure-function $\tilde{F}_T$ gets a contribution, and there is no dependence on ϕ^* at all.

This demonstrates that the azimuthal asymmetries are related to the helicities of the partons participating in the scattering process.

2.8 Monte Carlo models.

We will in the rest of this thesis make extensive use of Monte Carlo models. In the next chapter such models are used for comparison to previous experimental results and in chapter 4 to develop an analysis method. In chapter 5 and chapter 7 they will first be used to unfold the data to hadron-level and then for a comparison with the final results.

The models which have been used to simulate deep inelastic scattering are the so-called MEPS (matrix-element with parton-shower) models. They are based on calculations of the exact matrix-elements up to leading order in α_s with the addition of parton-showers to approximate the contribution from higher-order α_s processes [Sjöstrand 1994]. In order to produce final-state-hadrons they use the Lund string fragmentation [Sjöstrand 1994]. The Monte Carlo generators which we used also contains an interface to a program which provides calculations of QED corrections[Kwiatkowski, Spiesberger & Mohring 1992, Charchula, Schuler & Spiesberger 1994]. This includes virtual-corrections to the photon-vertex as well as the possibility to emit one extra real photon.

The two models we will use are Lepto 6.5 [Ingelman, Edin & Rathsman 1997] and Rapgap 2.06 [Jung 1995]. The main difference is that Rapgap in addition allows for the possibility to use experimental fits to diffractive data and is therefore the main choice for the H1 collaboration, whereas we have implemented a number of modifications in Lepto, like the inclusion of the Fermi-motion in the proton. We will use Rapgap to correct for detector effects and Lepto for comparison and interpretation of the result.

For the detailed final comparison with data a second-order α_S calculation (NLO) will be used [Catani & Seymour 1997]. It contains one-loop virtual corrections and the possibility to emit one extra parton to produce a three parton final-state. It does, however, not contain any non-perturbative hadronization.

Details about the parameters and settings used in the different programs are listed in appendix C.

2.9 Summary.

We have calculated the cross-section for semi-inclusive deep inelastic scattering where we found that, in a system where the proton and the photon collide head-on, it can be written as a Fourier cosine-series with three terms: $d\sigma = a_0 + a_1 \cos\phi^* + a_2 \cos 2\phi^*$ (eq. 2.17), where ϕ^* is the azimuthal opening angle between the detected hadron and the lepton-plane. The first term, a_0 is a function of the traditional transverse- and longitudinal structure-functions, whereas the second and third term can be written as:

$$a_1 = \sqrt{1 - y_B)}(2 - y_B)\tilde{F}_{LT} \qquad (2.54)$$

$$a_2 = (1 - y_B)\tilde{F}_{TT} \qquad (2.55)$$

where $\tilde{F}_{LT}$ is the interference between longitudinal and transverse photons and $\tilde{F}_{TT}$ is the transverse linear polarization. We furthermore found that $\tilde{F}_{LT}$ and $\tilde{F}_{TT}$ are non-zero only beyond zeroth order in α_s.

We investigated the observable azimuthal asymmetries:

$$\langle \cos\phi^* \rangle = \frac{a_1}{2\,a_0} \qquad (2.56)$$

$$\langle \cos 2\phi^* \rangle = \frac{a_2}{2\,a_0} \qquad (2.57)$$

and found that they are sensitive to the parton-densities in leading-order in α_s, while the value of the strong coupling itself only effects them in higher orders.

In the rest of this thesis we will concentrate on the asymmetries and first investigate previous measurements of them, before we develop an analysis method suited to our detector.

3

Previous measurements.

3.1 Fixed target experiments.

Three previous measurements of the ϕ^*-asymmetries have been performed by fixed target experiments. The kinematic regions covered by these are displayed in fig. 2.1. No signal was observed by the SLAC [Dakin et al. 1972] experiment whereas the two $\mu^{\pm}P$ scattering experiments, EMC [Arneodo et al. 1987] and E665 [Adams et al. 1993], both concluded that the signal measured could not be explained by perturbative QCD alone. Instead it was interpreted as an effect of the intrinsic momentum, $p_\perp$, of the partons inside the proton.

In this chapter the measurement of the E665 experiment will be discussed by implementing the intrinsic $p_\perp$ in a Monte Carlo model and tuning it to fit the E665 results. The contribution from QED-effects will also be estimated.

3.2 The measurement from E665.

The E665 experiment used a 490 GeV μ-beam on proton and deuterium targets to measure the structure of protons and neutrons. Deep inelastic scattering events used in the ϕ^*-asymmetry analysis were selected according to the following criteria:

$$\begin{array}{ccccc}
300\ GeV^2 & < & W^2 & < & 900\ GeV^2 \\
60\ GeV & < & \nu & < & 500\ GeV \\
3\ GeV^2 & < & Q^2 & & \\
0.003 & < & x_B & & \\
0.1 & < & y_B & < & 0.85
\end{array}$$

where W^2 is the invariant mass of the hadronic system squared, ν is the energy loss of the lepton, Q^2 is the square of the momentum transferred by the virtual photon, and x_B and y_B are the Bjorken scaling variables. These variables were calculated from the energies of the incoming and the scattered muon together with the scattering angle.

The tracks used in the measurement were required to have $x_H > 0$, where $x_H = 2\,p_L^*/W$ is defined in the hadronic center-of-mass system.

The angle ϕ^* is defined as the azimuthal opening angle between the measured charged particle and the plane spanned by the two leptons in a system where the proton and the exchanged boson collide head-on. The definition is the same in the proton rest-system, the hadronic-center-of-mass system and the Breit-system, since these are connected through Lorenz transformations along the photon-proton axis.

The average $cos\phi^*$ of the detected charged particles was measured in the hadronic center-of-mass system as a function of a $p_\perp^*$-cutoff applied to the charged particles, where $p_\perp^*$ was measured relative the photon-proton axis. The results, shown in fig. 3.1, are taken from [Adams et al. 1993].

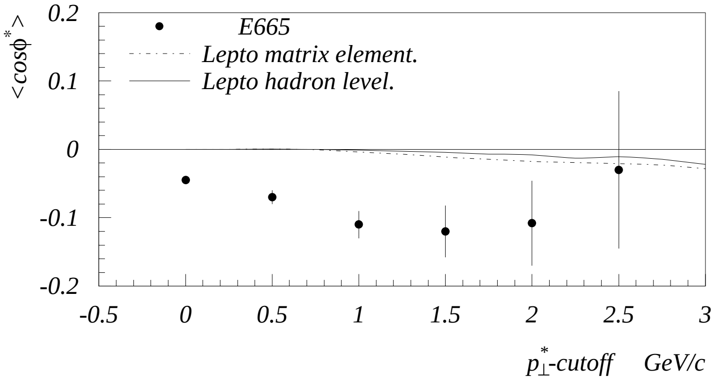

Figure 3.1: $\langle\cos\phi^*\rangle$ as measured by E665, compared to a MEPS model(Lepto 6.5) on matrix element level (dashed-dotted line) and hadron level (full line).

The Lepto Monte Carlo (see section 2.8 and appendix C) is used for comparisons. The default version used in fig. 3.1 contains zeroth and leading order processes in α_s. The intrinsic $p_\perp$ was set to zero for the default version since the intrinsic motion is implemented using an azimuthally flat random distribution and thus only has the effect of smearing the detected signal. This Monte Carlo cannot reproduce the signal measured by E665.

E665 explained the signal they measured with non-perturbative effects which has been discussed in a number of papers by introducing an intrinsic $p_\perp$ [Cahn 1978],[König & Kroll 1982],[Cahn 1989],[Chay, Ellis

& Stirling 1991],[Chay, Ellis & Stirling 1992] and [Seymour 1995]: In the collinear approximation, the partons are assumed to be parallel to the proton. If one, however, takes the proton-size into consideration two extra degrees of freedom appears. We will here choose these two to be the transverse momentum, $p^*_{\perp in}$, of the incoming parton and its azimuthal angle relative the lepton plane, ϕ^*_{in}. A proton-size of $\approx 1\,fm$ allows for a Fermi motion of the partons corresponding to a momentum of about $200\,MeV$. We will in this chapter see that if we introduce an intrinsic $p_\perp$ of that order as input, that the detected ϕ^* distribution is non-uniform, resulting in a measurable negative $\langle\cos\phi^*\rangle$. This has been pointed out in the articles above and has been used as the explanation for the effect seen in fig. 3.1. E665 used the model from Chay et al. to estimate a value of $0.5\,GeV$ for the intrinsic $p_\perp$ to describe their data.

We will in the following sections introduce an intrinsic $p_\perp$, following these ideas, into Lepto to study if we can improve the description seen in fig. 3.1.

In the last section we will address a different problem: The momentum transfer squared of the exchanged virtual boson can be calculated from the energies of the incoming and scattered leptons, and the scattering angle. However, since the energy of the incoming lepton is not measured but assumed to be equivalent to the nominal beam energy, initial state radiation which escapes undetected, would introduce an error in the calculation. This kind of radiation will cause any Lorenz transformation to be systematically wrong and thereby give rise to a systematic effect which will produce a negative $\langle\cos\phi^*\rangle$ signal. The effect turns out to be large and special care has to be taken not to introduce errors in the analysis.

3.3 Some comments on the implementation of the intrinsic $p_\perp$.

To ensure a continuous transition from zeroth to leading order processes we will here calculate the corrections for the intrinsic $p_\perp$ in both orders. For the zeroth order we will use the matrix-element in eq. 2.23 and for the two leading order processes the matrix-elements are: BGF in eq. 2.31 and QCD-Compton in eq. 2.34. The implementation will be done through a modification of an existing Monte Carlo program, Lepto 6.5 [Ingelman et al. 1997], and will be done to secure a minimum of change to the authors version. We will only calculate and change the azimuthal distribution and reorient already generated events. Technically the intrinsic-$p_\perp$ also changes the scattering amplitude but precautions will be taken to minimize this effect so that we can neglect it.

3.4 Intrinsic $p_\perp$ in zeroth order α_s processes.

Including the possibility for a $p^*_{\perp in}$ in the zeroth order matrix-element (eq. 2.23) simply means that we replace the incoming quark eq. A.5, which until now has been collinear with the proton, with one having a transverse momentum.

$$\tilde{v}^*_i = \frac{\sqrt{Q^2}}{2}(1,0,0,1) \to (\tilde{v}^*_{i0}, p^*_{\perp in}\cos\phi^*_{in}, p^*_{\perp in}\sin\phi^*_{in}, \tilde{v}^*_{iz}) \tag{3.1}$$

where ϕ^*_{in} is defined as the azimuthal angle of the plane spanned by the incoming quark and the photon with respect to the lepton plane. The scattered quark has the same transverse momentum and the same ϕ^* angle as the incoming quark. $\tilde{v}^*_{iz}$ is kept at $\sqrt{Q^2}/2$. Both partons are set to be mass-less.

To calculate the matrix-element we start by inserting this modified four-vector into the terms in the nominator of eq. 2.23.

$$\begin{aligned}
(\tilde{v}_{in}\cdot e)^2 &= (\tilde{v}^*_{i0}e^*_0 - \tilde{v}^*_{iz}e^*_z)^2 + \frac{1}{2}p^{*2}_{\perp in}e^{*2}_\perp \\
&\quad -2(\tilde{v}^*_{i0}e^*_0 - \tilde{v}^*_{iz}e^*_z)p^*_{\perp in}e^*_\perp\cos\phi^*_{in} + \frac{1}{2}p^{*2}_{\perp in}e^{*2}_\perp\cos 2\phi^*_{in} \quad (3.2)\\
(\tilde{v}_{in}\cdot e')^2 &= (\tilde{v}^*_{i0}e'^*_0 - \tilde{v}^*_{iz}e'^*_z)^2 + \frac{1}{2}p^{*2}_{\perp in}e'^{*2}_\perp \\
&\quad -2(\tilde{v}^*_{i0}e'^*_0 - \tilde{v}^*_{iz}e'^*_z)p^*_{\perp in}e'^*_\perp\cos\phi^*_{in} + \frac{1}{2}p^{*2}_{\perp in}e'^{*2}_\perp\cos 2\phi^*_{in} \\
&= (\tilde{v}^*_{i0}e^*_0 + \tilde{v}^*_{iz}e^*_z)^2 + \frac{1}{2}p^{*2}_{\perp in}e^{*2}_\perp \\
&\quad -2(\tilde{v}^*_{i0}e^*_0 + \tilde{v}^*_{iz}e^*_z)p^*_{\perp in}e^*_\perp\cos\phi^*_{in} + \frac{1}{2}p^{*2}_{\perp in}e^{*2}_\perp\cos 2\phi^*_{in} \quad (3.3)
\end{aligned}$$

Evaluating the matrix-element using these terms renders:

$$|\mathcal{M}_2|^2 \propto \tilde{a}_0 + \tilde{a}_1\cos\phi^*_{in} + \tilde{a}_2\cos 2\,\phi^*_{in} \tag{3.4}$$

where

$$\begin{aligned}
\tilde{a}_0 &= 2(\tilde{v}^{*2}_{i0}e^{*2}_0 + \tilde{v}^{*2}_{iz}e^{*2}_z) + p^{*2}_{\perp in}e^{*2}_\perp & (3.5)\\
\tilde{a}_1 &= -4\tilde{v}^*_{i0}e^*_0 p^*_{\perp in}e^*_\perp & (3.6)\\
\tilde{a}_2 &= p^{*2}_{\perp in}e'^{*2}_\perp & (3.7)
\end{aligned}$$

The denominator and the factors in front of the matrix-element are left untouched. Upon implementing this we can just add the $p^*_{\perp in}$ to the outgoing quark and reorienting it azimuthally.

The behavior we saw already in the tensor-contraction in section 2.2 can also be found here: $a_1 \propto p^*_{\perp in}$ and $a_2 \propto p^{*2}_{\perp in}$.

3.5 Intrinsic $p_\perp$ in leading order processes.

As mentioned above events are generated without intrinsic $p_\perp$ by the Lepto generator and the effect on the event by the intrinsic $p_\perp$ is imposed in a second step. The modified scattering process in principle has a different scattering amplitude and thus a different cross section than the originally generated event. The difference is, however, small except under specific kinematic conditions. The problems arise when the emitted radiation is very soft or collinear with the emitting parton which leads the denominator in eq. 2.28 to go to zero. Cutoffs have been introduced in the generator to avoid these divergences. The denominator of the matrix element can, for QCD-Compton (i.e. gluon brems-strahlung), be written as $(1-x_p)\,(1-z_q)$, and for BGF (i.e. photon-gluon-fusion) as $z_q\,(1-z_q)$ where

$$x_p = \frac{Q^2}{2\,\tilde{v}_{in}\cdot q} \qquad \text{and} \qquad z_q = \frac{\tilde{v}_{in}\cdot\tilde{v}_2}{\tilde{v}_{in}\cdot q}. \tag{3.8}$$

where q is the four-vector of the virtual photon. These two variables are used in the Lepto program to regulate the divergences of the matrix-elements so as to ensure that the leading-order cross-section is smaller than the total cross-section. Since these variables are intrinsically important to the program we cannot allow them to change in spite of the fact that we by implementing the intrinsic $p_\perp$ have changed the event. This constraint will fortunately lead to very small changes in the scattering amplitude.

A $2 \to 3$ process has 5 degrees of freedom, and by introducing the intrinsic-$p_\perp$ we add two more: the transverse momentum and the azimuthal angle of the incoming parton.

By introducing the intrinsic-$p_\perp$ the two outgoing partons have no longer the transverse momenta balanced in a reference system where the photon and proton collide head-on. The strategy is to calculate the transverse momentum, $\tilde{p}^*_{\perp 2}$, of the outgoing quark which has been related to z_q in eq. 3.8, under the constraint that the value of z_q is not changed by the influence of the transverse momentum. The tilde here indicates that the intrinsic $p_\perp$ has been included. The $p_\perp$ of the other parton, the other quark for BGF and the gluon for the QCD-Compton case, is given by momentum conservation.

The four-vectors of the partons can be expressed as:

$$\begin{aligned} \tilde{v}^*_{in} &= (\tilde{v}^*_{in0}, p^*_{\perp in}\cos\phi^*_{in}, p^*_{\perp in}\sin\phi^*_{in}, \tilde{v}^*_{inz}) && (3.9) \\ \tilde{v}^*_1 &= (\tilde{v}^*_{in0}, p^*_{\perp in}\cos\phi^*_{in} - \tilde{p}^*_{\perp 2}\cos\phi^*_2, \\ &\qquad p^*_{\perp in}\sin\phi^*_{in} - \tilde{p}^*_{\perp 2}\sin\phi^*_2, \tilde{v}^*_{inz}) && (3.10) \\ \tilde{v}^*_2 &= (\tilde{v}^*_{20}, \tilde{p}^*_{\perp 2}\cos\phi^*_2, \tilde{p}^*_{\perp 2}\sin\phi^*_2, \tilde{v}^*_{2z})\,. && (3.11) \end{aligned}$$

Inserting these into the expression of x_p shows that we can determine the longitudinal momentum $\tilde{v}_{inz}$,

$$\frac{Q^2}{2\,x_p} = \tilde{v}_{in}\cdot q = \tilde{v}^*_{inz}\sqrt{Q^2}. \tag{3.12}$$

The expression for z_q renders:

$$\begin{aligned} & z_q\,(\tilde{v}_{in}\cdot q) = \tilde{v}_{in}\cdot\tilde{v}_2 = \\ & = \tilde{v}^*_{in0}\sqrt{\tilde{p}^{*2}_{\perp 2} + \tilde{v}^{*2}_{2z}} - \tilde{p}^*_{\perp 2}p^*_{\perp in}(\cos\phi^*_2\cos\phi^*_{in} + \sin\phi^*_2\sin\phi^*_{in}) - \tilde{v}^*_{iz}\tilde{v}^*_{2z} = \\ & = \tilde{v}^*_{in0}\sqrt{\tilde{p}^{*2}_{\perp 2} + \tilde{v}^{*2}_{2z}} - \tilde{p}^*_{\perp 2}p^*_{\perp in}\cos(\phi^*_2 - \phi^*_{in}) - \tilde{v}^*_{iz}\tilde{v}^*_{2z} \end{aligned}$$

This equation can now be solved for $\tilde{p}^*_{\perp 2}$,

$$\begin{aligned} \tilde{p}^*_{\perp 2} = {} & \frac{A p^*_{\perp in}\cos(\phi^*_2 - \phi^*_{in})}{\tilde{v}^{*2}_{in0} - p^{*2}_{\perp in}\cos^2(\phi^*_2 - \phi^*_{in})} + \\ & \frac{\sqrt{\tilde{v}^{*2}_{in0}(A^2 - \tilde{v}^{*2}_{in0}\tilde{v}^{*2}_{2z}) + \tilde{v}^{*2}_{in0}\tilde{v}^{*2}_{2z}p^{*2}_{\perp in}\cos^2(\phi^*_2 - \phi^*_{in})}}{\tilde{v}^{*2}_{in0} - p^{*2}_{\perp in}\cos^2(\phi^*_2 - \phi^*_{in})} \end{aligned} \tag{3.13}$$

where

$$A = z_q\,(\tilde{v}_{in}\cdot q) + \tilde{v}_{inz}\tilde{v}_{2z}. \tag{3.14}$$

Since the final expression for the scattering amplitude will be proportional to $\tilde{p}^*_{\perp 2}\cos\phi^*$, eq. 2.10, it will be proportional to the square-root above. If we continue to use the angles ϕ^* and ϕ^*_{in} we would have to generate a two-dimensional distribution. The easiest way to get around this problem is to use the opening angle between the incoming and outgoing parton $\Delta\phi_2^* = \phi_2^* - \phi_{in}^*$ instead of ϕ_{in}^* as our seventh parameter. This will reduce the square-root to a one dimensional function and, as will be shown, put all of the dependence on ϕ^* in linear terms.

This gives:

$$\tilde{p}_{\perp 2}^* = \frac{A p_{\perp in}^* \cos\Delta\phi_2^* + \sqrt{\tilde{v}_{in0}^{*2}(A^2 - \tilde{v}_{in0}^{*2}\tilde{v}_{2z}^{*2}) + \tilde{v}_{in0}^{*2}\tilde{v}_{2z}^{*2}p_{\perp in}^{*2}\cos^2\Delta\phi_2^*}}{\tilde{v}_{in0}^{*2} - p_{\perp in}^{*2}\cos^2\Delta\phi_2^*}. \tag{3.15}$$

Upon setting $p_{\perp in}^* = 0\,GeV$ the only remaining terms are the first under the square-root, and the first in the denominator.

$$\tilde{p}_{\perp 2}^* = \frac{\sqrt{\tilde{v}_{in0}^{*2}(A^2 - \tilde{v}_{in0}^{*2}\tilde{v}_{2z}^{*2})}}{\tilde{v}_{in0}^{*2}} \tag{3.16}$$

Inserting the expressions for the four-vectors from appendix A, leads to $\tilde{p}_{\perp 2}^* = \sqrt{\hat{s}\, z_q(1-z_q)} \equiv p_{\perp 2}^*$ as expected. Since only real values of $\tilde{p}_{\perp 2}^*$ are of interest we will have $\sqrt{\tilde{v}_{in0}^{*2}(A^2 - \tilde{v}_{in0}^{*2}\tilde{v}_{2z}^{*2}) + \tilde{v}_{in0}^{*2}\tilde{v}_{2z}^{*2}p_{\perp in}^{*2}\cos^2\Delta\phi_2^*} > 0$ i.e. $\tilde{v}_{in0}^{*2}(\tilde{v}_{in0}^{*2}\tilde{v}_{2z}^{*2} - A^2) < \tilde{v}_{in0}^{*2}\tilde{v}_{2z}^{*2}p_{\perp in}^{*2}\cos^2\Delta\phi_2^*$. This fixes the limits for $\Delta\phi_2^*$ for given kinematics and $p_{\perp in}^*$.

Following the procedure of the previous chapter we insert the modified momenta into the terms in the nominator and expand the squares. The denominator has not changed. The matrix element for QCD-Compton scattering can then be expressed as:

$$\begin{aligned} |\mathcal{M}_3|_C^2 \quad \propto \quad & \tilde{c}_0 + \tilde{c}_1\cos\phi_2^* + \tilde{c}_2\cos 2\phi_2^* + \tilde{c}_3\cos(\phi_2^* + \Delta\phi_2^*) + \\ & \tilde{c}_4\cos 2(\phi_2^* + \Delta\phi_2^*) \end{aligned} \tag{3.17}$$

where

$$\tilde{c}_0 = 2\,(e_o^{*2}(\tilde{v}_{i0}^{*2} + \tilde{v}_{20}^{*2}) + e_z^{*2}(\tilde{v}_{iz}^{*2} + \tilde{v}_{2z}^{*2})) + e_\perp^{*2}(\tilde{p}_{\perp 2}^{*2} + p_{\perp i}^{*2}) \tag{3.18}$$

$$\tilde{c}_1 = -4\,\tilde{v}_{20}^* e_0^* e_\perp^* \tilde{p}_{\perp 2}^* \tag{3.19}$$

$$\tilde{c}_2 = e_\perp^{*2}\tilde{p}_{\perp 2}^{*2} \tag{3.20}$$

$$\tilde{c}_3 = -4\,\tilde{v}_{i0}^* e_0^* e_\perp^* p_{\perp in}^* \tag{3.21}$$

$$\tilde{c}_4 = e_\perp^{*2} p_{\perp i}^{*2}. \tag{3.22}$$

Setting $p_{\perp in}^*$ to zero again restores the original dependence on $p_{\perp 2}^*$. Integrating the matrix-element, eq. 3.17, over ϕ_2^* reduces the expression to contain only the term $\tilde{c}_0$ which depends on Q^2, y_B, x_p, z_q , $p_{\perp in}^*$ and $\Delta\phi_2^*$. After the values of Q^2, y_B, x_p and z_q have been fixed through the generation in Lepto, and $p^*_{\perp in}$ has been generated according to a Gaussian, $\tilde{c}_0$ will simply describe the distribution of $\Delta\phi^*_2$, and can be used as a probability function to generate $\Delta\phi^*_2$. Thereafter ϕ^*_2 can be generated from the complete expression of the matrix element eq. 3.17.

For BGF we have to insert the expressions for the two modified outgoing partons, eqs. 3.10-3.11, into the matrix-element. This will lead to a final form of the matrix-element which is slightly more complicated compared to the Compton case.

Again inserting these into the terms in the nominator and expanding the squares renders:

$$\begin{aligned} |\mathcal{M}_3|^2_B \propto\ & \tilde{b}_0 + \tilde{b}_1 \cos\phi^*_2 + \tilde{b}_2 \cos(\phi^*_2 + \Delta\phi^*_2) + \tilde{b}_3 \cos 2\phi^*_2 + \\ & \tilde{b}_4 \cos 2(\phi^*_2 + \Delta\phi^*_2) + \tilde{b}_5 \cos\phi^*_2 \cos(\phi^*_2 + \Delta\phi^*_2) \end{aligned} \tag{3.23}$$

where

$$\tilde{b}_0 = 2\,(e^{*2}_o(\tilde{v}^{*2}_{10} + \tilde{v}^{*2}_{20}) + e^{*2}_z(\tilde{v}^{*2}_{1z} + \tilde{v}^{*2}_{2z})) + e^{*2}_\perp(2\,\tilde{p}^{*2}_{\perp 2} + p^{*2}_{\perp i}) \tag{3.24}$$

$$\tilde{b}_1 = -4\,(\tilde{v}^*_{20} - \tilde{v}^*_{10}) e^*_0 e^*_\perp \tilde{p}^*_{\perp 2} \tag{3.25}$$

$$\tilde{b}_2 = 2\,e^{*2}_\perp \tilde{p}^{*2}_{\perp 2} \tag{3.26}$$

$$\tilde{b}_3 = -4\,\tilde{v}^*_{10} e^*_0 e^*_\perp p^*_{\perp in} \tag{3.27}$$

$$\tilde{b}_4 = e^{*2}_\perp p^{*2}_{\perp i} \tag{3.28}$$

$$\tilde{b}_5 = -4\,e^{*2}_\perp \tilde{p}^*_{\perp 2} p^*_{\perp in}. \tag{3.29}$$

Although the complexity of the expression is larger, the strategy in the generation of the event kinematics is the same as in the case of QCD-Compton. Integrating over ϕ^*_2 renders $\tilde{b}_0$ which can be used for generating $\Delta\phi^*_2$.

In summary the strategy in the generation procedure is the following:

1. Let Lepto generate Q^2, y_B, x_p and z_q, and in case of a first order α_s process decide whether it is a BGF or QCD-Compton event.
2. Generate $p^*_{\perp in}$ from a Gaussian.
3. Calculate, depending on the process, $\tilde{a}_0$,$\tilde{a}_1$ and $\tilde{a}_2$ (eqs. 3.5-3.7) or $\tilde{c}_0$ (eq. 3.18) or $\tilde{b}_0$ (eq. 3.24)
4. Generate ϕ^*_{in} or $\Delta\phi^*_2$
5. If $O(\alpha_s)$ generate ϕ^*_2

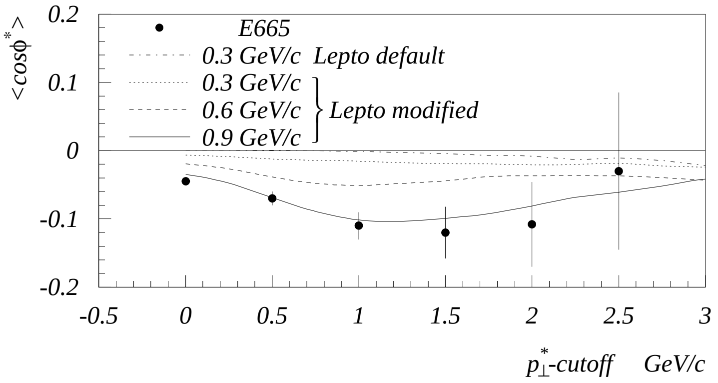

Figure 3.2: $\langle \cos\phi^* \rangle$ as measured by E665, compared to the default Lepto prediction (dashed-dotted line) and to a modified MEPS model, with different assumptions about $\langle p^*_{\perp in} \rangle$, on hadron-level.

3.6 Comparison of model predictions with data.

The model predictions were extracted for three different values of the intrinsic transverse momentum, $\langle p^*_{\perp in} \rangle = 0.3\,GeV$, $0.6\,GeV$ and $0.9\,GeV$. The resulting $\langle \cos\phi^* \rangle$ is plotted in fig. 3.2, from which it is found that an intrinsic $p_\perp$ of $0.9\,GeV$ gives a good description of the data. This $p^*_{\perp in}$ is, however, too large to be consistent with the Fermi motion of the partons inside the proton volume. An additional $p_\perp$ contribution may come from the higher order α_s processes.

The fact that E665 estimated a lower intrinsic $p_\perp$ using the model of Chay et al. is due to the fact that the fragmentation was described by special fragmentation functions, which amplified the asymmetry [Chay et al. 1992]. Based on comparisons with this model E665 estimated the intrinsic $p_\perp$ to 500 MeV and the "fragmentation $p_\perp$" to 700 MeV. We have used the standard Lund string-fragmentation, [Sjöstrand 1994], which does not consider the asymmetries. Therefore we have to use a larger value for the intrinsic $p_\perp$ to be comparable to the model of Chay et al..

In order to gain confidence in the method we have used to implement the intrinsic $p_\perp$, it is important to check that the total scattering amplitude does not change drastically. The result of our method is an increase in the amplitude but it turns out that this enhancement is limited to below 10%. Since this mainly is meant as a qualitative check rather than a quantitative estimate, this precision is perfectly acceptable.

3.7 QED-effects.

QED-radiation from the incoming and/or scattered lepton can also produce an effect in the measured distributions due to the fact that the event kinematics may be wrongly reconstructed as was explained earlier, see fig. 3.3. This gives rise to a systematic error in the Lorentz transformation which has to be performed to reach the hadronic-cms and the Breit-system. Consequently, this contribution is a purely experimental problem.

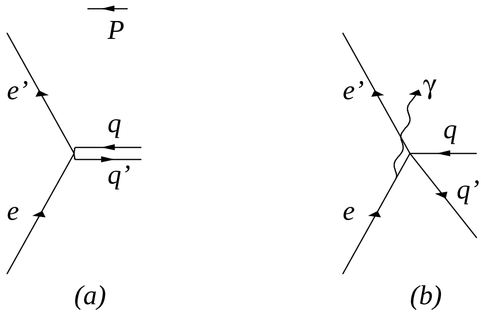

Figure 3.3: The effect of QED-radiation on the lepton-side as viewed in the Breit-system. In (a) a QPM-event is drawn. In (b) an initial-state photon has been radiated, and the Lorenz-transform from the lab has been calculated using the nominal beam-energy e, which is slightly larger than the true lepton energy. Due to momentum conservation the scattered quark q' *has* to absorb the $p_\perp^*$ of the photon γ. The final-state-radiation will work in the same direction.

The influence of QED can be estimated through a short calculation. For this we define a reference system where the incoming and scattered leptons are contained in the $x-z$-plane. In this system we have $\cos\tilde{\phi}^* = p_x/p_\perp$ where the tilde now denotes that the transverse momentum of the photon has been included. The expressions for the x-component of the transverse momentum and the total transverse momentum become:

$$\tilde{p}_x^* = p_\perp^* \cos\phi^* - p_{x\gamma}^* \tag{3.30}$$

$$\tilde{p}_\perp^{*2} = p_\perp^{*2} - 2p^*_{x\gamma}p^*_\perp \cos\phi^* + p^{*2}_{x\gamma}. \tag{3.31}$$

Using these to calculate the measured $\cos\tilde{\phi^*}^*$ renders

$$\cos\tilde{\phi}^* = \frac{\tilde{p}^*_x}{\tilde{p}^*_\perp} = \frac{p^*_\perp \cos\phi^* - p^*_{x\gamma}}{\sqrt{p_\perp^{*2} - 2p^*_{x\gamma}p^*_\perp \cos\phi^* + p^{*2}_{x\gamma}}} \tag{3.32}$$

For a qualitative estimate of the effect from QED we can neglect the influence from the denominator and get the average observed distribution to be:

$$\langle\cos\tilde{\phi}^*\rangle \approx \langle\cos\phi^*\rangle - \langle\frac{p^*_{x\gamma}}{p^*_\perp}\rangle. \tag{3.33}$$

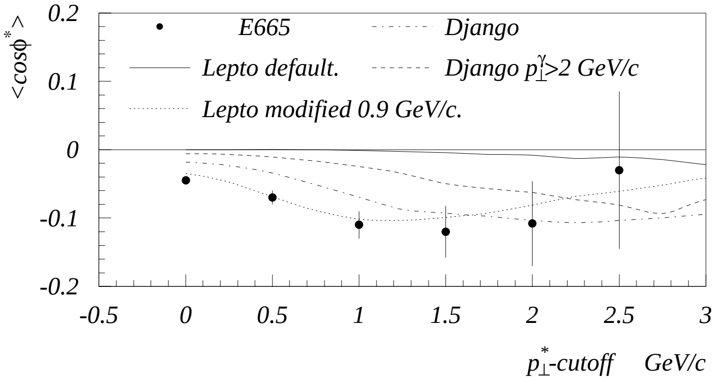

Figure 3.4: $\langle\cos\phi^*\rangle$ as measured by E665, compared to the default Lepto prediction (full line), to a modified MEPS model with $\langle p^*_{\perp in}\rangle = 0.9 GeV/c$ (dotted line), and to a LO-QED model (Django 6.2) where the dashed-dotted and the dashed lines correspond to different Lorentz transforms, described in the text, on hadron level.

The QCD contribution to $\langle\cos\tilde{\phi^*}\rangle$ is displaced by a linear term in $p^*_{x\gamma}$. This is a very short and approximate calculation to show that QED indeed produces a signal.

The Monte Carlo used by E665 to calculate the QED corrections was based on a leading-order QED calculation, without virtual corrections, and using a $p_\perp$ cutoff to stay away from the divergences.

We have used the Django Monte Carlo program to estimate the shape of the $\langle \cos \tilde{\phi}^* \rangle$ distribution including effects from QED. Django provides an interface between the HERACLES and LEPTO programs. In HERACLES complete first order α_{em} corrections are performed. i.e. virtual corrections and the emission of one initial or final state photon are included. The QCD effect is produced by Lepto.

The $p_\perp$ cutoff, used in the E665 Monte Carlo, was taken into account by introducing an artificial cutoff in Django applied in the following way: If the emitted photon has a $p_\perp$ smaller than the cutoff value, the boost was performed into the hadronic center-of-mass system by taking the photon momentum into account. If, however the photon had a $p_\perp$ greater than the cutoff value, the nominal energy of the incoming lepton was used, leading to an error in the transformation. The consequence of this is a non-zero $\langle \cos \phi^* \rangle$ which is due to the systematic error in the Lorentz boost due to initial photon radiation.

In fig. 3.4 the results from Django are plotted together with the results from the modified Lepto and the data-points from E665. The Django results can describe the general trend of the data points. The curve with a cutoff at 2 GeV shows the sensitivity of the signal to QED brems-strahlung. It is evident that one has to be very careful with the QED corrections to make a reliable measurement.

It is of course impossible to estimate the effect of the cutoff used by E665, and thus the effect of the QED-correction, without direct access to their Monte Carlo program, but this simple investigation indicates that the corrections due to QED radiation may be considerable.

4

Jets.

4.1 Introduction.

The signature of a typical DIS event is flows of hadrons stemming from the partons involved in the hard scattering process and hadrons coming from the proton remnant. Due to the colour field stretched between the scattered partons and the proton remnant there is no unambiguous way to assign the detected hadrons to either the remnant or the hard sub-system. However, in the Breit-system the remnant continues essentially in the direction of the incoming proton and the hadrons stemming from the hard sub-system appear as collimated flows of particles, or jets, proceeding along the original directions of the scattered partons, provided the energy involved in the process is large enough. In the present analysis the $k_\perp$-algorithm for jet finding has been used. The procedure to reconstruct jets in this algorithm will be described as well as its specific application in this analysis.

It will be shown that the limited detector acceptance will influence the ϕ^* resolution. In order to improve the situation an energy flow parameter has to be used. In addition the limited detector acceptance will by itself produce a signal in ϕ^* which requires some consideration. The Lepto Monte Carlo generator has been used in different versions to illustrate these effects. In the first version we have removed the QCD effects on the azimuthal distributions and the intrinsic $p_\perp^*$ which enabled us to study any fake signals. Secondly the authors default version with LO QCD predictions assuming no intrinsic transverse parton momentum was used. In addition the modified version, including an intrinsic $p_\perp^*$ of 0.9 GeV, developed in the previous chapter was used for comparison. Finally we compare the expected signal from a NLO QCD calculation (DISENT) to the leading order signal from Lepto.

4.2 The $k_\perp$-algorithm.

In [Catani, Dokshitzer & Webber 1992] and [Catani, Dokshitzer & Webber 1994] the $k_\perp$ jet-algorithm for eP-physics is developed. It is a clustering algorithm which compares the distances between all pairs of four-vectors, representing final-state hadrons, plus the distance from each individual four-vector to the proton direction. The distance measure, $k_\perp$, is defined as follows:

$$k^2_{\perp\, ij} = min\left(E_i^2, E_j^2\right)\, 2(1 - \cos\theta_{ij}) \qquad \forall\; i,j \in [1,n] \;\; i \neq j \qquad (4.1)$$

and

$$k^2_{\perp\, ip} = E_i^2\, 2(1 - \cos\theta_{ip}) \qquad \forall\; i \in [1,n]. \qquad (4.2)$$

where $\cos\theta_{ij}$ and $\cos\theta_{ip}$ are the angles between the four-vectors of the hadrons i and j and between the hadron i and the proton direction p, respectively. E_i and E_j are the corresponding energies.

If the smallest distance is of the type $k_{\perp\, ip}$, then hadron i is regarded as belonging to the proton remnant and is rejected. In case that the smallest distance is of the type $k_{\perp\, ij}$ the two four-vectors i and j are added covariantly. In this analysis the procedure is repeated until each event is reduced to contain exactly two jets for which a distance value $k^2_\perp$ is extracted. To enable a comparison between events this distance is scaled with Q^2 producing a dimensionless measure of the hardness of the event.

In chapter 2 we studied the azimuthal distribution on the parton-level where the definition of the ϕ^* angle is trivial. There the incoming parton, in the Breit frame, collide head on with the photon and therefore the two hard partons from the scattering have to balance in $p^*_{\perp 2}$. With the use of the $k_\perp$ algorithm we can investigate the azimuthal distribution on hadron level by reconstructing jets. The assumption is that these jets carry information about the underlying partons. In the reconstruction of the hadron plane we have used all hadrons assigned to the hard jets in order to calculate a two-dimensional thrust axis in the azimuthal plane. For this we reduce the normal thrust-calculation, [Sjöstrand 1994], from three to two dimensions by introducing a two-dimensional unit vector in Breit-system: $\bar{n} = (\cos\phi^*, \sin\phi^*)$. The two-dimensional thrust axis is then found by maximizing:

$$\tilde{T}^2(\phi^*) = \sum_i h^{*2}_{\perp i} \cos^2(\phi^*_{h_i} - \phi^*). \qquad (4.3)$$

This equation has two equal maxima in ϕ^* separated by 180°, and to resolve this ambiguity we choose the maximum closest to the backward jet for the definition of the ϕ^* angle.

4.3 Kinematic range.

In order to ensure that the scattered lepton falls inside the acceptance of the backward electro-magnetic calorimeter and that a good separation between the the leptonic and hadronic system is achieved, the following kinematic cuts were applied on the scattered positron:

$$\begin{array}{ccccc} 10\,GeV^2 & < & Q^2 & < & 100\,GeV^2 \\ 0.2 & < & y_B & < & 0.65 \\ 156^\circ & < & \theta_{scl} & < & 176^\circ \end{array}$$

4.4 Resolution.

The LAr detector has an acceptance which is limited to the angular range between 6° and 150° in the laboratory system which causes a problem in the reconstruction of the ϕ^*-angle. Depending on the kinematics one of the hadron jets may proceed in the backward region and escape detection in the LAr calorimeter. On the parton-level one could simply require two partons in order to determine whether the event is fully contained in the detector. On the hadron-level higher-order emissions, and the non-perturbative fragmentation will produce a flow of hadrons from each parton and the exact number of hadrons in the final state is a priori unknown. In order to determine how much of the event is contained in the detector we instead use the light-cone momenta, remembering that the proton defines the positive z direction. The incoming proton has $P_-^* = E^* - p_z^* \equiv 0$, and the incoming virtual boson has, from the definition of the Breit-system, $q_-^* \equiv \sqrt{Q^2}$. On the parton-level the remnant has $r_-^* \equiv 0$, which means that the two hard partons *have* to carry all of the negative light-cone momentum. As was mentioned previously this is not completely valid on the hadron-level due to the effects of higher order emissions and non-perturbative effects. On the other hand it is reasonable to assume that the hadron jets still have to carry a large fraction of the light-cone momentum. Thus by requiring the detected hadrons to carry more than a certain fraction of the light-cone momentum it is possible to reconstruct the hadron-plane.

Th energy fraction, i_-^*, is defined as the scaled negative light-cone momentum of the detected hadrons in the Breit-system:

$$i_-^* = \frac{h_-^*}{\sqrt{Q^2}} = \frac{\sum_i E_i^* - p_{z\,i}^*}{\sqrt{Q^2}}. \tag{4.4}$$

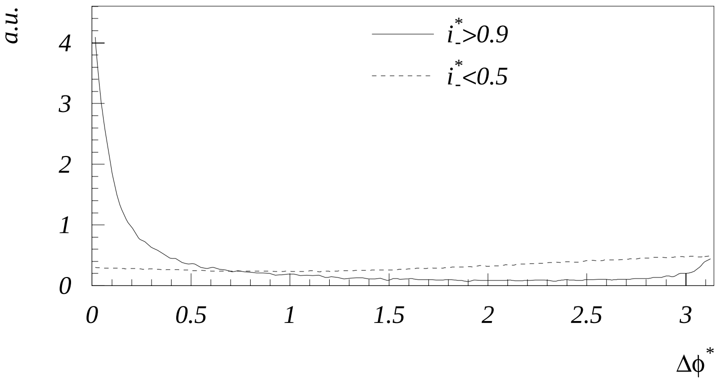

Figure 4.1: The resolution in ϕ^* using jets, for two different intervals in the energy-flow i_-^*. $\Delta\phi^*$is defined as the absolute difference between the ϕ^* angle reconstructed on the hadron-level and the one generated on the parton-level.

With the resolution variable $\Delta\phi^*$ defined as the difference between the ϕ^* angle reconstructed on the hadron-level and the one generated on the parton-level we can study the effect of applying a cut in the scaled light-cone momentum. This is illustrated in fig. 4.1 by giving the two examples $i_-^* < 0.5$ and $i_-^* > 0.9$. The results show that requiring less than 50% of the light-cone momentum in the detector gives a more or less flat $\Delta\phi^*$ distribution and thus no resolution at all is obtained. With more than 90% of the light-cone momentum detected, a sharp peak is observed at small values of $\Delta\phi^*$ indicating an excellent resolution. The price which has to be paid to obtain this good resolution is of course that a large fraction of the statistics is cut away.

In chapter 5 it will be shown that the detector-level resolution for i_-^* is not good enough to apply a cut. There are large migrations due to errors in the energy measurement and from initial-state QED radiation. We will therefore, in chapter 6, derive an unfolding algorithm to correct for detector effects over the full range $0 < i^{*}_{-} < 1$. This enables us to extract the signal for $i^{*}_{-} > 0.9$ as our final result.

4.5 The H1 acceptance.

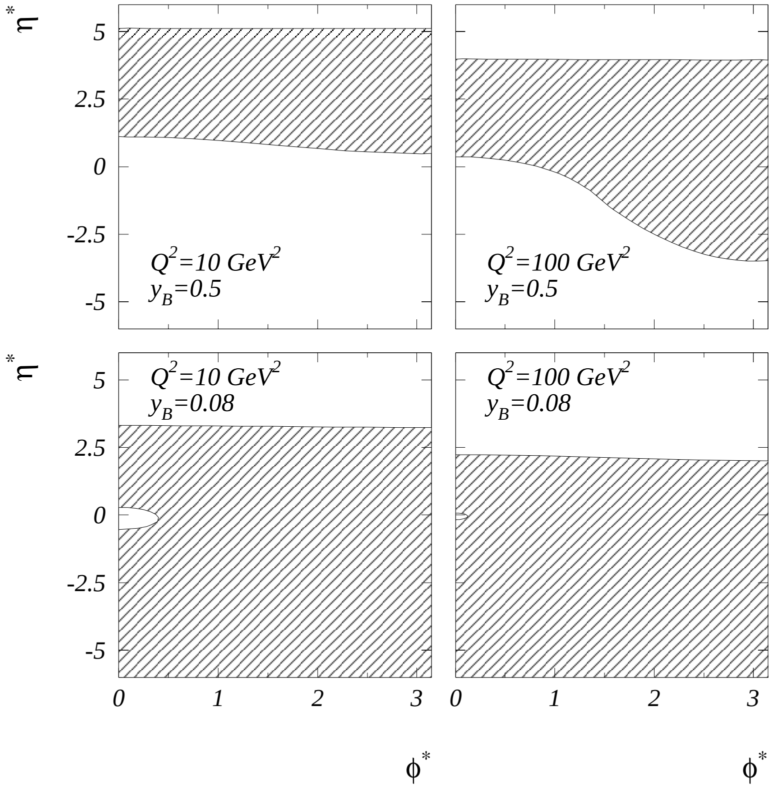

Figure 4.2: The shape of the LAr-calorimeter in the Breit-system for different kinematic values. The hatched area gives the acceptance of the LAr calorimeter.

The detector is a symmetric cylinder in the laboratory with acceptance holes in the forward and backward regions, which can be described by cones with certain opening angles centered around the beam axis and with its tips in the interaction point. Thus the azimuthal acceptance in the laboratory is flat. In the Breit frame the detector has a different shape for every event depending on the event kinematics. If the boost into the Breit frame is only a longitudinal one, it only affects the opening angles of the cones but the azimuthal acceptance remains flat. The effect of a transverse boost is to change the directions of the cones so that they are no longer aligned. This will cause a non-flat ϕ^* acceptance. The acceptance of the LAr calorimeter in the Breit frame is drawn in fig. 4.2 for four different kinematic situations. One immediate observation from the top row of fig. 4.2 is that there is a larger acceptance in rapidity for $\phi^* = \pi$ than for $\phi^* = 0$. This will result in an $\langle \cos\phi^* \rangle < 0$ [Jacobsson 1994] and consequently one has to find a way around this difficulty.

The accumulated effect of the limited acceptance on the ϕ^* asymmetry over the whole kinematic range can be seen in fig. 4.3 where $\langle \cos\phi^* \rangle$ is plotted as a function of the $k_\perp^2/Q^2 - cutoff$. The results are given for three different regions of light-cone momenta and for the two cases where the $k_\perp^2/Q^2$ is above and below the $k_\perp^2/Q^2 - cutoff$ value, respectively. All events which contributed to the plots were required to have at least two hadrons within the acceptance of the LAr calorimeter.

In principle it should be possible to correct for the acceptance effects but, as we will see, the faked signals from these effects are several times bigger than the real signals. Instead we have chosen to avoid the acceptance problem by defining, for each event, the rapidity region which has a flat acceptance in ϕ^*.

If we again study fig. 4.2 it illustrates four specific situations, which are (top left) small longitudinal and transverse boosts, (top right) large longitudinal and small transverse boost, (bottom left) small longitudinal and large transverse boost and finally (bottom right) large longitudinal and transverse boosts. The idea is to find the rapidity limits which define a region of flat ϕ^* acceptance. However, as seen in the bottom row of fig. 4.2 there are in some cases 'holes' in the acceptance area. The rapidity region defined by these 'holes' must also be excluded in order to obtain a completely flat acceptance in ϕ^*.

The limits of the rapidity range in the Breit frame can be calculated for each event from the event kinematics. The rapidity is given from scalar-products of a massless four-vector h with the proton four-vector P and the four-vector of the virtual boson q as:

$$y^* = \frac{1}{2}\log\frac{h_+^*}{h_-^*} = \frac{1}{2}\log\left(1 + \frac{q \cdot h}{x_B\, P \cdot h}\right). \tag{4.5}$$

For the azimuthal angle we need an explicit expression for h_x^* and the

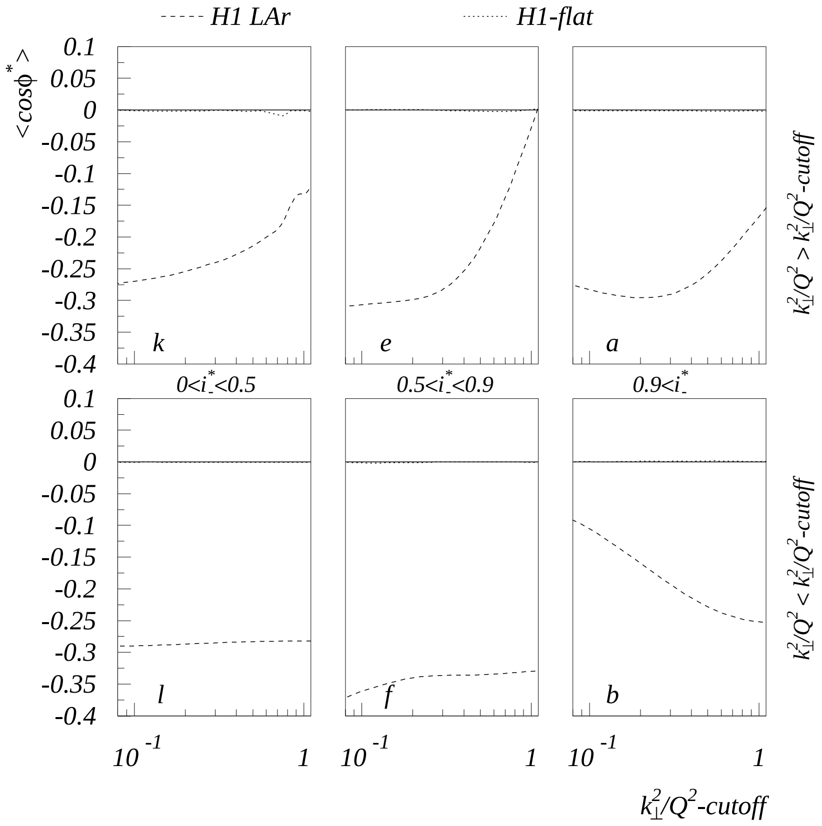

Figure 4.3: $\langle \cos\phi^* \rangle$ as function of the $k_\perp^2/Q^2 - cutoff$ in three different bins of the scaled light-cone momentum, i_-^*. The results are given for events above the $k_\perp^2/Q^2 - cutoff$, top row, and those below, bottom row. The two curves show the Lepto Monte Carlo prediction without any azimuthal asymmetry included. The dashed curve includes the full acceptance of the LAr calorimeter, and the dotted line corresponds to the azimuthally flat acceptance. The naming-scheme of the bins is adapted to the fact that there will be twice as many bins on detector level.

result is

$$\cos\phi^* = \frac{h_x^*}{h_\perp^*} = \frac{y_B}{\sqrt{1-y_B}\sin\theta_h^*}\left(\frac{2-y_B}{2\,y_B} + \frac{\cos\theta_h^*}{2} - \frac{e\cdot h}{(2x_BP+q)\cdot h}\right) \tag{4.6}$$

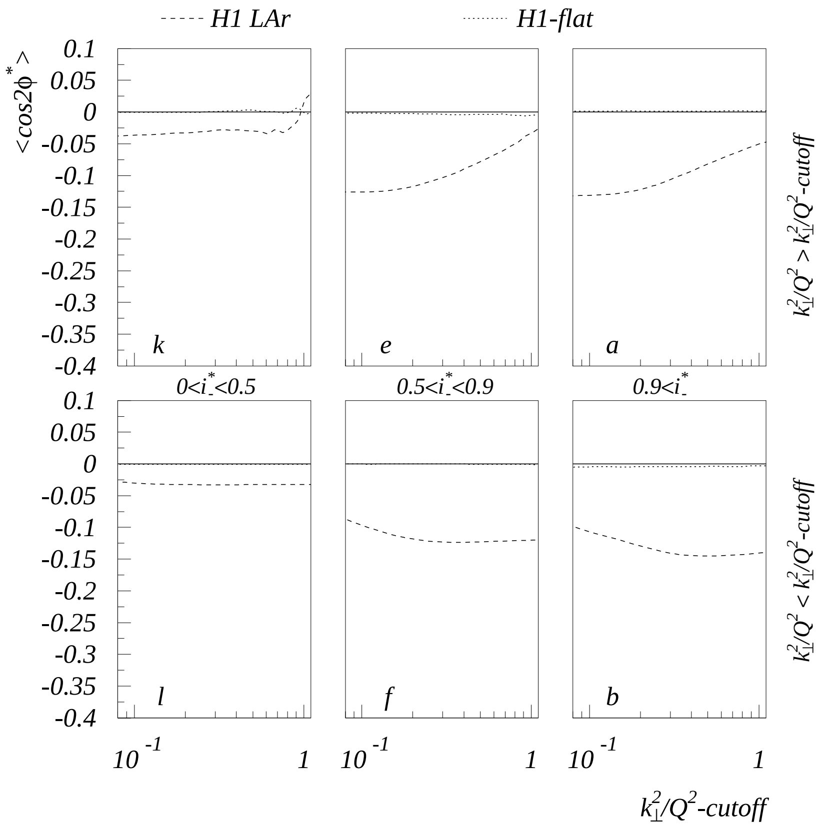

Figure 4.4: $\langle \cos 2\phi^* \rangle$ as function of the $k_\perp^2/Q^2 - cutoff$ in three different bins of the scaled light-cone momentum, i_-^*. The results are given for events above the $k_\perp^2/Q^2 - cutoff$, top row, and those below, bottom row. The two curves show the Lepto Monte Carlo prediction without any azimuthal asymmetry included. The dashed curve includes the full acceptance of the LAr calorimeter, and the dotted line corresponds to the azimuthally flat acceptance.

where θ_h^* is the polar angle of h in the Breit-system. Using these equations we can calculate the rapidity and ϕ^*-angle in the Breit system for an arbitrary four-vector in the laboratory frame. By placing a four-vector in the lepton plane of the laboratory system, at the boundaries of the LAr acceptance in rapidity for $\phi = 0$ and π, we can thus calculate the acceptance in the Breit frame. From this we can define a maximum region of flat acceptance ϕ^*. In the top right picture of fig. 4.2 this means that we calculate the two corners of the hatched area at $\phi^* = 0$, as well as the two at $\phi^* = \pi$. We can then cut out all four-vectors ending up in the curved area below $\eta^* \approx 0.5$ and create a flat acceptance.

To study the effects of the acceptance we removed the QCD corrections to the azimuthal angle in the Lepto Monte Carlo. The results in figs. 4.3-4.4 are given both for the full LAr acceptance and for flat acceptance. Whereas the former case produces a significant effect the latter gives results consistent with zero. This proves that an influence on the signal from detector effects can be avoided.

In the following *all* results will be using the flat acceptance.

4.6 The expected signal.

The LEPTO Monte Carlo generator has been used to estimate the signals in $\langle \cos \phi^* \rangle$ and $\langle \cos 2\phi^* \rangle$ as a function of $k_\perp^2/Q^2$ cutoff, after the acceptance effects have been removed. Presented are results for three different scenarios corresponding to no intrinsic transverse parton momentum (LEPTO default), an intrinsic $p_\perp^*$ of 0.9 GeV included (LEPTO modified) and the QCD signal removed from the Monte Carlo program (LEPTO uncorrelated). As before the results are subdivided into three regions in the flow parameter i_-^*, and for $k_\perp^2/Q^2$ larger and smaller than the cutoff value.

The first observation from figs. 4.5-4.6 is that the LEPTO version from which the generation of azimuthal asymmetries has been removed, does not produce any signal neither for $\langle \cos \phi^* \rangle$ nor for $\langle \cos 2\phi^* \rangle$ as is also expected provided there is no influence of the acceptance.

Fig. 4.5 shows that the magnitude of the $\langle \cos \phi^* \rangle$ signal is below 2% in all bins except for $0.5 < i_-^* < 0.9$ and $i_-^* > 0.9$ as $k_\perp^2/Q^2 > k_\perp^2/Q^2 - cutoff$ is required. The effect of the intrinsic $p_\perp^*$ is considerable in the bins $0.5 < i_-^* < 0.9$ and $i_-^* > 0.9$ for $k_\perp^2/Q^2 < k_\perp^2/Q^2 - cutoff$. The only bin which exhibit a reasonable signal is $i_-^* > 0.9$ demanding $k_\perp^2/Q^2 > k_\perp^2/Q^2 - cutoff$.

The $\langle \cos 2\phi^* \rangle$ signal seems to be less sensitive to the intrinsic $p_\perp^*$ as seen from fig. 4.6. In the lowest i_-^* bin the signal is very small both for $k_\perp^2/Q^2 < k_\perp^2/Q^2 - cutoff$ and for $k_\perp^2/Q^2 > k_\perp^2/Q^2 - cutoff$.

The distributions of $\langle \cos \phi^* \rangle$ and $\langle \cos 2\phi^* \rangle$ for the bin with $i_-^* > 0.9$ and a $k_\perp^2/Q^2$ above the $k_\perp^2/Q^2 - cutoff$ are presented in more detail

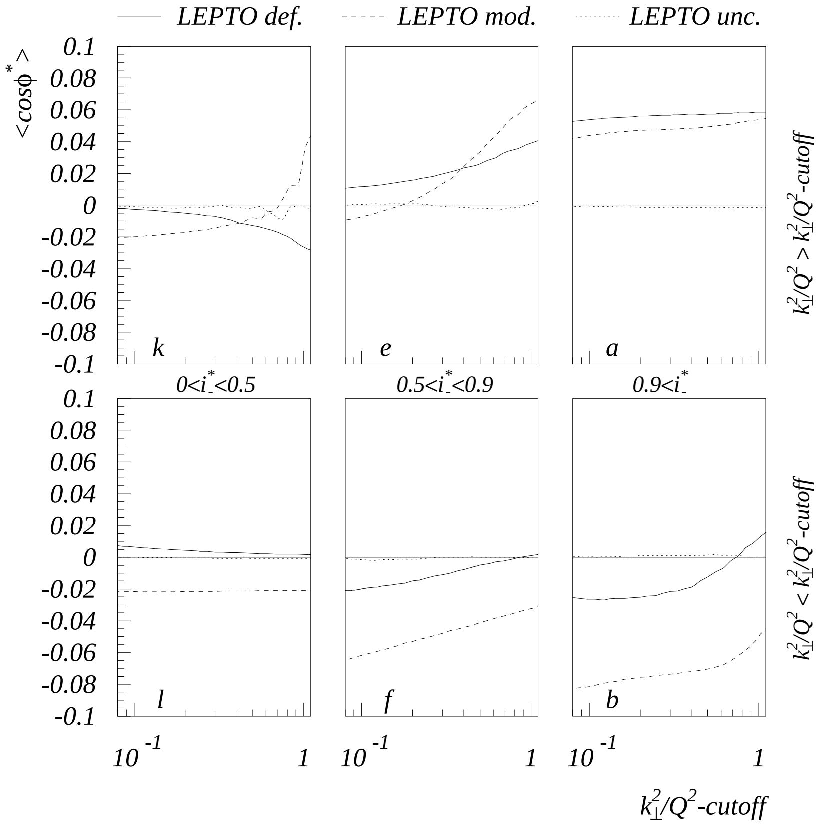

Figure 4.5: The $\langle \cos\phi^* \rangle$ signal as expected if the azimuthal asymmetry is removed (dotted line), from normal QCD including the asymmetry (full line) and with an intrinsic-$p_\perp$ (dashed line), using the analysis method described. $\langle \cos\phi^* \rangle$ is shown as a function of the $k_\perp^2/Q^2 - cutoff$ for $k_\perp^2/Q^2 < k_\perp^2/Q^2 - cutoff$ and $k_\perp^2/Q^2 > k_\perp^2/Q^2 - cutoff$. The binning and naming-scheme are described in fig. 4.3.

in fig. 4.7. Here the signals have been extracted separately for QCD-Compton events (quark induced) and BGF-processes (gluon induced). LEPTO has been used in its default version i.e. without any intrinsic $p_\perp^*$, and for comparison also the results from the DISENT program are shown. DISENT calculates cross sections for DIS-processes up to next-

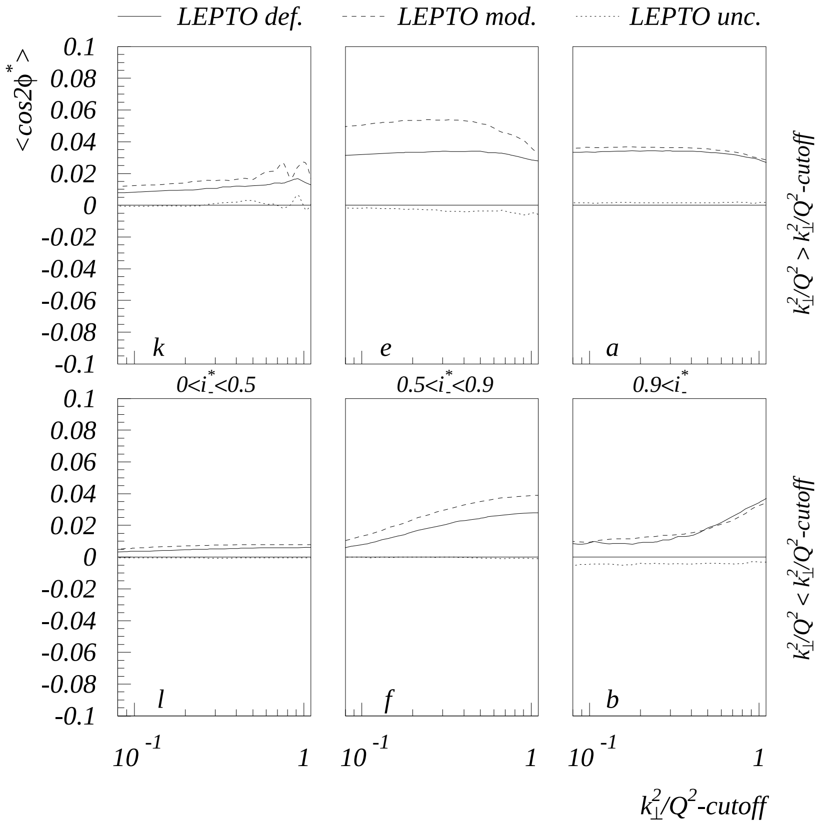

Figure 4.6: The $\langle \cos 2\phi^* \rangle$ signal as expected if the azimuthal asymmetry is removed (dotted line), from normal QCD including the asymmetry (full line) and with an intrinsic-$p_\perp$ (dashed line), using the analysis method described. $\langle \cos 2\phi^* \rangle$ is shown as a function of the $k_\perp^2/Q^2 - cutoff$ for $k_\perp^2/Q^2 < k_\perp^2/Q^2 - cutoff$ and $k_\perp^2/Q^2 > k_\perp^2/Q^2 - cutoff$. The binning and naming-scheme are described in fig. 4.3.

to-leading order. We notice that the dominant contribution to the signal comes from the gluon induced process both for $\langle \cos \phi^* \rangle$ and for $\langle \cos 2\phi^* \rangle$. The NLO corrections are largest for the $\langle \cos \phi^* \rangle$ from the gluon induced processes. It will turn out that we cannot resolve this difference when we look at the data.

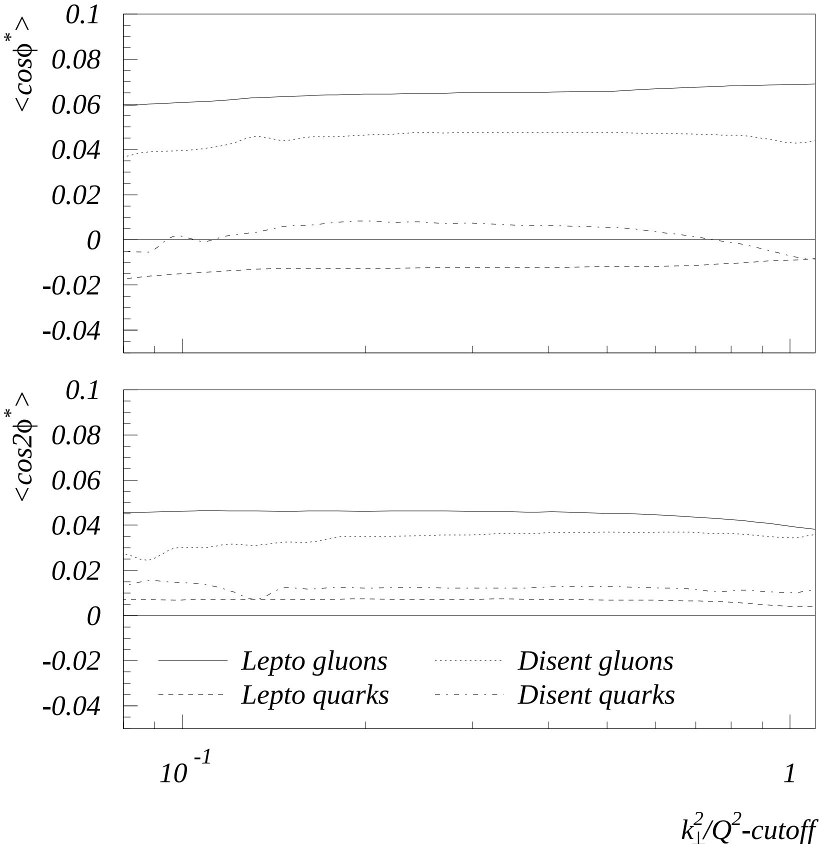

Figure 4.7: The high energy flow bin ($i^*_- > 0.9$) for $k_\perp^2/Q^2 > k_\perp^2/Q^2 - cutoff$. $\langle \cos\phi^* \rangle$ (top) and $\langle \cos 2\phi^* \rangle$ (bottom) are shown as a function the $k_\perp^2/Q^2 - cutoff$. The curves correspond to the Lepto predictions for gluon initiated (full lines) and quark initiated (dashed lines) processes, and to NLO predictions (Disent) for gluon initiated (dotted lines) and quark initiated (dash-dotted lines) processes.

4.7 Conclusions.

We have established that a jet-algorithm can be used in order to reconstruct the hadronic plane by clustering the four-vectors of the measured hadrons until two jets remain in every event. At the point in the clustering procedure where exactly two jets are obtained a distance-measure $k_\perp^2/Q^2$ is extracted as an estimate of the hardness of the event. The four-vectors of the two jets are used to reconstruct the hadron-plane.

Two major problems connected to the measurement have been solved. Firstly the relevant variables have been identified by which a region of good ϕ^* resolution can be defined. Secondly the effect of the limited detector acceptance has been removed by calculating, on an event by event basis, the largest rapidity range with an azimuthally flat acceptance in the Breit-system.

Due to the fact that the acceptance effects produce asymmetries which are four times larger than the expected QCD signals, all investigations on the hadron and the detector level, have been performed in the regions of azimuthally flat acceptance only and no extrapolations have been done.

5

Hera and H1.

5.1 DESY.

The German research laboratory DESY (Deutsches Elektronen Synchrotron) was founded in 1959. As the name indicates it was centered around a 7 GeV electron synchrotron. A number of experiments were performed at this accelerator over the years until the DORIS electron-positron collider was taken into operation in 1974. This collider was covering the energy range up to just beyond 10 GeV. In 1979 the PETRA electron-positron ring was completed offering collision energies up to 38 GeV. At this machine the first observation of three jet events were made and thus the experimental evidence for the existence of the gluon was given. The construction of the "Hadron-Electron Ring Accelerator" (HERA) started in 1984 and in 1991 HERA was put into operation. It is the first and only electron-proton collider in the world and its center-of-mass energy of about 300 GeV is by more than a factor ten larger than those reached in previous DIS experiments with fixed proton targets. In this chapter we will give a brief overview of the HERA collider and the layout of the H1 detector. Those detector components which have been specifically used in this analysis are described in more detail. We furthermore go through the methods used to reconstruct the event kinematics and show the resulting resolution in the various kinematic variables.

5.2 HERA.

The HERA collider consists of two separate storage rings, placed in a subterranean circular ring tunnel of 6.3 km circumference. Positrons* (or electrons) and protons are separately accelerated up to energies of 27.5

---

*The present analysis is based on the data taken 1997 where HERA was operated with positron beams due to problems with the lifetime of the electron beam.

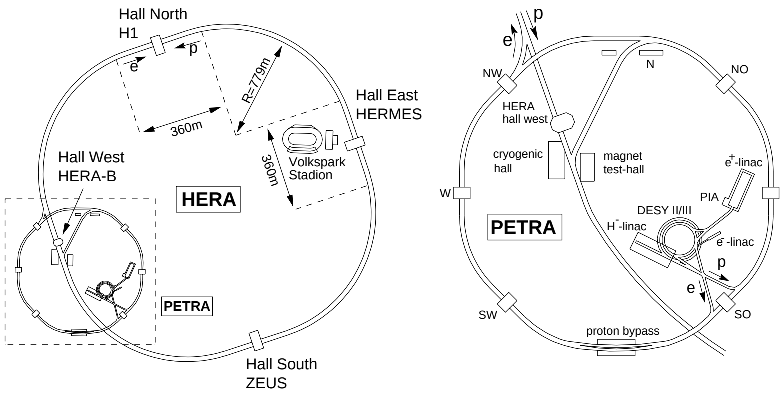

Figure 5.1: The electron-proton collider HERA (left), and the area of the DESY (right) including the pre-accelerators LINAC I–III, DESY I–III and PETRA.

GeV and 820 GeV[†], respectively, and brought to collision at the North Hall and the South Hall, where the multi-purpose detectors of the H1 and the ZEUS collaborations are located (fig. 5.1a). These experiments have been taking data since 1992. The fixed target experiments HERMES and HERA-B are located in the West Hall and in the East Hall, respectively. Since 1995 the HERMES experiment measures collisions of the polarized lepton beam with polarized protons from a gas target to study phenomena related to the spin of the target particles. The HERA-B experiment utilizes tungsten wire targets inserted into the proton beam halo to produce proton-proton collisions. The main goal is to search for decay modes of the $B^0 - \bar{B}^0$ system, which indicate a violation of the combined charge conjugation and parity (CP) conservation.

Fig. (fig. 5.1b) gives an overview of the various preaccelerators, which are needed to prepare the beams for HERA. The proton beam is produced by passing H^- ions, accelerated to an energy of 50 MeV in LINAC III, through a stripper foil in order to remove the electrons. They are then collected in bunches and accelerated in DESY III to 7.5 GeV and in PETRA to 40 GeV before they are injected into HERA for acceleration to the final energy. Leptons are provided by a 500 MeV linear accelerator, and after acceleration in DESY II to 7 GeV and in PETRA to 12 GeV before they are injected into HERA to reach 27.5 GeV. The

---

[†] In 1998 the energy of the proton beam was increased to 920 GeV and the positron beam was again replaced by an electron beam.

leptons (protons) are stored in typically 190 colliding bunches, with a length of 8 mm (110 mm) and typical currents of 30 mA (80 mA). The bunch crossing interval is 96 ns, corresponding to a bunch crossing rate of 10.4 MHz. The lifetime of the lepton (proton) beam is typically 10 (100) hours.

5.3 H1.

The H1 laboratory frame is defined by a right-handed coordinate system where the positive z-axis points along the proton beam direction. The x-axis points to the center of the HERA ring and the y-axis upwards. The nominal interaction point is taken as the origin. The polar angle θ is defined with respect to the positive z-direction and azimuthal angles are defined such that $\phi = 0$ points to the positive x-direction.

The final state particles from the lepton-proton collisions are detected by the HERA detectors H1 and ZEUS. Both are designed as nearly hermetic multi-purpose detectors. A side view of the H1 detector is shown in fig. 5.3. To account for the asymmetric beam energies of the colliding particles the forward region (i.e. the region along the proton direction) is equipped with enhanced instrumentation. A detailed description of the H1 detector can be found in [Abt et al. 1997]. In this measurement the liquid argon (LAr) calorimeter, the backward calorimeter, the tracking chamber system and the luminosity detectors are of particular importance.

5.4 Trackers.

The H1 tracking system includes three major components which cover polar angles in the range of $5^\circ < \theta < 178^\circ$ with full azimuthal coverage (fig. 5.3). The central tracking chambers and the forward tracking detector are placed around the beam pipe between z = -1.5 m and z = 2 m. The backward drift chamber (BDC) is located in front of the backward calorimeter. A super-conducting solenoid, which surrounds both the tracking system and the LAr calorimeter, provides a uniform magnetic field of 1.15 T.

The Central Tracker. The central tracking device consists of six chambers in total which are housed in an aluminum tank. The main components are the two concentric drift chambers (CJC1, CJC2) with wires strung parallel to the beam axis. They cover the range of polar angles $15^\circ < \theta < 165^\circ$. The transverse momenta of charged particles

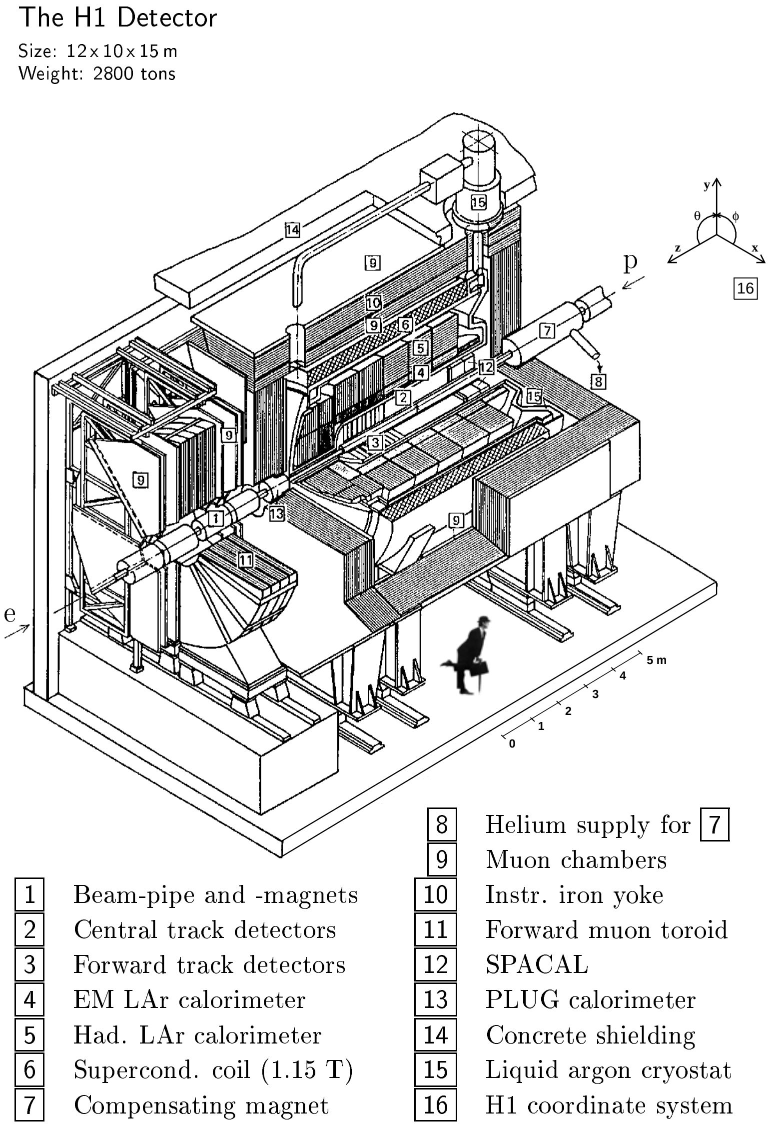

1	Beam-pipe and -magnets
2	Central track detectors
3	Forward track detectors
4	EM LAr calorimeter
5	Had. LAr calorimeter
6	Supercond. coil (1.15 T)
7	Compensating magnet
8	Helium supply for 7
9	Muon chambers
10	Instr. iron yoke
11	Forward muon toroid
12	SPACAL
13	PLUG calorimeter
14	Concrete shielding
15	Liquid argon cryostat
16	H1 coordinate system

Figure 5.2: An isometric view of the H1 detector

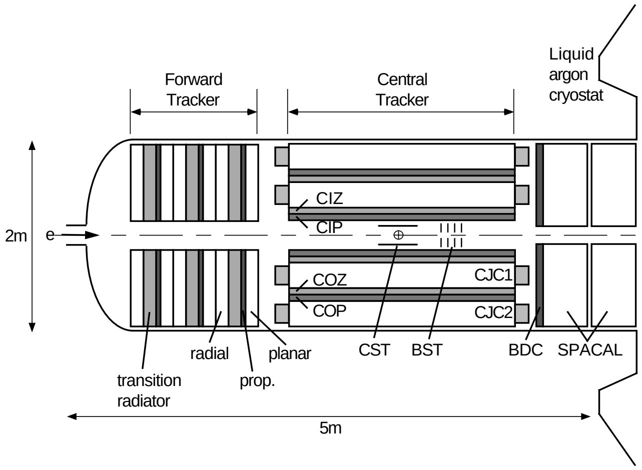

Figure 5.3: A side view of the tracking system and the backward calorimeter.

are measured with a resolution of $\delta p_{\perp}/p_{\perp}^2 < 0.01\,GeV^{-1}$. Two polygonal drift chambers with wires strung perpendicular to the beam axis improve the determination of the z coordinate and complement the measurement of the track momenta. These are the central inner and central outer z-chambers (CIZ, COZ) which are placed at radii of 18 cm (CIZ) and 47 cm (COZ), they achieve a z resolution of typically $300\mu m$. The central tracker is completed by two multi wire proportional chambers (MWPC), the central inner proportional chamber (CIP) and the central outer proportional chamber (COP), which deliver a fast trigger signal with a time resolution better than the 96 ns separation time between consecutive HERA bunch crossings. In this analysis the central tracking chambers are used to reconstruct the event vertex and to measure the momenta of charged particles in the hadronic final state. The backward drift chamber (BDC) is important for a precise measurement the scattered positron, needed for the calculation of the event kinematics.

The Forward Tracker. The forward tracking detector which covers the polar angles $5^\circ < \theta < 25^\circ$ is composed of a tracking chamber system comprising three identical modules aligned along the z direction. Each module consists of a planar drift chamber, a multi-wire proportional chamber, transition radiators, and a radial drift chamber. In the present analysis the forward tracking detector is only used in combination with the CJC.

5.5 Calorimeters.

The H1 calorimeter comprises four sub-detectors, each with full azimuthal acceptance, designed to measure the energy of final state particles. The liquid argon (LAr) calorimeter, the spaghetti calorimeter (Spacal), the tail catcher and the plug calorimeter. The main component is the LAr calorimeter which covers the central and the forward region, while the backward region is covered by the Spacal. The instrumented iron yoke of the magnet (the tail catcher) is used for muon identification and to provide a rough calorimetric measurement of hadronic particles leaking out of the LAr calorimeter. The plug calorimeter (not used in this analysis) closes the acceptance gap in between the LAr calorimeter and the beam pipe in the forward direction.

The Liquid Argon Calorimeter. In order to obtain as good an energy resolution as possible the finely segmented liquid argon (LAr) calorimeter has been placed inside the solenoid in order to reduce the amount of uninstrumented material that the particles have to traverse before they are absorbed in the calorimeter. The calorimeter consists of an electro-magnetic section and a hadronic section, both contained in a single liquid argon cryostat, and covers the polar angles 4° to 154°. It is segmented along the beam axis in eight self supporting wheels. The wheels are constructed from eight identical stacks or octants (figs. 5.4-5.5). The two forward wheels (IF1 and IF2 in fig. 5.4) are assembled as two half rings in an effort to minimize uninstrumented regions due to cracks. Every wheel of the LAr calorimeter is divided into an inner electro-magnetic section with lead absorber plates and an outer hadronic section with steel absorber plates (in both cases liquid argon is used as the active material). The most backward wheel, the BBE, has only an electro-magnetic section. Both sections are highly segmented in the transverse and longitudinal directions with about 44000 cells in total. The electro-magnetic part has a depth between 20 and 30 radiation lengths and the total depth of the LAr calorimeter varies between 4.5 and 8 hadronic interaction lengths depending on the polar angle. The energy resolution of the hadronic calorimeter is limited by fluctuations in the π° content on the hadronic shower and the unequal calorimeter response for electro-magnetic and hadronic energy. The charge output for hadrons is about 30% smaller than for leptons of the same energy. A weighting technique is employed online to correct for this effect. The

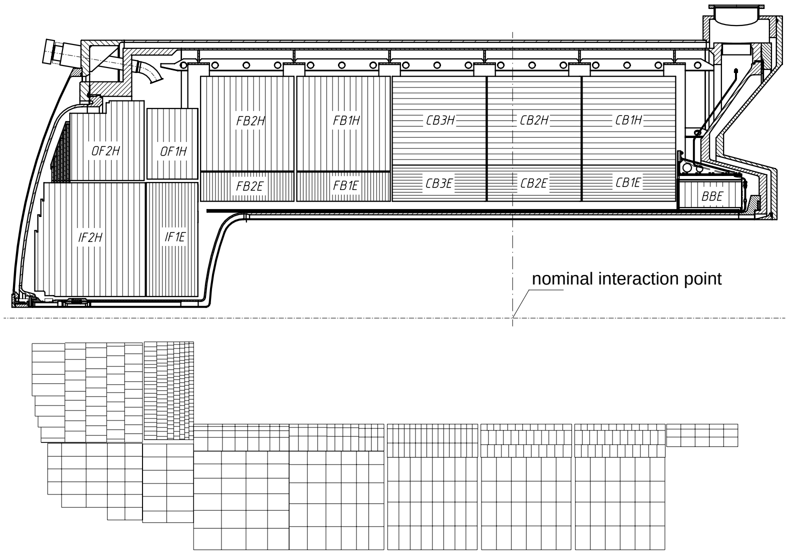

Figure 5.4: A side view of the H1 liquid argon calorimeter. The upper part shows the structure of the absorber plates, the lower part shows the cell structure.

LAr calorimeter is used in this analysis both to measure the total energy flow of the hadronic final state and for the measurement of the jets.

The Spacal. The backward region is instrumented with a lead/scintillating fiber calorimeter (Spacal), covering polar angles from (154° to 177.8°) with full azimuthal acceptance. It consists of an electro-magnetic and a hadronic section, the latter with a total depth of two hadronic interaction lengths. The primary task of this detector is to measure the energy and the direction of the scattered lepton but in this analysis it has also been used to measure the total hadronic energy flow in the backward direction.

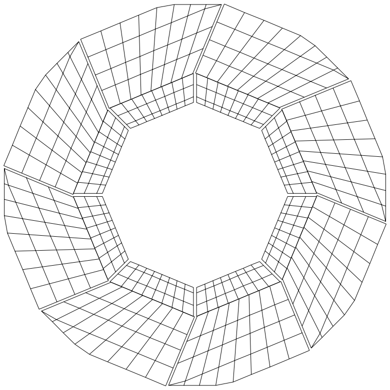

Figure 5.5: Radial view of the octant and cell structure of the CB1 ring of the H1 Liquid Argon calorimeter

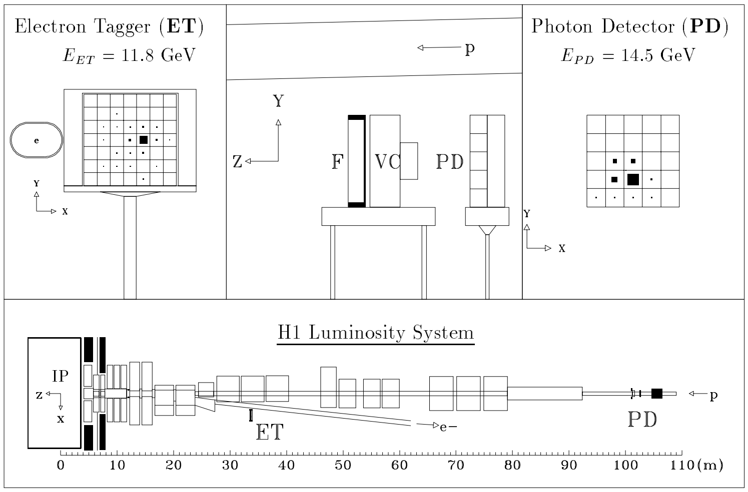

Figure 5.6: A Bethe-Heitler bremsstrahlung event measured in the H1 luminosity system.

5.6 Luminosity system.

The cross section of a given process $\sigma_{process}$ is related to the observed number of events produced in this process $N_{process}$ according to

$$\sigma_{process} = \frac{N_{process}}{\mathcal{L}_{int}}$$

where $\mathcal{L}_{int}$ denotes the integrated luminosity represented by the data set. The measurement of any cross section therefore requires a precise knowledge of $\mathcal{L}_{int}$. The integrated luminosity can be determined by measuring the event rate of a process with a well known cross section. In the H1 experiment the elastic bremsstrahlung $e + p \rightarrow e + \gamma + p$ (Bethe-Heitler process) is used for this purpose. Both, the scattered lepton and the emitted photon, are measured by two detectors installed close to the lepton beam in the HERA tunnel (fig. 5.6). The electron tagger (ET) and the photon detector (PD) are situated at z positions of 33.4 m and 102.8 m respectively.

5.7 Time of Flight Counters

Background induced by reactions of the proton beam with residual gas particles and interactions with the wall of the beam pipe far outside the detector can be rejected by using time-of-flight (ToF) information. For this purpose scintillators with a time resolution of 2-4 ns cover the end-caps of the detector at both ends. Based on the precise timing knowledge of the bunch crossings in the detector provided by the HERA machine (HERA clock), a distinction between signals from proton induced background outside the detector and genuine collision events is enabled.

5.8 Triggers.

The purpose of the trigger is to recognize, with the help of the detector information, real ep-events and to reject the background events. At HERA the lepton and the proton bunches collide with a frequency of 10.4 MHz. The expected rate of events from lepton-proton collisions is around hundred per second at the design luminosity whereas the background rates are in the kHz range. The largest contributions comes from proton gas interactions, synchrotron radiation originating from the lepton beam, and stray protons which produce particle showers by hitting the beam pipe.

The H1 trigger system used for the online selection consists of three active levels plus one level which is used in the online reconstruction step. After the application of the trigger, events are recorded at a rate of the order of 10 Hz.

5.9 Kinematic reconstruction.

Two different methods to reconstruct the event kinematics will be described. The first method, which has been used to select events for the analysis, is based on the knowledge of the beam energy, and the energy and direction of the scattered lepton.

$$Q^2 = (e - e')^2 \approx 2e \cdot e' \tag{5.1}$$

$$y_B = \frac{P \cdot q}{P \cdot e} = 1 - \frac{P \cdot e'}{P \cdot e} \tag{5.2}$$

Unfortunately this method is sensitive to bremsstrahlung from the leptons (see chapter 3), and will produce systematic effects if it is used to perform Lorentz-transformations. Therefore the hadronic energy flow, which is less sensitive to initial state radiation, is used to define y_B ([Bassler & Bernardi 1999]).

Recognizing that $P \cdot (P + q) = p \cdot h \ \Rightarrow \ P \cdot q \approx P \cdot h$ and that $P \cdot e \approx P \cdot h + P \cdot e'$ we have a modified y_B

$$y_B \approx \frac{P \cdot h}{P \cdot h + P \cdot e'} = \frac{h_-}{h_- + e'_-} \tag{5.3}$$

Even if this method is generally more reliable in performing Lorentz-transformations it does not reproduce inclusive quantities as well as the lepton method. The reason is that for events where a part of the hadronic final state particles disappears undetected in the beam pipe the value of y_B will be underestimated. By combining the two, selecting events using the lepton variables, and performing the Lorentz transform to the Breit system using Q^2 from the lepton method and y_B from the energy flows, we will achieve two things: A good description of the inclusive quantities, and secondly an isolation of the events with wrongly calculated Lorentz-transforms to low values of the scaled light-cone momentum, i^*_-, defined in eq. 4.4. If we would have used the lepton method for the transform there would be systematic errors in all bins of i^*_-.

On the left hand side of fig. 5.7 the relative resolution in Q^2 is shown. No systematic dependence is observed and the spread is 0.82.

On the right hand side of fig. 5.7 the resolution, defined as the absolute difference between detector and hadron level, is shown. For y_B the tail due to initial state radiation is visible from the lepton method, whereas it has more or less disappeared in the hadron method.

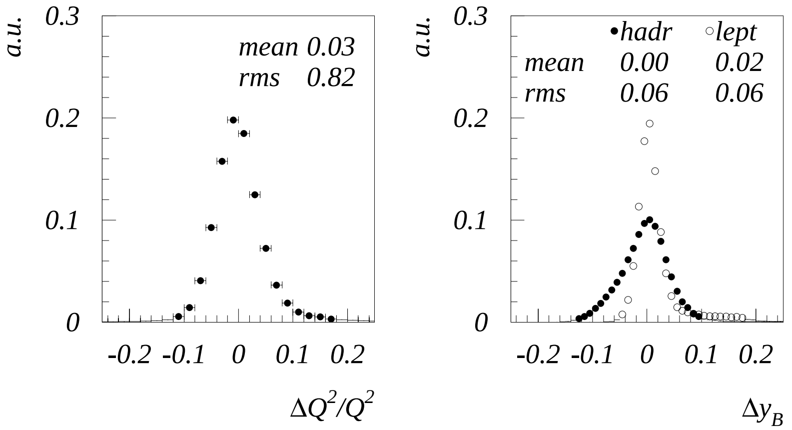

Figure 5.7: The resolution for the kinematic variables Q^2 left and y_B right. For Q^2 only the lepton method is shown. For y_B both the lepton-method (open circles) and the energy-flow method (filled circles) is shown.

5.10 Light-cone momentum and jets.

The scaled energy flow is calculated in the region of flat ϕ^* acceptance, defined inside the LAr calorimeter. If the measured scaled energy flow is required to be larger than 90% the resolution will depend entirely on the energy and spatial resolution of the LAr calorimeter, while for smaller fractions of the energy flow seen by the detector, it will also be sensitive to the resolutions of the Spacal calorimeter and to the loss of hadrons in the beam-pipe.

On the right of fig. 5.8 shows the relative resolution of i^*_- for events having $i^*_- > 0.9$. The resolution is defined as the difference between the detector level value minus the hadron level value divided by the hadron level value. We observe an average systematic displacement of 7% and a width of 0.18. This means that on average an event generated at 0.9 will migrate down to 0.84. The tail towards lower values tells that the migration goes predominantly in one direction we will have a rather pure sample in the bin reconstructed with $i^*_- > 0.9$.

On the left hand side of fig. 5.8 the relative resolution in $k^2_\perp/Q^2$ is plotted. It has a mean-value of zero but the distribution is very broad, with tails both towards lower and higher values.

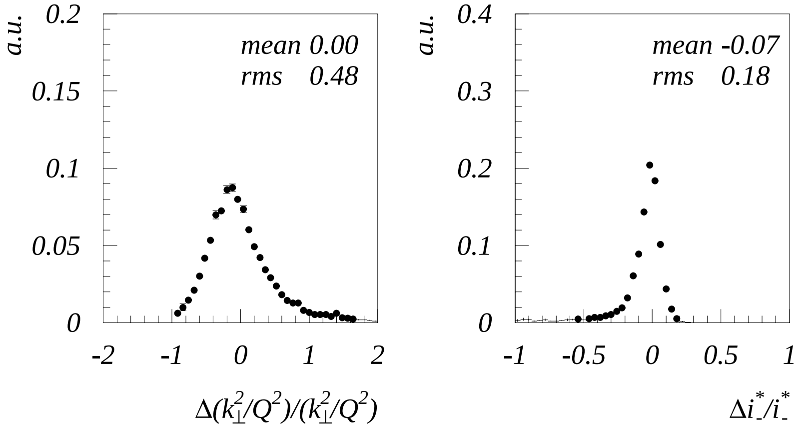

Figure 5.8: The resolution in $k_\perp^2/Q^2$ (lefthand plot) and in i_-^* (righthand plot), plotted for $i_-^* > 0.9$ and $k_\perp^2/Q^2 > 0.3$.

In fig. 5.9 the resolution in ϕ^* is shown for the case that 90scaled energy flow is measured. As expected the resolution comes out very good. The reconstruction of the angle is less sensitive to errors in the energy measurement since the measuring error probably effects *all* final state particles and thus the direction of the resulting four-vector remains more or less the same.

Although we have a very good resolution in the variable we want to measure, the resolution in the variables defining our kinematic bins is unfortunately less good. This calls for a complete unfolding of the data. For this purpose a general unfolding method has been developed.

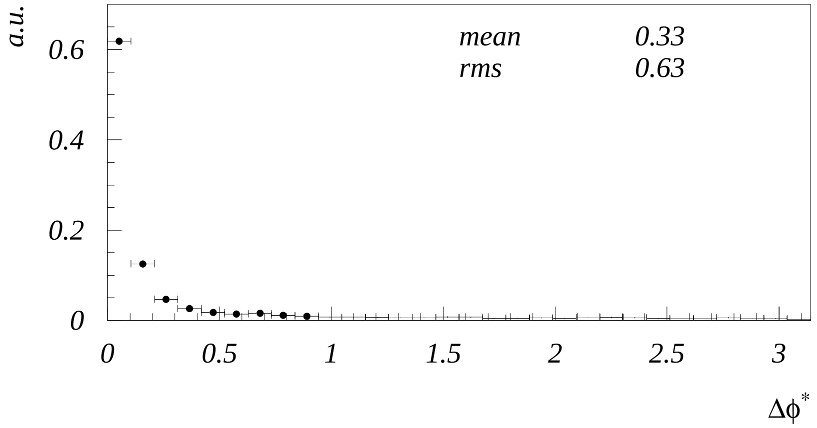

Figure 5.9: The resolution in ϕ^* defined as the absolute difference between the ϕ^* reconstructed on hadron level and the ϕ^* reconstructed on detector level, plotted for $i^*_- > 0.9$ and $k^2_\perp/Q^2 > 0.3$.

6

Detector corrections and unfolding.

6.1 Background.

In order to compare experimental data with predictions from models, it is necessary to compensate for detector effects like acceptance limitations, finite resolution, efficiencies etc. One method which has been used frequently is based on bin to bin corrections. The basic idea behind this method is that the interesting observable is extracted both on the hadron level and on the detector level with the help of simulation programs. The ratio between the values obtained on hadron and detector level provides the correction for each bin separately. The deficit of this method is that it does not consider the migrations between the bins, i.e. an event is generated in one bin and detected in another.

An improvement of this scheme is to do a maximum likelihood or χ^2-fit to the data, using the complete detector response. The advantage is that it can easily be extended to any number of dimensions and can take poor Monte Carlo statistics into account, as well as weighted events.

In this chapter the problem of deconvolution/unfolding will be treated. The two methods above will be described and a scheme to test and compare them will be developed. The tests are then carried out with special attention to model dependence and error calculations.

6.2 Detector response.

The unfolding problem is that a function $f(E)$ on the hadron level, which depends on the observable[*] E, has to be extracted from a measured distribution $g(E')$ where E' is the experimentally measured quantity. The transformation between $f(E)$ and $g(E')$ is given by the convolution integral:

$$g(E') = \int K(E', E) f(E) dE \tag{6.1}$$

---

[*] E is here any observable, and is taken to be dimensionless.

Where the kernel $K(E', E)$ is describing how the detector is transforming the observable $f(E)$ to the measured distribution $g(E')$. This is a classical integral-equation of the first-kind. There does not exist a unique way to solve it, but the solution has to be developed for each specific problem.

An accurate determination of the kernel, $K(E', E)$, is necessary for a meaningful analysis. This is, in our case, obtained from a Monte Carlo simulation in which the measuring properties of the various detector elements have been modeled. Through this kind of simulation the hadron and detector levels are known simultaneously on an event by event basis. What is explicitly known is however just the total distribution $r(E', E) = K(E', E)f(E)$ since we cannot separate the physics distribution $f(E)$ from the detector response without knowledge of the analytical form of both the total distribution $r(E', E)$ and $f(E)$.

6.3 A reformulation of the integral equation using histograms.

For a numerical solution of the convolution integral, the kernel $K(E', E)$ is represented as a two-dimensional histogram/matrix. This means that the integral in eq. 6.1 will be replaced by a sum over a number of bins integrating over each bin.

$$g(E') = \sum_{\beta} \int_{E_\beta} K(E', E) f(E) dE \tag{6.2}$$

where E_β indicates the integration over bin β on hadron level. The binning on detector level produces the additional integration over a bin α:

$$\int_{E'_\alpha} g(E') dE' = \sum_{\beta} \int_{E'_\alpha} \int_{E_\beta} K(E', E) f(E) dE dE'. \tag{6.3}$$

Since the functions are of unknown form the integrations cannot be performed analytically but are simply replaced by the bin content multiplied by the bin width. This is a correct procedure provided the functions $g(E')$ and $r(E', E) = K(E', E)f(E)$ can be written as odd functions with respect to the bin center, in each bin. It will later be necessary to bin also $f(E_\beta)$, and thus to assume that it, like g, is an odd function. This implies that $K(E', E)$ has to be an even function. Thus the detector response must be approximately symmetric in each bin, possibly described by a Gaussian distribution.

$$g_\alpha(E'_\alpha) \Delta E'_\alpha = \sum_{\beta} K(E'_\alpha, E_\beta) f(E_\beta) \Delta E_\beta \Delta E'_\alpha \tag{6.4}$$

where $\Delta E'_\alpha$ is the bin width and E'_α is the center of bin α. Rewriting this as a matrix equation renders

$$\bar{g} = \mathbf{K} \cdot \bar{f} \tag{6.5}$$

where the factors $\Delta E'_\alpha$ has been absorbed into the vector $\bar{g}$ and the matrix $\mathbf{K}$, and ΔE_β into the vector $\bar{f}$. This equation is exact under the constraints mentioned above.

To extract the distribution on hadron level, $\bar{h}_{data}$, which corresponds to the experimentally measured distribution, $\bar{d}_{data}$, we have to generate hadron level Monte Carlo data, $\bar{h}_{mc}$, and perform a detector simulation to get the corresponding detector level Monte Carlo distribution, $\bar{d}_{mc}$. The data histograms and the Monte Carlo histograms separately fulfill equation eq. 6.5 using the same kernel:

$$\bar{d}_{data} = \mathbf{K} \cdot \bar{h}_{data} \tag{6.6}$$

$$\bar{d}_{mc} = \mathbf{K} \cdot \bar{h}_{mc} \tag{6.7}$$

where the kernel $\mathbf{K}$ has to be determined from eq. 6.7 if we are going to be able to solve eq. 6.6.

6.4 Bin-to-bin corrections.

First we will study an approximate determination of $\mathbf{K}$. We start by left-multiplying both eq. 6.7 and eq. 6.6 with the inverse of $\mathbf{K}$

$$\bar{h}_{data} = \mathbf{K}^{-1} \cdot \bar{d}_{data} \tag{6.8}$$

$$\bar{h}_{mc} = \mathbf{K}^{-1} \cdot \bar{d}_{mc}. \tag{6.9}$$

We then have to find $\mathbf{K}^{-1}$ using $\bar{h}_{mc}$ and $\bar{d}_{mc}$, and with the assumption that the off-diagonal elements in $\mathbf{K}$ are small compared to the diagonal we can, as a “zeroth-order” approximation, write eq. 6.9 as†:

$$\mathbf{diag}(\bar{h}_{mc}) \approx \mathbf{K}^{-1} \cdot \mathbf{diag}(\bar{d}_{mc}). \tag{6.10}$$

Right-multiplying with the inverse of the detector level histogram leads to:

$$\mathbf{K}^{-1} \approx \mathbf{diag}(\bar{h}_{mc}) \cdot \mathbf{diag}(\bar{d}_{mc})^{-1}. \tag{6.11}$$

Inserting this expression for $\mathbf{K}^{-1}$ into eq. 6.8 renders:

$$\bar{h}_{data} = \mathbf{diag}(\bar{h}_{mc}) \cdot \mathbf{diag}(\bar{d}_{mc})^{-1} \cdot \bar{d}_{data} \tag{6.12}$$

[†] The notation $\mathbf{diag}(\bar{v})$, mean the diagonal matrix whose elements are the vector $\bar{v}$.

which is a so-called bin-to-bin correction. It is commonly used but, as can be seen, suffer from the fact that no knowledge concerning the off-diagonal elements in K is used. The bin-to-bin correction will, in the last section of this chapter, be contrasted to a more refined solution, which takes the off-diagonal elements into account.

6.5 A solution taking the migrations into account.

The first step is to consider the two-dimensional histogram $\mathbf{r}_{mc}$, which has the detector level stored as a function of the hadron level. This histogram contains in its elements all information concerning the migration from one bin on hadron level to another detector level, but it also contains the physical input-distribution, $\bar{h}_{mc}$ from the Monte Carlo generation. It can symbolically be written as

$$\mathbf{r}_{mc} = (\mathbf{Kh})_{mc}. \tag{6.13}$$

If, as mentioned above, the detector response is even with respect to the bin-center, and the physical input is odd, we can divide $\bar{h}_{mc}$ away by right-multiplying eq. 6.13 with the inverted hadron level histogram, $\mathbf{diag}(\bar{h}_{mc})^{-1}$, to isolate $\mathbf{K}$

$$\mathbf{K} \approx (\mathbf{Kh})_{mc} \cdot \mathbf{diag}(\bar{h}_{mc})^{-1} = \mathbf{r}_{mc} \cdot \mathbf{diag}(\bar{h}_{mc})^{-1}. \tag{6.14}$$

We now invert eq. 6.14 and insert into eq. 6.8

$$\bar{h}_{data} = \mathbf{diag}(\bar{h}_{mc}) \cdot \mathbf{r}_{mc}^{-1} \cdot \bar{d}_{data} \tag{6.15}$$

This is a numerically exact solution which, however, suffers from the fact that statistical fluctuations in the bins of $\mathbf{r}_{mc}$ where the statistics is small can be amplified by the inversion [Blobel 1984]. The first improvement is to do a χ^2-fit, which will find the most probable solution, using a Gaussian interpretation of the errors. This require different numbers of bins on hadron and detector level, in order for the number of degrees of freedom to be non-zero. This can be achieved by simply dividing each hadron level bin in two on detector level, or by studying where the migrations are largest and introduce extra bins in those regions. To calculate the χ^2 we also need to introduce the covariance-matrix, $\mathbf{C}$, containing the summed error of the measured data and the Monte Carlo data in each detector level bin:

$$\chi^2 = (\bar{d}_{data} - \mathbf{K} \cdot \bar{h}_{data})^T \cdot \mathbf{C^{-1}} \cdot (\bar{d}_{data} - \mathbf{K} \cdot \bar{h}_{data}). \tag{6.16}$$

If the Monte Carlo data has comparable errors to the measured data this formulation is difficult to solve numerically for a problem with many bins and will be improved in the next section.

6.6 χ^2 vs. log-likelihood.

The normal χ^2 method has a deficit which has to be resolved. When both coordinates have errors, the χ^2 will, for a single bin, have the following limiting behavior:

$$\chi^2 = \frac{(y-ax)^2}{\sigma_y^2 + a^2\sigma_x^2} \quad \underset{a \to \pm\infty}{\longrightarrow} \quad \frac{x^2}{\sigma_x^2} \tag{6.17}$$

which makes it very difficult to minimize. A minimizer can very easily be stuck at very large absolute values on a since the χ^2 function is more or less flat there. For a problem with many bins the χ^2 will be almost impossible to minimize. Using a log-likelihood formulation introduces an additional term by which the limiting behavior of the χ^2 is avoided. Assuming uncorrelated errors the log-likelihood is written as:

$$\mathcal{L} = \frac{(y-ax)^2}{\sigma_y^2 + a^2\sigma_x^2} + \log(\sigma_y^2 + a^2\sigma_x^2) \quad \underset{a \to \pm\infty}{\longrightarrow} \quad +\infty \tag{6.18}$$

where the last term ensures that $\mathcal{L}$ goes to infinity in the limit of large a. This behavior makes the minimization much more reliable than the χ^2 method since all parameters will be limited to reasonable values.

6.7 Maximum likelihood formulation.

The integral-equation can now be formulated as log-likelihood expression

$$\mathcal{L} = (\bar{d}_{data} - \mathbf{K} \cdot \bar{h}_{data})^T \cdot C^{-1} \cdot (\bar{d}_{data} - \mathbf{K} \cdot \bar{h}_{data}) + \log|C| \tag{6.19}$$

which, in a more explicit notation, can be written as (again assuming uncorrelated errors):

$$\mathcal{L} = \sum_\alpha \left\{ \frac{(d_\alpha - \sum_\beta K_{\alpha\beta} h_\beta)^2}{\sigma_{d_\alpha}^2 + \sum_\beta \sigma_{K_{\alpha\beta}}^2 h_\beta^2} + \log(\sigma_{d_\alpha}^2 + \sum_\beta \sigma_{K_{\alpha\beta}}^2 h_\beta^2) \right\} \tag{6.20}$$

which should be minimized with respect to the parameters h_β. This is achieved with a normal Newton procedure using the derivatives to iteratively find the best minimum, [Press, Teukolsky, Vetterling & Flannery 1992, John E. Dennis & Schnabel 1996].

6.8 Orthogonal functions.

In the previous sections we have treated the case where the functions in the original integral equation, eq. 6.1, are unknown and therefore were replaced by histograms. However, if the form of these functions are known we can find an analytic solution to the equation. In the present measurement we are dealing with a Fourier cosine-series containing three terms and we will in this section develop a solution for this case. It will be shown that the equation has an exact solution, and that it can be formulated as a matrix-equation similar to the one found in eqs. 6.6-6.7.

We start with:

$$d(\phi') = \int K(\phi', \phi) h(\phi) d\phi \tag{6.21}$$

where the functions $d(\phi')$ and $h(\phi)$ now are known to be cosine series in the variables ϕ' and ϕ, respectively, containing three terms:

$$(d_0 + d_1 \cos\phi' + d_2 \cos 2\phi') = \int K(\phi', \phi)(h_0 + h_1 \cos\phi + h_2 \cos 2\phi) d\phi \tag{6.22}$$

Studying the equation we firstly conclude that we can write the kernel as a function of the three moments in $\cos i\phi'$ times general functions of ϕ; $K(\phi', \phi) = k_0(\phi) + k_1(\phi)\cos\phi' + k_2(\phi)\cos 2\phi'$. If we expand the functions k_i in cosine series in ϕ we can write the kernel as:

$$K(\phi', \phi) = \sum_{i=0}^{2}\sum_{j=0}^{2} k_{ij} \cos(i\phi') \cos(j\phi). \tag{6.23}$$

This kernel will be multiplied by the hadron level function $h(\phi) = (h_0 + h_1 \cos\phi + h_2 \cos 2\phi)$ and then integrated over ϕ. Using the fact that the terms in a Fourier series are orthogonal to each other the mixed products, for example the $\cos\phi$ term from the kernel times the $\cos 2\phi$ term from h, will integrate to zero. We can thus write the first step in the integration as:

$$\begin{aligned}
&\int K(\phi', \phi)(h_0 + h_1 \cos\phi + h_2 \cos 2\phi) d\phi = \\
&\qquad \int (k_{00} h_0 + k_{01} h_1 \cos^2\phi + k_{02} h_2 \cos^2 2\phi) d\phi + \\
&\qquad \int (k_{10} h_0 + k_{11} h_1 \cos^2\phi + k_{12} h_2 \cos^2 2\phi) d\phi \cos\phi' + \\
&\qquad \int (k_{20} h_0 + k_{21} h_1 \cos^2\phi + k_{22} h_2 \cos^2 2\phi) d\phi \cos 2\phi'.
\end{aligned} \tag{6.24}$$

We see the that the natural way to reformulate this into a matrix equation is by using the moments in $\cos i\phi'$ and $\cos j\phi$ as coordinate axes and regard the equation as a linear transformation from one coordinate system to another. Performing the integrals in eq. 6.24, dropping the explicit notation with $\cos i\phi'$ and $\cos j\phi$ produces:

$$\begin{pmatrix} d_0 \\ d_1 \\ d_2 \end{pmatrix} = \pi \begin{pmatrix} 2k_{00} & k_{01} & k_{02} \\ 2k_{10} & k_{11} & k_{12} \\ 2k_{20} & k_{21} & k_{22} \end{pmatrix} \begin{pmatrix} h_0 \\ h_1 \\ h_2 \end{pmatrix} . \tag{6.25}$$

This equation can be written exactly as eq. 6.6:

$$\bar{d}_{data} = \mathbf{K} \cdot \bar{h}_{data} \tag{6.26}$$

where the normalization factor π has been absorbed in $\mathbf{K}$.

The only difference from the formulation in eq. 6.6 is that eq. 6.26 is an exact solution whereas in the case of histograms a number of constraints have to be imposed to make it correct.

The interpretation of the elements in $\mathbf{K}$ is straight-forward. The diagonal elements is the detector resolution for that moment and the off-diagonal elements represent noise or systematic effects.

In chapter 4 we concluded that a high scaled energy flow i^*_- is crucial for a good resolution in ϕ^*. However, in chapter 5 we saw that the resolution in i^*_- is not good enough to perform a cut in this variable. We will therefore use a two dimensional formulation of the unfolding method we have developed here. This is straight forward since the histogram formulation, eq. 6.6, which will be used for the energy flow and the orthogonal formulation, eq. 6.26, which will be used for the ϕ^* modulations are identical.

6.9 Test procedure.

The purpose of the test procedure is to check the error-calculation, and any systematic effects stemming from the differences between the Monte Carlo and the data. Normally full hadronic final-state generators are used to generate single events, which then are going through a detailed simulation of the detector. This sets statistical limits to the number of models which can be simulated. A faster way is to use a typical parameterization of a detector resolution to achieve a analytic formulation of the kernel. For example the calorimeter resolution can typically be

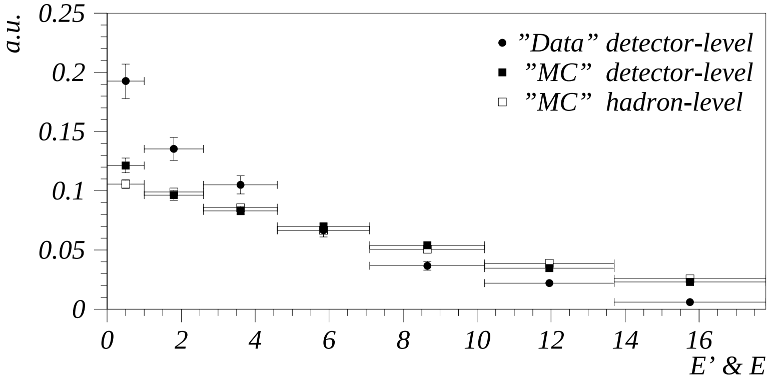

Figure 6.1: Distributions in the variables E and E' for one of the generated sets. The histogram representing the measured data on detector level is shown as filled circles, and the histograms representing Monte Carlo data are shown on detector level as filled squares and on hadron level as open squares. For comparison all three histograms are normalized to unity.

written as $x/\sqrt(E)$, which gives the kernel:

$$K(E',E) = \frac{1}{\sqrt{2\,\pi\,x^2E}} e^{-\frac{1}{2}\frac{(E-E')^2}{x^2E}} \tag{6.27}$$

and convolute that with a typical energy distribution

$$f(E) = ae^{-aE}. \tag{6.28}$$

We thus have a analytic expression for the total distribution $r(E',E) = K(E',E)f(E)$. This function is then sampled on a fine-grained grid, and a number of events is generated directly in each node. This is a fairly fast procedure and can therefore be repeated to test how sensitive the different solutions of the integral equation are to the input distribution $f(E)$ and to statistical fluctuations. As an example one set of histograms are shown in fig. 6.1. The detector resolution was set to $50\%/\sqrt{E}$. The unfolding uses twice as many bins on detector level (not shown) as on hadron level. For the measured data $a = 0.2$ and for the Monte Carlo data $a = 0.1$.

6.10 Results.

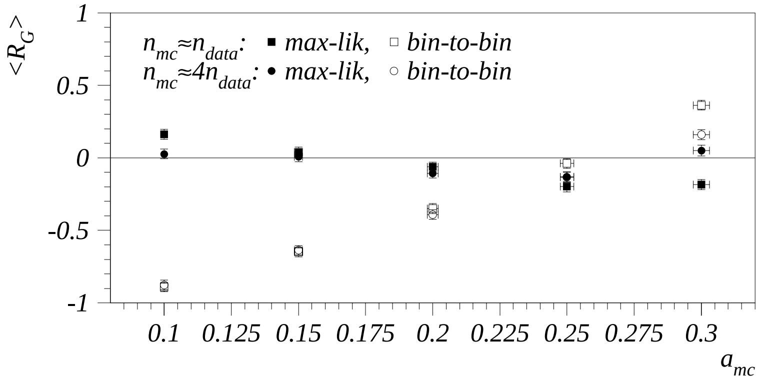

Figure 6.2: The mean of the Gaussian residuals plotted versus a_{mc} for the maximum likelihood method (filled circles and filled squares) and for bin-to-bin corrections (open circles and open squares). The two cases of Monte Carlo statistics equal to the data sample, $n_{mc} \approx n_{data}$, and Monte Carlo statistics four times the data sample, $n_{mc} \approx 4n_{data}$, are compared.

For the results 1000 times two sets of histograms were generated. One set was representing the measured data, whereas the other set represented the Monte Carlo data. The measured data was then corrected for detector effects using bin-to-bin correction according to eq. 6.12, and using the maximum likelihood method according to eq. 6.19. An exponential was then fitted to each corrected histogram, and the parameter a_c was extracted with errors.

To check the systematic dependence two things were varied, the number of entries in the Monte Carlo histograms was set to 1000 and 4000, and the mean value in eq. 6.28 was set to $a_{mc} = \{0.1, 0.15, 0.2, 0.25, 0.3\}$. The data was kept fixed at 1000 entries and $a = 0.2$. For the bin-to-bin correction the overlap, the number of events which occur in the same bin on hadron as on detector level, was between 60% and 80%, and the correction factors were between 0.9 and 1.1.

The results are studied by plotting the Gaussian residuals

$$R_G = \frac{a_c - a}{\sigma_c^2} \tag{6.29}$$

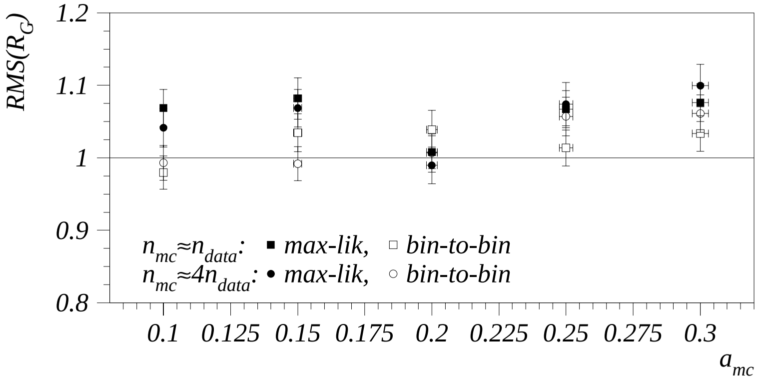

Figure 6.3: The RMS of the Gaussian residuals plotted versus a_{mc} for the maximum likelihood method (filled circles and filled squares) and for bin-to-bin corrections (open circles and open squares). The two cases of Monte Carlo statistics equal to the data sample, $n_{mc} \approx n_{data}$, and Monte Carlo statistics four times the data sample, $n_{mc} \approx 4n_{data}$, are compared.

and the relative residuals

$$R_r = \frac{a_c - a}{a}, \tag{6.30}$$

where a_c is the corrected value, and a is the true.

For R_G the mean should be zero and the RMS one, where a deviation in the RMS indicates a problem in the error-calculation and a deviation in the mean shows the systematic error made. Any systematic dependence should also be visible in the mean of R_r, as a percentage of the true a.

As can be seen in fig. 6.3, the error calculation is good for both methods, but fig. 6.2 and fig. 6.4 show that there is a rather large systematic dependence in case of the bin-to-bin correction. This comes from the fact that the off-diagonal elements are too large for the actual resolution.

There is also a systematic dependence for the maximum likelihood fit (fig. 6.2 and fig. 6.3), stemming from the fact that the constraints defined in section 6.3 are not completely fulfilled. The bins are so large that the function cannot be approximated as odd. If the bin-size is decreased some bins become so depopulated that the Gaussian approximation fails.

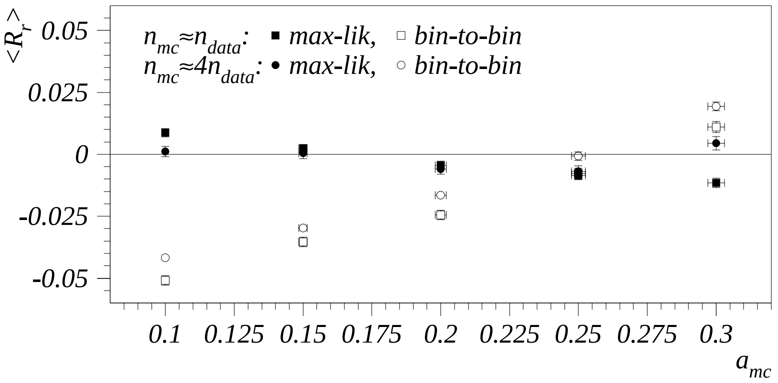

Figure 6.4: The mean of the relative residuals plotted versus a_{mc} for the maximum likelihood method (filled circles and filled squares) and for bin-to-bin corrections (open circles and open squares). The two cases of Monte Carlo statistics equal to the data sample, $n_{mc} \approx n_{data}$, and Monte Carlo statistics four times the data sample, $n_{mc} \approx 4n_{data}$, are compared.

This is a rather typical problem connected to balancing the detector resolution and the statistics in the definition of the bin size.

7

The measurement.

7.1 Introduction.

We will now put the results of the previous chapters together and extract the azimuthal asymmetries. The discussion will start with a description of the selections criteria for the measured data sample and the Monte Carlo samples used for the detector corrections. A comparison between the data and the Monte Carlo sample of the basic kinematic quantities will be performed on detector level before we continue with a thorough discussion of the jet reconstruction on detector level. A number of quantities will be studied to ensure that the Monte Carlo program Rapgap can be used for the detector corrections.

In the two final sections the unfolding of the measured data to hadron level will be performed according to the method described in chapter 6. The final results will be presented and compared to Monte Carlo predictions.

7.2 Basic quantities on detector level.

The analysis uses data taken 1997, comprising 294041 events which corresponds to an integrated luminosity of $15.3\,pb^{-1}$. The event selection requires an electron in the Spacal-detector with the following characteristics:

$$\begin{array}{ccccc} 10\ GeV & < & E_{elec} & & \\ 156^\circ & < & \theta_{elec} & < & 176^\circ \\ 10\ GeV^2 & < & Q^2 & < & 100\ GeV^2 \\ 0.2 & < & y_B & < & 0.65 \end{array}$$

where the Q^2 and y_B are calculated from the scattered lepton and the nominal energy of the lepton beam as described in chapter 5. Thereafter y_B is recalculated from the hadronic energy flow to achieve a minimal systematic error in the Lorentz transformation to the Breit system.

The Monte Carlo generator Rapgap 4.06, with a parameterization of the structure function according to CTEQ-4m, was used to perform the

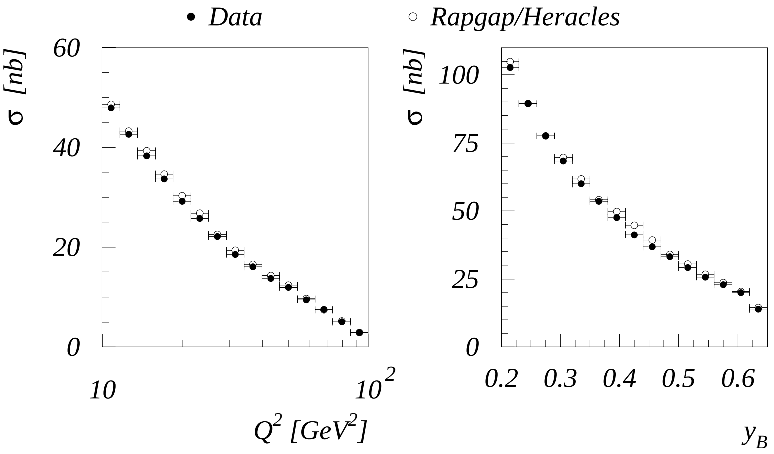

Figure 7.1: The Q^2 distribution (left) and y_B distribution (right). The measured data (filled circles) are compared to the simulated Monte Carlo sample (open circles).

detector corrections. In order to save space and time a weighting procedure was applied to reduce the sample designated for detector simulation. This was achieved by weighting the generated Monte Carlo events such that the events are almost equally distributed over the whole phase space region, which means a suppression of events at low y, low Q^2 and with low jet transverse momenta. The events were kept with a probability $p = min(1, (1 + Q^2 y_B + p_\perp^{*2})/100)$, where Q^2 and y_B were taken from the generator output and $p_\perp^{*2}$ was calculated from the partons of the leading order matrix element in the hadronic cms. In case of a lowest order event, QPM, $p_\perp^{*2}$ was set to zero. A sample of 2343687 events resulted in 307257 events after applying the weights. This Monte Carlo sample, which corresponds to an integrated luminosity of $115.5\,pb^{-1}$, was sent through a detailed detector simulation. An unweighted sample of 8220951 events corresponding to $342.2\,pb^{-1}$ was generated and used as reference for the hadron level.

On the left hand side of fig. 7.1 the cross-section is plotted as a function of Q^2 for the measured data sample, filled circles, and the simulated Monte Carlo sample, open circles. On the right hand side the cross-section is plotted as a function of y_B for the same samples. The Monte Carlo is giving an accurate description of both variables both in shape and absolute normalization.

7.3 The jets.

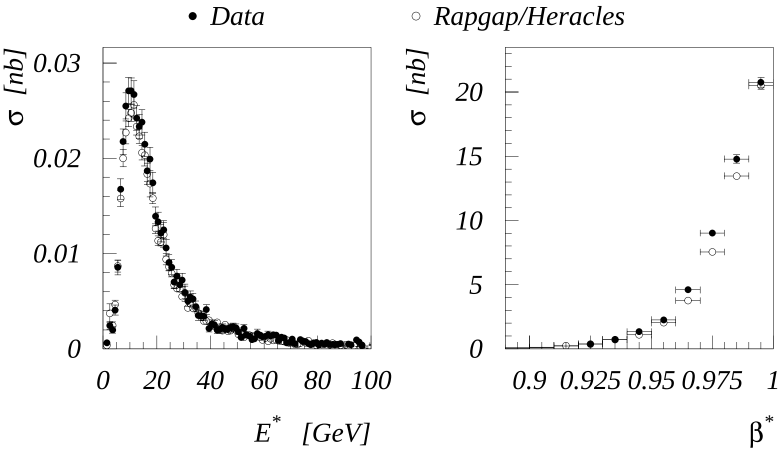

Figure 7.2: The energy distribution (left) and the beta distribution (right) for the backward jet in events with $i_-^* > 0.9$ and $k_\perp^2/Q^2 > 0.3$. The measured data (filled circles) are compared to the simulated Monte Carlo sample (open circles).

The $k_\perp$-algorithm is applied to both samples as described in chapter 4 in order to make sure that the Monte Carlo sample is giving a good description of the jets found in the data. We have chosen to study five key jet variables which should be sensitive to possible discrepancies. In this section we will only discuss events with $i_-^* > 0.9$ and $k_\perp^2/Q^2 > 0.3$. A complete set of plots for all energy flow bins and for all cutoff values is shown in appendix D, giving mean values and variances for the key variables.

In fig. 7.2 the energy and β^* distributions of the backward jet, for events with $i_-^* > 0.9$ and $k_\perp^2/Q^2 > 0.3$, are shown. Both variables are measured in the Breit system. Beta is the dimensionless velocity of the jet defined as $\beta^* = P^*/E^*$. Both distributions are well described, both in shape and normalization, telling that both the energy and the momentum of the jets are correctly generated by the Monte Carlo program.

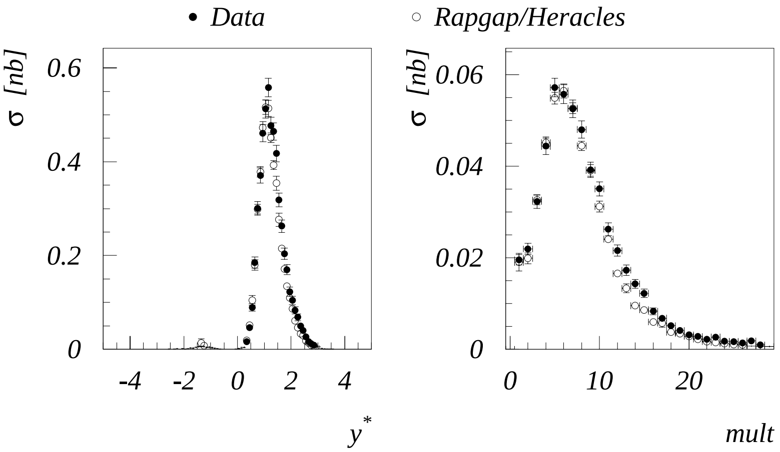

Figure 7.3: The rapidity distribution (left) and multiplicity distribution (right) of the backward jet in events with $i^*_- > 0.9$ and $k_\perp^2/Q^2 > 0.3$. The measured data (filled circles) are compared to the simulated Monte Carlo sample (open circles).

The spatial location of the jets must be established in the Breit-system. In fig. 7.3 the rapidity and multiplicity distributions of the backward jet, for events with $i^*_- > 0.9$ and $k_\perp^2/Q^2 > 0.3$, are shown. The rapidity is defined in the Breit system. From the rapidity distribution we learn that the position in the Breit system is very well described. The multiplicity, or the number of four-vectors assigned to the jets, is of course sensitive to the QCD effects but also to effects in the detector. Shower evolution, Bremsstrahlung and scattering will thus influence the jet reconstruction and these effects should therefore be correctly reproduced by the Monte Carlo data. It is clear from the plots that Rapgap-generated data which have gone through a detailed simulation of the H1 detector are in very good agreement with the experimental data.

Finally in fig. 7.4 we see the azimuthal distribution for jets in events with $i^*_- > 0.9$ and $k_\perp^2/Q^2 > 0.3$. It is normalized to cross-section and the Monte Carlo is also here giving very accurate description of the shape. The overall cross-section in the Monte Carlo is within 4% of the data.

In fig. 7.5 and fig. 7.7 two two-jet events are presented in a longitudinal (r-z) and transversal (x-y) view of the detector. The same events are also shown in fig. 7.6 and fig. 7.8 as lego-plots in the $\eta - phi$ plane

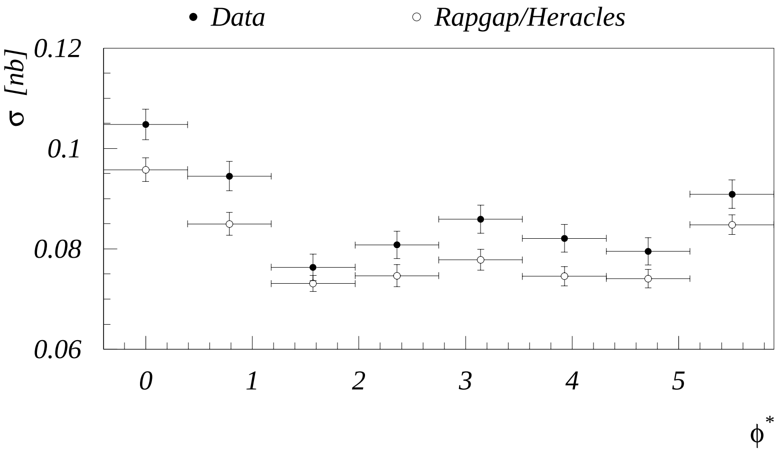

Figure 7.4: The distribution of the azimuthal angle for jets in events with $i^*_- > 0.9$ and $k_\perp^2/Q^2 > 0.3$. The measured data (filled circles) are compared to the simulated Monte Carlo sample (open circles).

of the detector, together with the kinematics of the events and the jet variables.

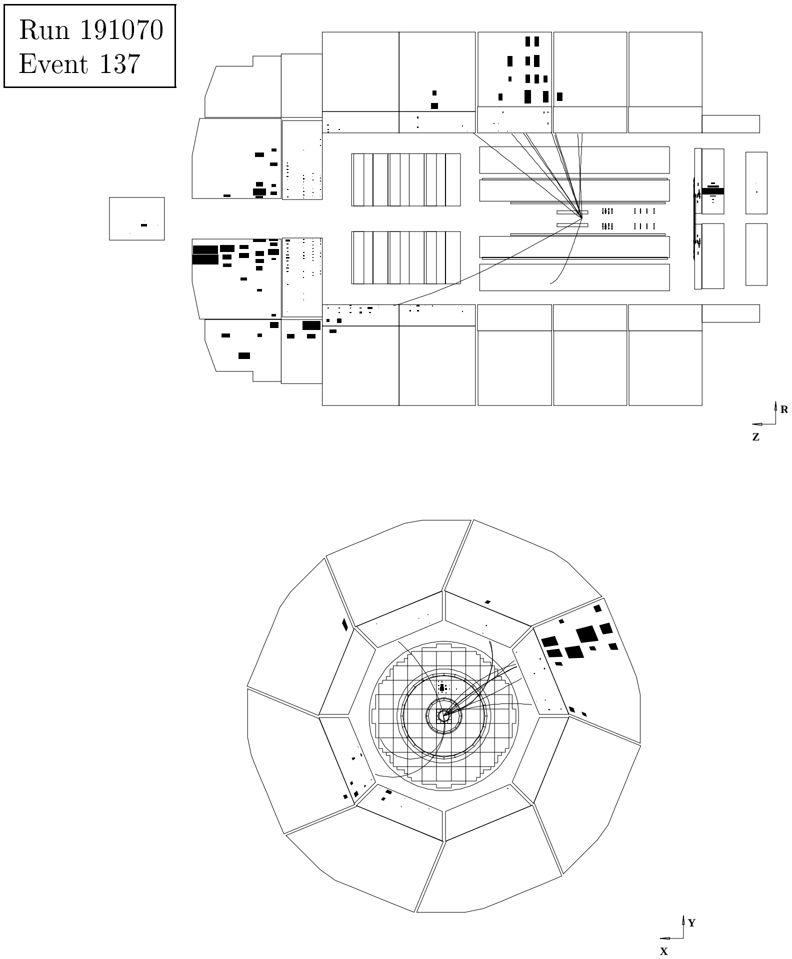

Figure 7.5: A deep-inelastic two-jet event as registered by the detector. The upper figure shows the $r - z$ projection of the LAr-calorimeter, the tracking system and the SPACAL. The scattered lepton is observed in the SPACAL, the backward jet is going upward and the forward jet downward. In the lower figure the $x - y$-projection of the barrel-region of the LAr-calorimeter is shown together with the SPACAL and the particle tracks. The two LAr wheels in the forward direction are not incorporated into the $x - y$ projection. The backward jet is here at 2 o'clock and the forward jet is at 7 o'clock.

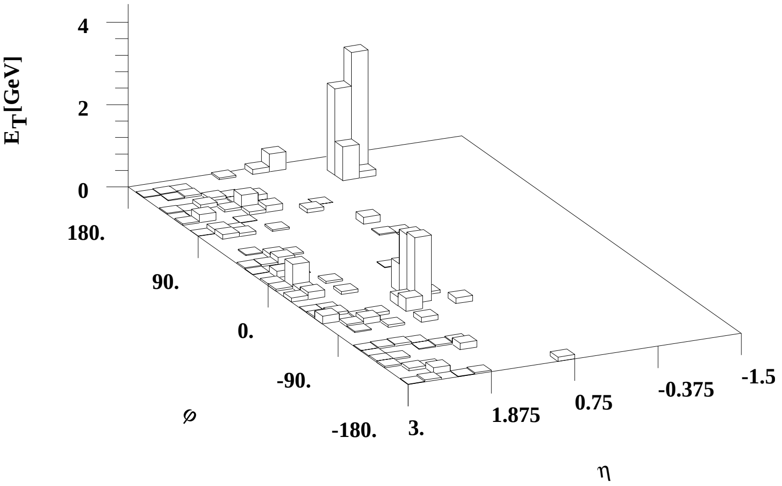

Run 191070 Event 137

$Q^2 = 28.9\ GeV^2$ $x_B = 0.0024$

$k_\perp^2/Q^2 = 0.83$ $i_-^* = 0.97$

$\phi^* = 44.0°$

Figure 7.6: The E_T weighted $\eta - \phi$ laboratory projection for the same event as in fig. 7.5, is shown together with the kinematic- and jet-variables of the event.

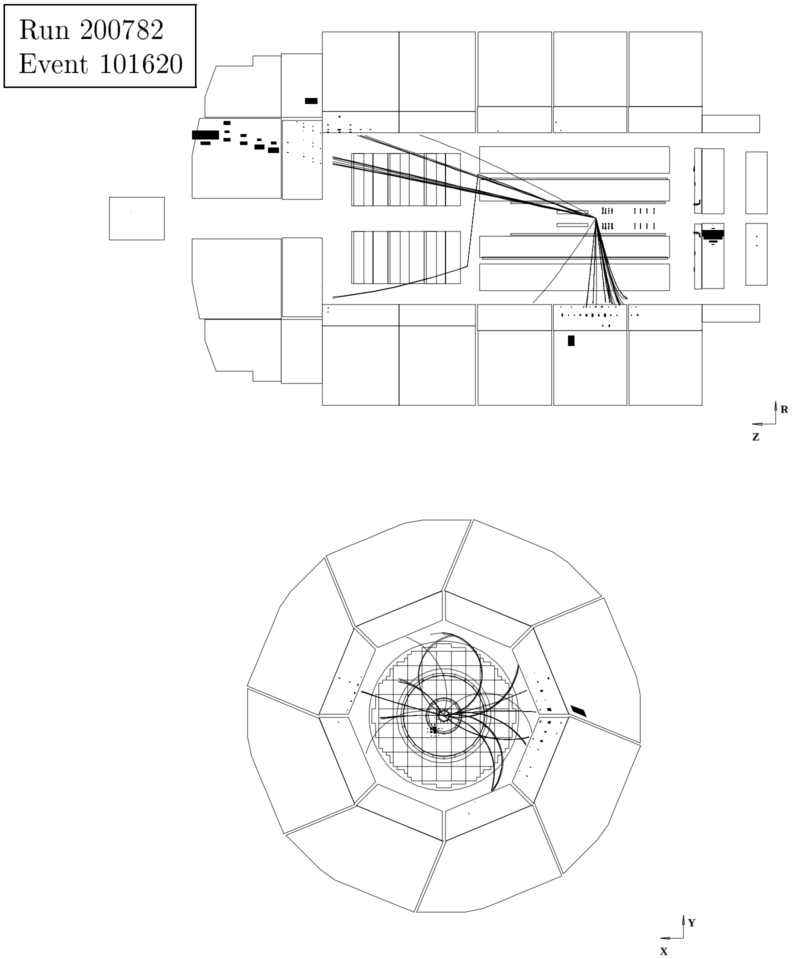

Figure 7.7: Another deep-inelastic two-jet event presented as in fig. 7.5 The scattered lepton is in the SPACAL and the backward jet is downward in the $r-z$-projection and right in the $x-y$-projection.

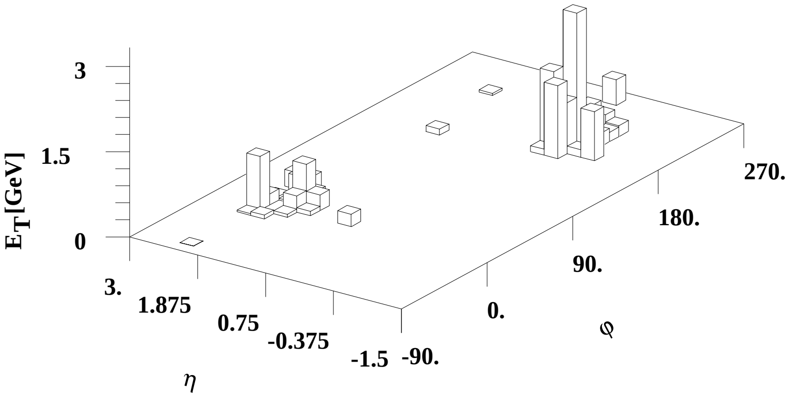

Run 200782	Event 101620
$Q^2 = 12.8\ GeV^2$	$x_B = 0.00069$
$k_\perp^2/Q^2 = 0.62$	$i_-^* = 0.92$
$\phi^* = 255.5°$	

Figure 7.8: The E_T weighted $\eta - \phi$ laboratory projection for the same event as in fig. 7.7, is shown together with the kinematic- and jet-variables.

7.4 The jet cross-section on detector level.

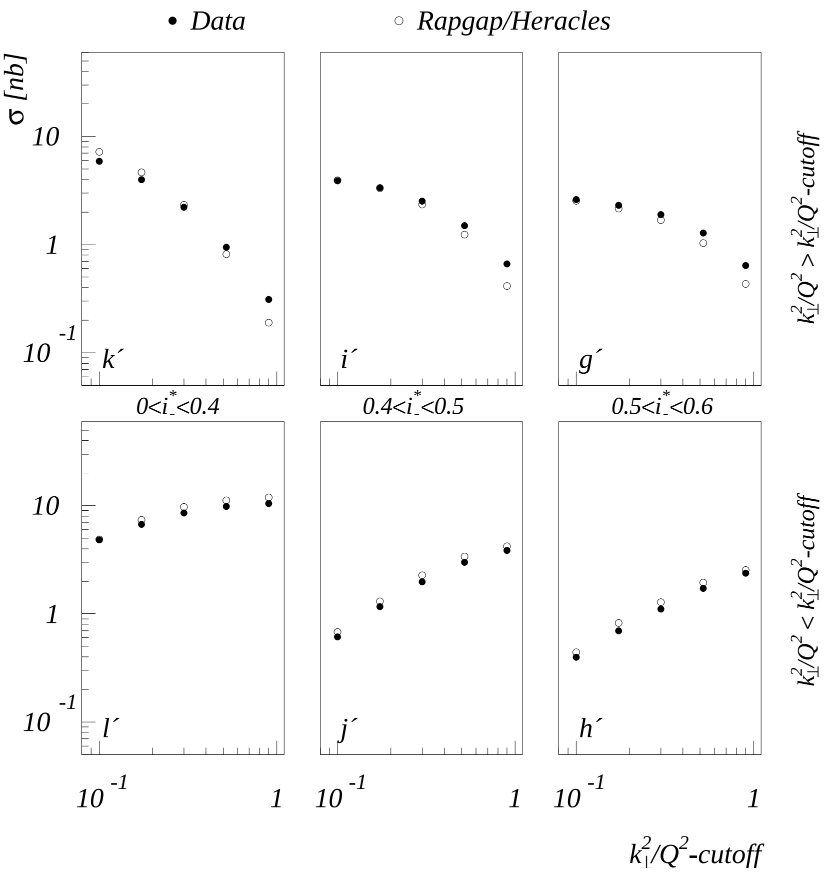

Figure 7.9: The jet cross-section on detector level as a function of the $k_\perp^2/Q^2$-cutoff at low energy-flows. The error bars only include statistical errors.

In figs. 7.9-7.10 the jet cross-sections for data and Monte Carlo are shown. Compared to the hadron-level plots in figs. 4.5-4.6 the bins in the energy-flow parameter on the detector-level have been subdivided into twice as many bins. This is necessary in order to provide the unfolding with the degrees of freedom needed to perform the fit.

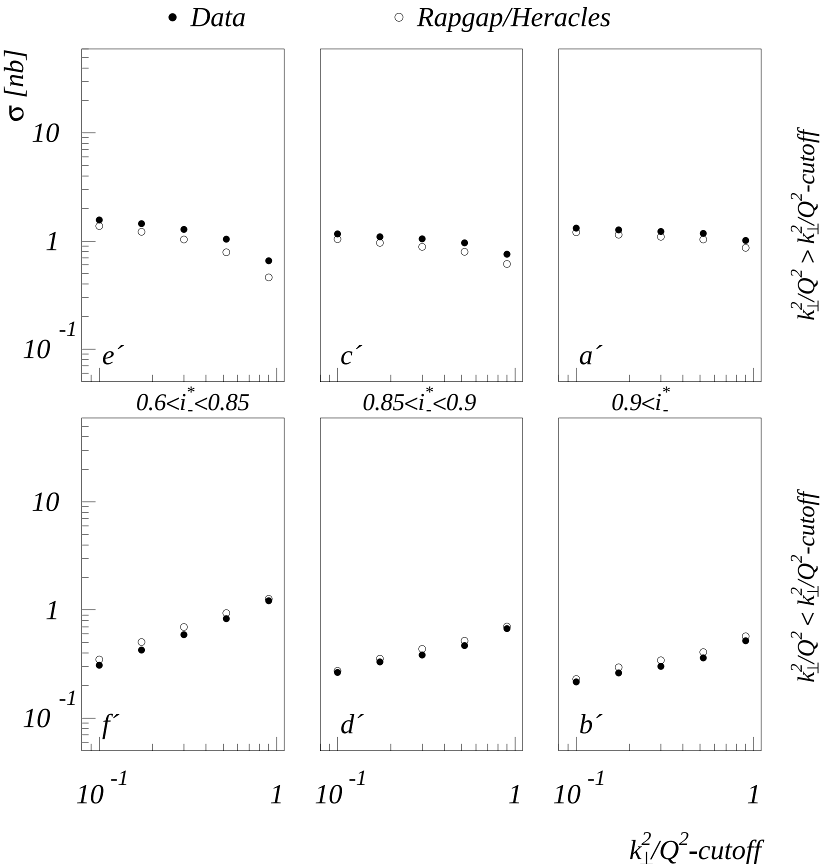

Figure 7.10: The jet cross-section on detector level as a function of the $k_\perp^2/Q^2$-cutoff at high energy-flows. The error bars only include statistical errors.

The important high energy flow bins in fig. 7.10 is extremely well described by the Monte Carlo data, but there are deviations in the low energy flow bins in fig. 7.9. Those discrepancies stem from the fact that the NLO corrections become important in these kinematic regions. We can understand this by looking at fig. 4.2. In those cases where we have a hole in the backward region of the acceptance, there is a possibility for a third jet to disappear undetected. The Rapgap Monte Carlo contains only leading order matrix elements and is thus only capable of producing a two jet event. Plots showing the energy, velocity, position and multiplicity of the two detected jets can be found in appendix D, from which it is obvious that the data is well reproduced by the Monte Carlo sample.

7.5 Average $\cos\phi^{*'}$ and average $\cos 2\phi^{*'}$ on detector level.

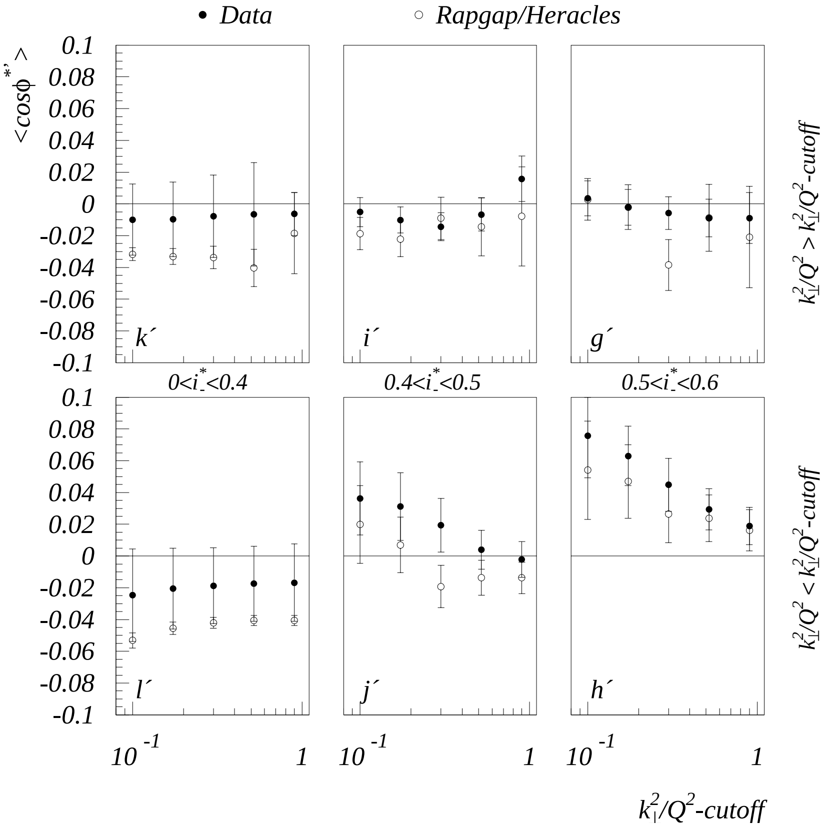

Figure 7.11: The average $\cos\phi^{*'}$ on detector level as a function of the $k_\perp^2/Q^2$-cutoff at low energy-flows. The error bars of the data points include both statistical and systematic errors.

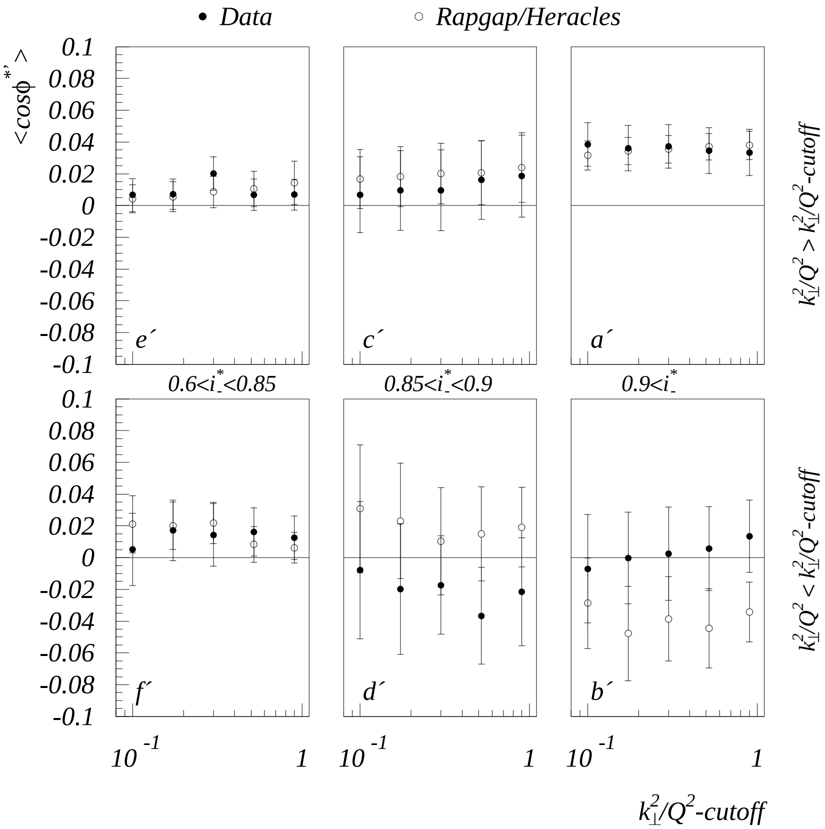

Figure 7.12: The average $\cos\phi^{*'}$ on detector level as a function of the $k_\perp^2/Q^2$-cutoff at high energy-flows. The error bars of the data points include both statistical and systematic errors.

We now turn to the final measurement of the azimuthal asymmetries and start by plotting the average $\cos\phi^{*'}$ in figs. 7.11-7.12 and the average $\cos 2\phi^{*'}$ in figs. 7.13-7.14 as a function of the cutoff variable. The averages have been calculated in two different ways: By fitting the function $f(\phi^{*'}) = a_0 + a_1\cos\phi^{*'} + a_2\cos 2\phi^{*'}$ to the experimental data and calculating the averages from the expressions $\langle\cos\phi^{*'}\rangle = a_1/2a_0$ and $\langle\cos 2\phi^{*'}\rangle = a_2/2a_0$, and by simply calculating the average value of the measured $\cos\phi^{*'}$ and $\cos 2\phi^{*'}$ distributions. No significant devi-

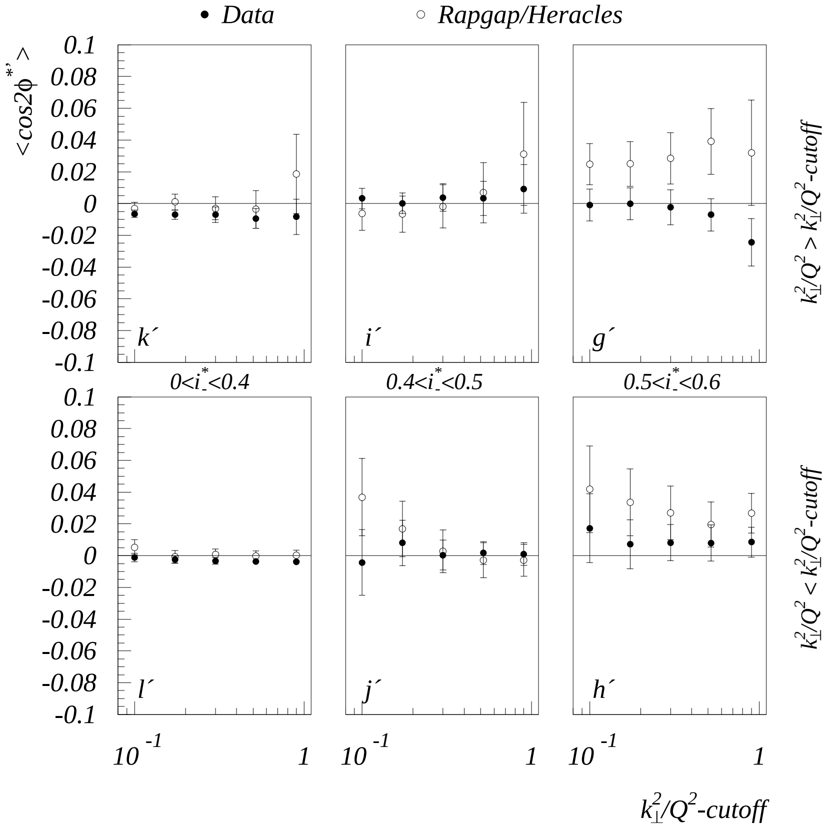

Figure 7.13: The average $\cos 2\phi^{*'}$ on detector level as a function of the $k_\perp^2/Q^2$-cutoff at low energy-flows. The error bars of the data points include both statistical and systematic errors.

ation could be observed between the two methods. We also calculated $\langle\cos 3\phi^{*'}\rangle$ as well as $\langle\sin\phi^{*'}\rangle$, but no significant signal could be observed, which is consistent with expectations.

We see that the data in the bins of high energy flow, fig. 7.12 and fig. 7.14, are persistently well described and that there are systematic deviations in the bins l' and k' of fig. 7.11. The deviations may come from a number of different sources. The first possibility which has to be considered is the description of the detector performance in the sim-

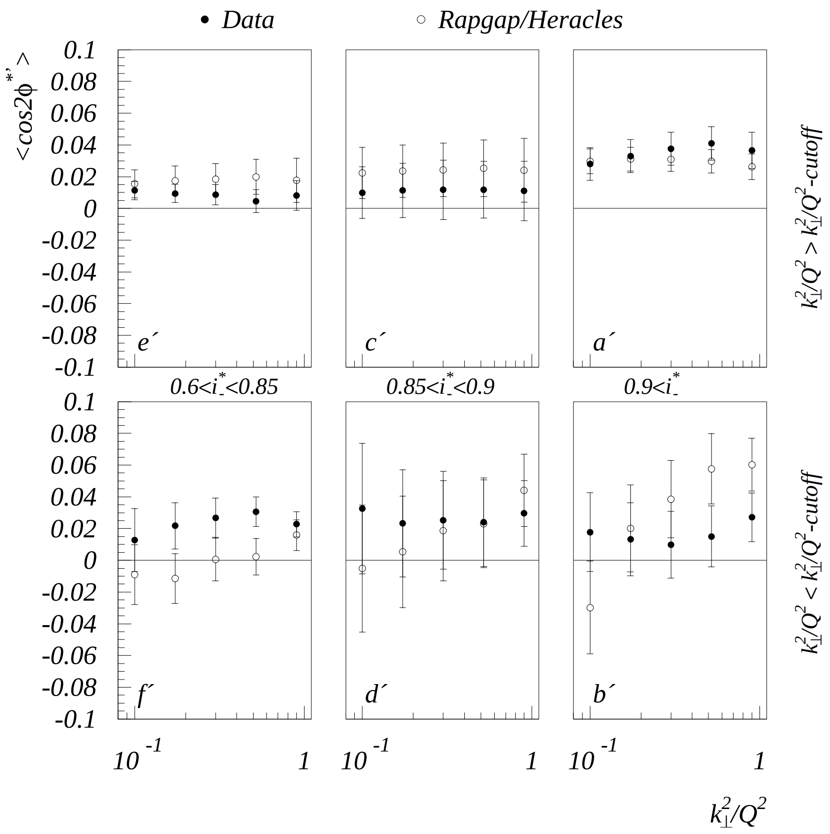

Figure 7.14: The average $\cos 2\phi^{*'}$ on detector level as a function of the $k_\perp^2/Q^2$-cutoff at high energy-flows. The error bars of the data points include both statistical and systematic errors.

ulation program. The SPACAL has been in operation a much shorter period of time than the LAr calorimeter and therefore the experience with the SPACAL is much poorer, which means a worse understanding of its properties.

QED effects as discussed in section 3.7 could be a possible source, since it was shown that the QED correction could amount to a $\langle\cos\phi^{*'}\rangle \approx -0.1$ effect (see fig. 3.4). The fact that we are using a kinematic method less sensitive to the QED radiation limits the effect to $\langle\cos\phi^{*'}\rangle \approx -0.05$

SPACAL had	7%
SPACAL elmagn	2%
LAr had	2%
LAr elmagn	2%
Tracks	3%

Table 7.1: The systematic errors from the uncertainty in the energy scales of the detector.

in bin l' of fig. 7.11, where we otherwise would not have expected any signal (see fig. 4.5). However, if the Heracles interface makes a slight overestimation of the QED corrections this would lead to the observed difference.

Higher order QCD effects as we discussed in the previous section can of course also play a role. The only thing which we probably can rule out is the intrinsic $p_\perp^*$ of the proton since it according to fig. 4.5 should produce a negative signal and thus would put the data below the Monte Carlo and not above.

It is, however, a complicated procedure to find out which of the possible sources, mentioned above, contribute to the deviations observed in bins k' and l' of fig. 7.11, and what the magnitude of the respective contributions are. Therefore we have chosen to include the difference between data and Monte Carlo in these bins into the systematic errors. This is a conservative estimate. A list of the other contributions to the systematic errors are specified in table 7.1.

7.6 Detector response.

The detector response has been discussed in chapter 6. The detector level data is related to the hadron level via a matrix, which describes the influence of the detector. The overall matrix plotted in fig. 7.15 relates bins in the energy flow variable on detector level to those on hadron level, for $k_\perp^2/Q^2 - cutoff = 0.3$. Each element in the overall matrix consists of a sub-matrix, which we denote $\mathbf{K}_{qq'}$, where $q = a, b, e, f, k, l$ and $q' = a'..l'$. Each of these sub-matrices can, with reference to eq. 6.25, be written as:

$$\mathbf{k} = \begin{pmatrix} k_{20} & k_{21} & k_{22} \\ k_{10} & k_{11} & k_{12} \\ k_{00} & k_{01} & k_{02} \end{pmatrix} \tag{7.1}$$

where the constants in eq. 6.25 has been absorbed into the elements. The element k_{11} in each sub-matrix gives the response for the $\cos\phi^*$

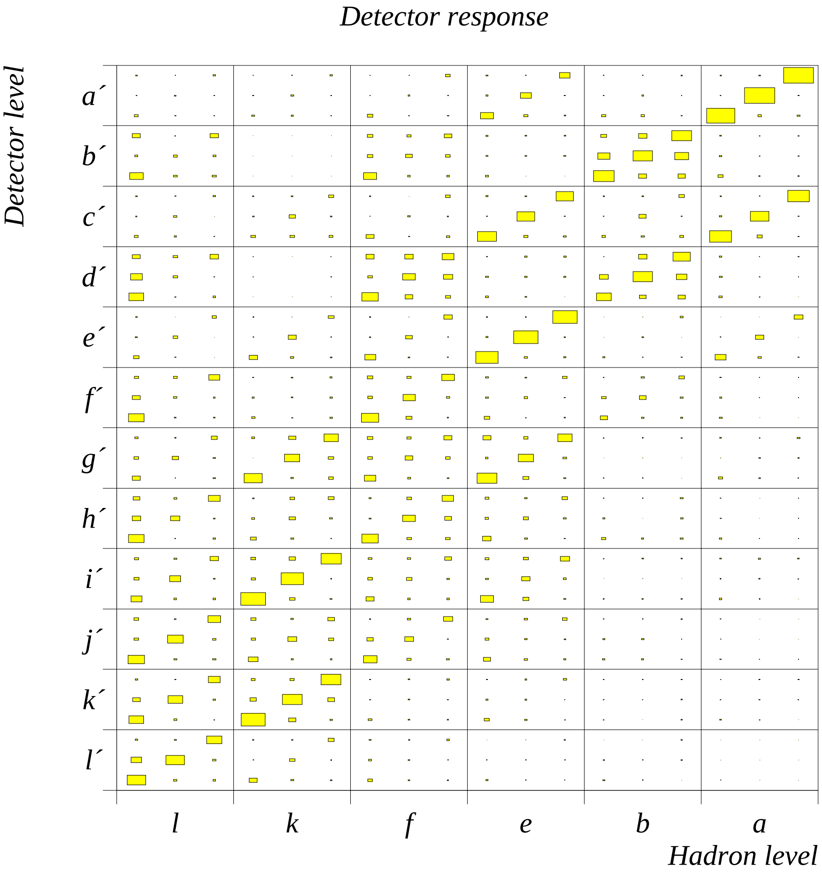

Figure 7.15: The detector response matrix at $k_\perp^2/Q^2 - cutoff = 0.3$. Each box contains 9 elements telling how the Fourier series $a_0 + a_1 \cos\phi^* + \cos 2\phi^*$ is transferred from hadron to detector level.

term and the element k_{22} gives the response for the $\cos 2\phi^*$ term. We see that there are 6x12 sub-matrices which each consists of 9 elements. The total matrix thus has 648 elements. The elements were determined for each sub-matrix by plotting $\phi^{*'}$ as measured on detector level versus ϕ^* as obtained on hadron level, and performing a two-dimensional fit to the Fourier expansions.

We first notice that the elements are concentrated along the diago-

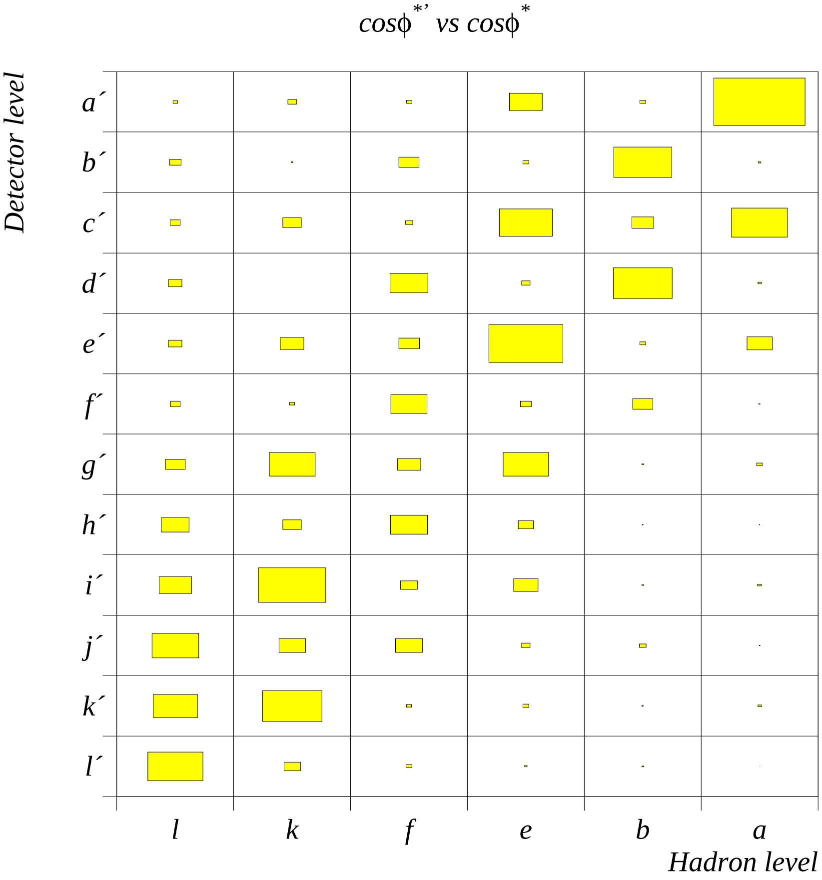

Figure 7.16: The detector response matrix for $\cos\phi^*$ term at $k_\perp^2/Q^2 - cutoff = 0.3$.

nal of the sub-matrices which means that the moments in the Fourier expansion on hadron level are dominantly transferred to the same moments on detector level. We have listed some important numbers in the detector response in table 7.2. The sub-matrix $\mathbf{K}_{aa'}$ describes the transformation between the high energy flow bins ($i_-^* > 0.9$) on detector and hadron level. As observed from the table the diagonal elements in that sub-matrix indicate a response of 60%. We also notice the smearing towards lower energy flows into the bins c' and e'. The migration the next

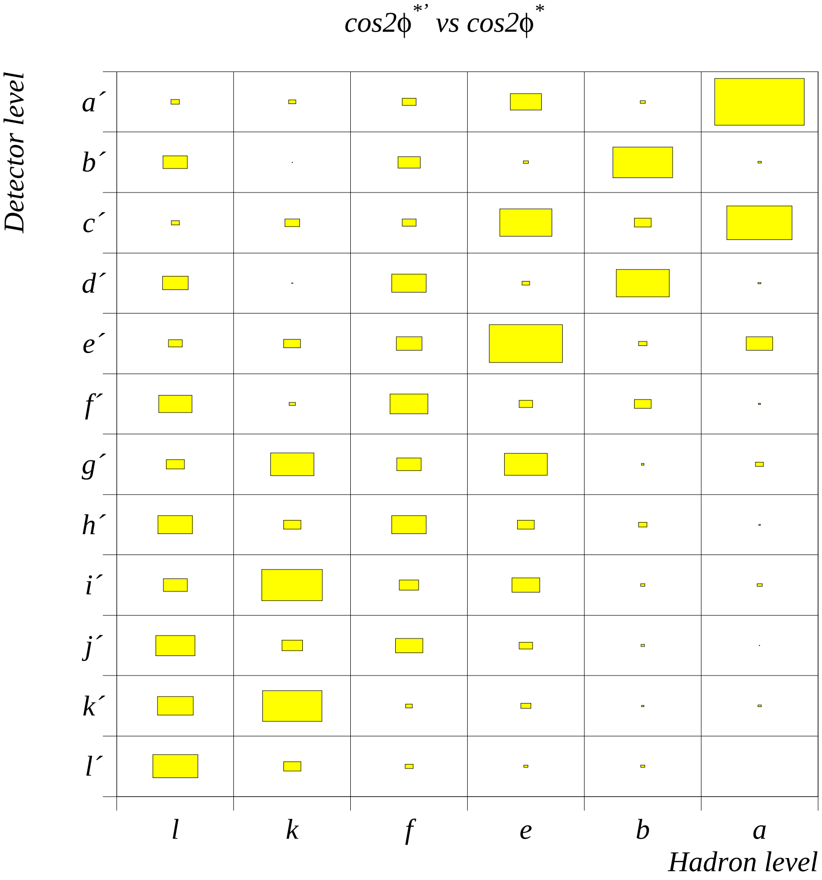

Figure 7.17: The detector response matrix for $\cos 2\phi^*$ term at $k_\perp^2/Q^2 - cutoff = 0.3$.

lower energy flow bin above the cutoff value, e, into bin a' is relatively small, which guarantees a clean sample in that bin.

In fig. 7.16 we have separated out the element $\mathbf{k}_{11}$ of each sub-matrix indicating how $\langle\cos\phi^*\rangle$ is transferred to $\langle\cos\phi^{*'}\rangle$ and fig. 7.17 shows the element $\mathbf{k}_{22}$ of each sub-matrix indicating how $\langle\cos 2\phi^*\rangle$ is transferred to $\langle\cos 2\phi^{*'}\rangle$. In these two plots we can more clearly study the smearing of the signal from bin a on hadron level over the detector level bins a', c' and e'. The lower energy flows in the bins c' and e' contain a mixture

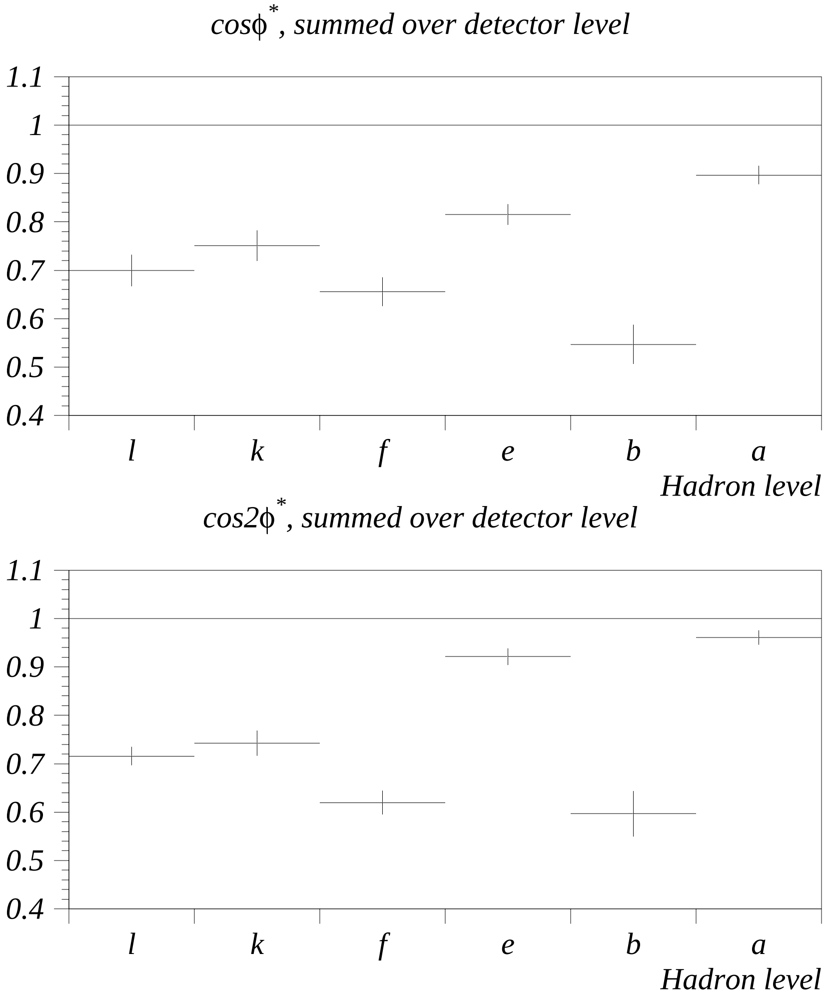

Figure 7.18: The response in the various energy flow bins on hadron level, after summation over detector level bins for $\cos\phi^*$ (top) and $\cos 2\phi^*$ (bottom), at $k_\perp^2/Q^2 - cutoff = 0.3$.

of events mainly from the bins a and e.

Finally we have performed a sum over the detector level bins in fig. 7.15 and these sums are displayed in fig. 7.18 for each of the hadron

a'		0.08	0.61
c'		0.20	0.23
e'	0.01	0.40	0.05
l'	0.22		
	l	e	a

a'		0.07	0.59
c'		0.20	0.31
e'	0.01	0.39	0.05
l'	0.15		
	l	e	a

Table 7.2: Some of the numbers from the detector response for $\cos\phi^*$, left, and for $\cos 2\phi^*$, right.

level bins. We notice that between 90% and 95% of the high energy flow signal is transferred to the detector level and the response is falling with the energy flow.

The detector response for other cutoff values is rather similar, the response in the high energy flow bin does not change significantly and stays at 90% for $\cos\phi^*$ and 95% for $\cos 2\phi^*$.

7.7 Unfolding the data to hadron level.

Cut	$k_\perp^2/Q^2$	χ^2	$\chi^2 - prob.$
1	0.10	11.17	0.89
2	0.17	12.18	0.84
3	0.30	12.18	0.84
4	0.52	9.50	0.95
5	0.90	8.36	0.97

Table 7.3: χ^2 for the unfolding using five different cutoff values.

Using the detector response matrix in the previous section we now unfold the measured asymmetries down to hadron level. We have chosen to use the χ^2-probability as quality measure of the unfolding. There are 12 energy flow bins on detector level each with the three measured moments a_0, a_1 and a_2. On hadron level we have 6 energy flow bins with three moments. This gives 12x3-6x3=18 degrees of freedom. In table 7.3 the χ^2 and the χ^2-probabilities are listed. The χ^2-probabilities are very high, varying between 0.84 and 0.97, stemming from the very conservative estimates of the systematic errors in the H1-detector.
Both detector and hadron level was normalized in each bin so that the

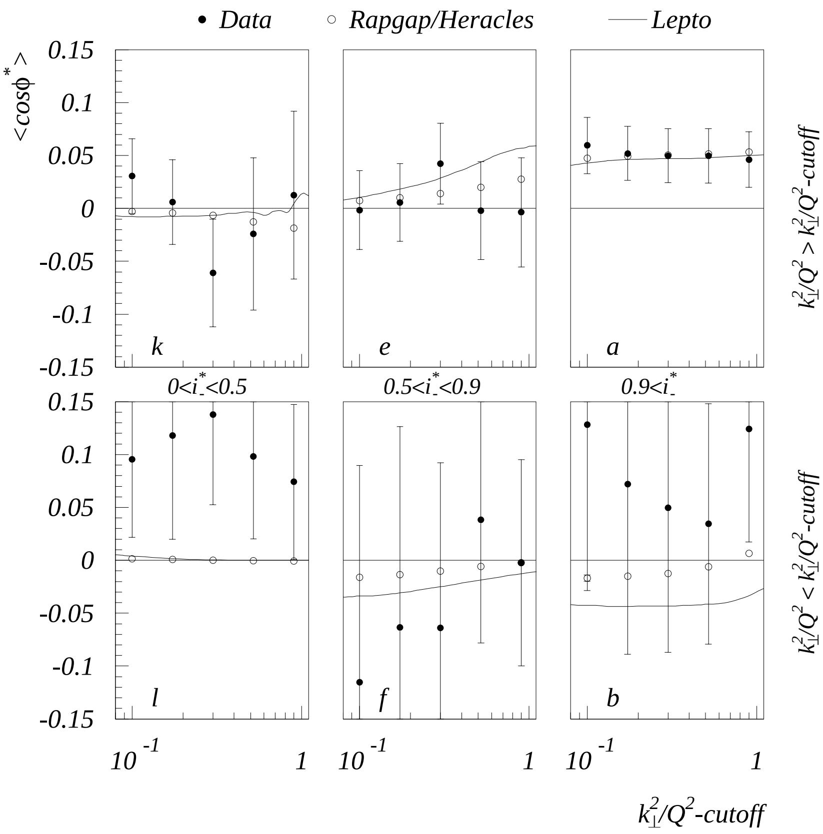

Figure 7.19: The average $\cos\phi^*$ unfolded to hadron level (filled circles), compared to the reference point from Rapgap (open circles) and curves from Lepto, as a function of the $k_\perp^2/Q^2$-cutoff at low energy-flows. The error bars belong to the data points. Note the different scale on the y-axis compared to previous plots.

functions had the form $f(\phi^*) = 1 + a_1 \cos\phi^* + a_2 \cos 2\phi^*$ on both hadron and detector level.

As a cross check the unfolding was performed twice, once with all three moments in the unfolding and once with only the two higher moments. Both unfoldings gave consistent results.

As a further check we initiated the unfolding with three different

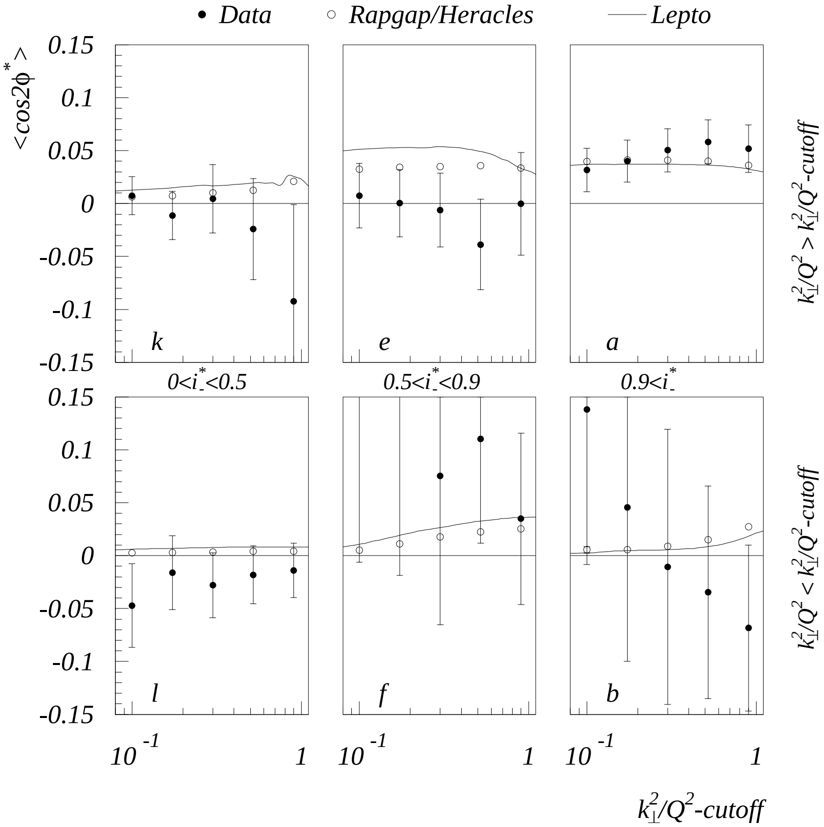

Figure 7.20: The average $\cos 2\phi^*$ unfolded to hadron level (filled circles), compared to the reference point from Rapgap (open circles) and curves from Lepto, as a function of the $k_\perp^2/Q^2$-cutoff at low energy-flows. The error bars belong to the data points. Note the different scale on the y-axis compared to previous plots.

starting values, namely by giving the parameters used in the unfolding procedure the values from the Monte Carlo generator on hadron level, by setting the parameters to zero, and by setting them to unity. All three runs gave consistent results.

The results for $\langle \cos\phi^* \rangle$ and $\langle \cos 2\phi^* \rangle$ on hadron level are plotted in figs. 7.19-7.20, together with the reference points from Rapgap and the curves from Lepto. The high energy flows are perfectly described for both $\langle\cos\phi^*\rangle$ and $\langle\cos 2\phi^*\rangle$. The average $\cos\phi^*$ for the data in bin l is one sigma above the Monte Carlo predictions, consistent with the signal on detector level.

Comparing Rapgap and Lepto we see that they are consistent for the important high energy flows for $k_\perp^2/Q^2 > k_\perp^2/Q^2 - cutoff$. The deviations seen at lower energy flows stem from the fact that in Rapgap we have the parton showers switched on whereas they were switched off in Lepto. Secondly they have a different cutoff scheme for the matrix element where Rapgap uses a cutoff $p_\perp^{*2} > 2.5\,GeV^2$ and Lepto a two dimensional cutoff $\hat{s} > 4\,GeV^2$ and $min(z, 1-z) > 0.04$.

7.8 Final result.

The final results are presented in fig. 7.21 as the average $\cos\phi^*$ and the average $\cos 2\phi^*$ versus $k_\perp^2/Q^2$-cutoff for $i_-^* > 0.9$ and $k_\perp^2/Q^2 > k_\perp^2/Q^2 - cutoff$. The data points are 1.5-2 standard deviations above zero, and are consistent with a pure gluon signal for both leading and next to leading order calculations.

The large errors stem from the migrations in the detector response. In order to reduce the error bars one would have to find a way to unfold the data which is less sensitive to the migrations.

By looking in a very constrained kinematic region we are able to isolate signals on $\langle\cos\phi^*\rangle$ and $\langle\cos 2\phi^*\rangle$ which are consistent with QCD. The interesting extension of the analysis is now to cover the region of small x_B and Q^2, where multiple gluon exchange might contribute to the DIS cross section. This can be investigated by a measurement of the azimuthal asymmetries which determines the exchanged spin.

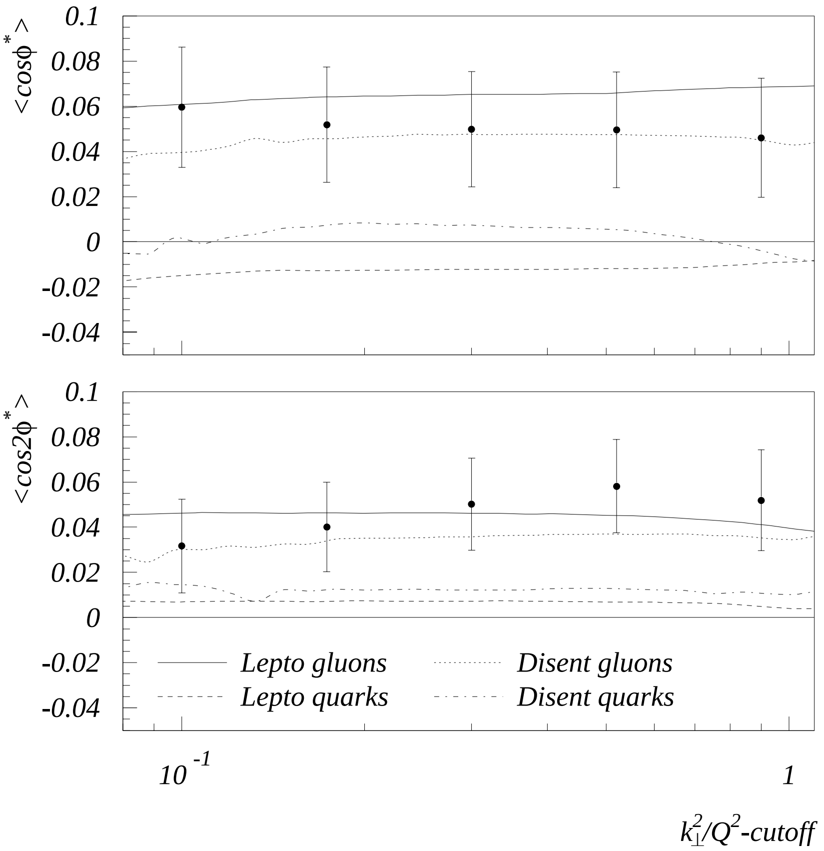

Figure 7.21: The average $\cos\phi^*$ (top) and $\cos 2\phi^*$ (bottom) as a function of the $k_\perp^2/Q^2$-cutoff for $k_\perp^2/Q^2 > k_\perp^2/Q^2{-}cutoff$ and $k_\perp^2/Q^2 < k_\perp^2/Q^2{-}cutoff$, bin a in figs. 7.19-7.20. The data is compared to the Lepto predictions for gluon initiated (full lines) and quark initiated (dashed lines) processes, and to NLO predictions (Disent) for gluon initiated (dotted lines) and quark initiated (dash-dotted lines) processes.

A

The Breit frame.

A.1 Introduction.

In this appendix we define the Breit frame and, as was stated in section 2.4, list the expressions for the four-vectors of the leptons and partons participating in the DIS process. We provide formulas for both zeroth and leading order processes in α_s.

A.2 Definition of the Breit frame.

The frame is so defined that the exchanged virtual photon is purely space-like, with the proton and photon colliding head on along the z-axis. We let the proton define the positive z-direction, which then gives the four-momenta of the photon, q, and proton, P, as:

$$q \equiv \left(0, 0, 0, -\sqrt{Q^2}\right) \tag{A.1}$$

$$P \equiv \frac{\sqrt{Q^2}}{2\,x_B}\,(1, 0, 0, 1) \tag{A.2}$$

A.3 Expressions for the leptons.

Looking at the expression for the photon above we recognize that since the photon four-momentum is the difference between the lepton four-momenta, $q = e - e'$, the energy and transverse momenta of the leptons have to be identical in order to cancel each other. The fact that the energies and transverse momenta are equal means that also the z components have to be identical in magnitude. We position the leptons in the x-z plane.

$$e = \left(\frac{\sqrt{Q^2}(2 - y_B)}{2\,y_B}, \frac{\sqrt{Q^2(1 - y_B)}}{y_B}, 0, -\frac{\sqrt{Q^2}}{2}\right) \tag{A.3}$$

$$e' = \left(\frac{\sqrt{Q^2}(2-y_B)}{2\,y_B}, \frac{\sqrt{Q^2(1-y_B)}}{y_B}, 0, \frac{\sqrt{Q^2}}{2} \right) \tag{A.4}$$

A.4 Expressions for the incoming and scattered quark in a QPM process.

In the Breit frame a QPM process is defined such that the four- momenta of the incoming (p_i) and scattered (p_f) quarks are of the same magnitude but oppositely directed along the z-axis. This has led to the nick-name "the brick-wall frame" for the Breit system.

$$p_i = \frac{\sqrt{Q^2}}{2}\,(1,0,0,1) \tag{A.5}$$

$$p_f = -\frac{\sqrt{Q^2}}{2}\,(1,0,0,1) \tag{A.6}$$

A.5 Expressions for the incoming parton and the two scattered partons in a leading order α_s process.

In a leading order α_s process the four-vector of the incoming parton, v_i^*, can be written:

$$v_i^* = \frac{p_\perp^{*2} + Q^2 z(1-z)}{2z(1-z)\sqrt{Q^2}}\,(1,0,0,1)\,. \tag{A.7}$$

To formulate the fourvectors of the scattered partons we need to define a partonic scaling variable z:

$$z = \frac{v_i \cdot v_2}{v_i \cdot q}. \tag{A.8}$$

The four-vector, v_2^*, associated with z can then be written as:

$$v_2^* = \left(\frac{p_\perp^{*2} + Q^2 z^2}{2z\sqrt{Q^2}}, p_\perp^* \cos\phi^*, p_\perp^* \sin\phi^*, \frac{p_\perp^{*2} - Q^2 z^2}{2z\sqrt{Q^2}} \right). \tag{A.9}$$

Using the above expressions the four-vector of the other final state parton, v_1^* can be calculated from momentum conservation:

$$v_1^* = \left(\frac{p_\perp^{*2} + Q^2(1-z)^2}{2(1-z)\sqrt{Q^2}}, -p_\perp^* \cos\phi^*, -p_\perp^* \sin\phi^*, \frac{p_\perp^{*2} - Q^2(1-z)^2}{2(1-z)\sqrt{Q^2}} \right). \tag{A.10}$$

B

The LO matrix element.

B.1 Introduction.

Complete expressions for the factors which enter the formulae of the leading order cross section given in section 2.5 and the approximate formulae specified in section 2.6.

B.2 The exact expressions.

The exact factors in eq. 2.32 for BGF are:

$$\begin{aligned} b_0 &= y_B^2(2\,(e_0^{*2}+e_z^{*2})(v_{z1}^{*2}+v_{z2}^{*2}+p_\perp^{*2})+4\,e_\perp^{*2}p_\perp^{*2}) \\ &= (1+(1-y_B)^2)\,Q^2(v_{z1}^{*2}+v_{z2}^{*2}+p_\perp^{*2})+ \\ &\qquad 2\,(1-y)\,2Q^2p_\perp^{*2} \qquad \text{(B.1)} \\ b_1 &= -4y_B^2\,e_0^*e_\perp^*(v_{02}^*-v_{01}^*)p_\perp^* \\ &= -(2-y_B)\sqrt{1-y_B}\;2Q^2(v_{02}^*-v_{01}^*)p_\perp^* \qquad \text{(B.2)} \\ b_2 &= y_B^2 2\,e_\perp^{*2}p_\perp^{*2} \\ &= 2\,(1-y_B)\,Q^2p_\perp^{*2}, \qquad \text{(B.3)} \end{aligned}$$

and the corresponding factors for QCD Compton in eq. 2.35 are:

$$\begin{aligned} c_0 &= y_B^2(2\,(e_0^{*2}+e_z^{*2})(v_{zi}^{*2}+v_{z2}^{*2}+\frac{1}{2}p_\perp^{*2})+2\,e_\perp^{*2}p_\perp^{*2}) \\ &= (1+(1-y_B)^2)\,Q^2(v_{zi}^{*2}+v_{z2}^{*2}+\frac{1}{2}p_\perp^{*2})+ \\ &\qquad 2\,(1-y)\,Q^2p_\perp^{*2} \qquad \text{(B.4)} \\ c_1 &= -4y_B^2\,e_0^*e_\perp^*v_{02}^*p_\perp^* \\ &= -(2-y_B)\sqrt{1-y_B}\;2Q^2v_{02}^*p_\perp^* \qquad \text{(B.5)} \\ c_2 &= y_B^2e_\perp^{*2}p_\perp^{*2} \\ &= 2\,(1-y_B)\,Q^2\frac{p_\perp^{*2}}{2}. \qquad \text{(B.6)} \end{aligned}$$

B.3 Expressions in the collinear limit.

The explicit expressions for the D functions in eqs. 2.44-2.46 are:

$$D_R = \frac{4x_p(1-x_p)f_g + \frac{16}{3}x_p \sum_q f_q}{\frac{1}{2}\frac{x_p}{1-x_p}(x_p^2+(1-x_p)^2)f_g + \frac{4}{3}\frac{1+x_p^2}{x_p}\sum_q f_q} \tag{B.7}$$

$$D_1 = -2\frac{(1-x_p)(2x_p-1)f_g + \frac{8}{3}x_p \sum_q f_q}{\frac{1}{2}\frac{x_p}{1-x_p}(x_p^2+(1-x_p)^2)f_g + \frac{4}{3}\frac{1+x_p^2}{x_p}\sum_q f_q} \tag{B.8}$$

$$D_2 = \frac{2x_p(1-x_p)f_g + \frac{8}{3}x_p \sum_q f_q}{\frac{1}{2}\frac{x_p}{1-x_p}(x_p^2+(1-x_p)^2)f_g + \frac{4}{3}\frac{1+x_p^2}{x_p}\sum_q f_q} \tag{B.9}$$

C

Details on the Monte Carlo models used.

C.1 Introduction.

We will in this appendix just list the features in the different Monte Carlos which was set at a *non-default* value. The structure function parametrized according to CTEQ-4M was implemented in all cases, and Q^2 was used as scale.

C.2 Lepto.

Since parton-showers are not generated taking the azimuthal asymmetries into account, they were switched off ($LST(8) = 1$). Furthermore the soft colour interaction ($LST(35) = 0$), and the new remnant treatment were taken out($LST(14) = 0$).

In the cases were the default version were used the intrinsic $p_\perp^*$ was set to zero ($PARL(9) = 0$).

In the modified version developed in chapter 3 everything was kept as above, and the intrinsic $p_\perp^*$ was steered through the lepto parameter ($PARL(9)$).

C.3 Disent.

Disent was used in its default version without changing any parameters.

C.4 Rapgap/Heracles.

Rapgap/Heracles was used with two different settings, one where the radiative corrections on the leptons was included and one where they where switched off.

These sets of events were produced for common use by the whole H1 community and most features were therefore included.

The process generation was set to normal DIS, without any contribution from resolved photon processes. Therefore Q^2 was the natural choise of scale in the structure function and in α_s. The ${p_\perp^*}^2$ cutoff in the leading order matrix elements was set to $2.5\,GeV^2$.

As diffractive structure function a fit to the H1 data from 1994 was used.

D

Control plots on detector level.

D.1 Introduction.

We will here present the control plots which have been used to ensure that the Monte Carlo model Rapgap gives an accurate description of the data. The key variables we have chosen are the energy, velocity, rapidity and multiplicity of the backward jet. The mean values and RMS spread of all four variables will be presented for all six detector-level bins of the energy flow, both below and above the $k_{\perp}^2/Q^2$-cutoff.

D.2 The energy distribution.

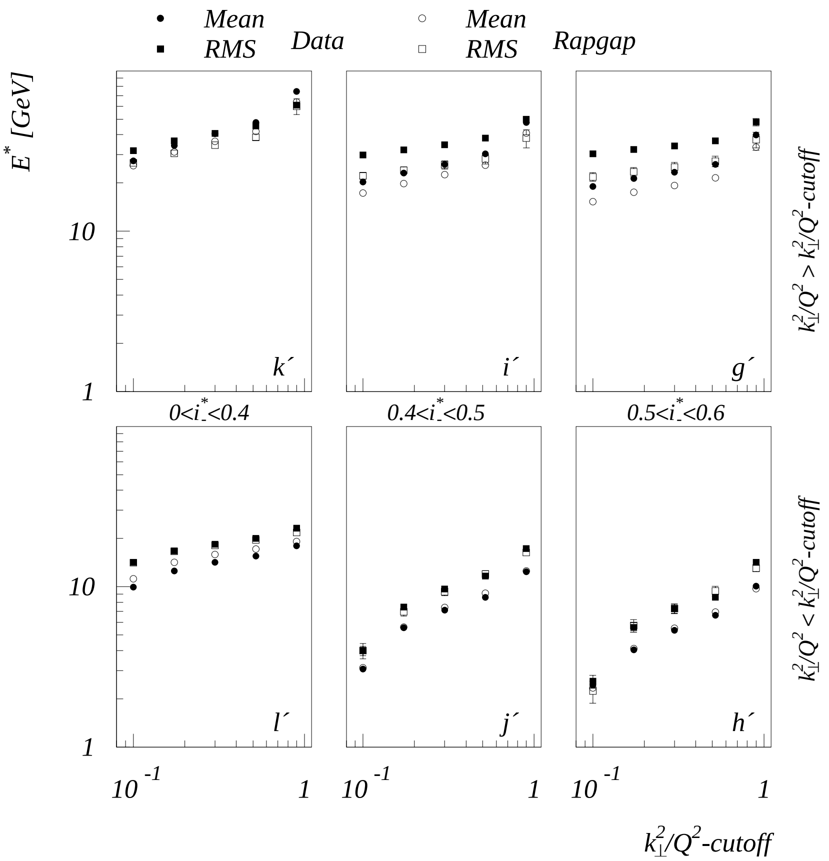

Figure D.1: The mean value and RMS spread in the energy of the backward jet as a function of the $k_\perp^2/Q^2$-cutoff at low energy-flows.

The energy of the backward jet as measured in the Breit system is plotted on detector level in fig. D.1 for low energy-flows and in fig. D.2 for high energy flows.

The only regions where any significant difference can be observed are in the bins i', g', e', c'. These are regions with medium energy flow, $0.4 < i_-^* < 0.9$, above the $k_\perp^2/Q^2$-cutoff. The Monte Carlo gives a mean

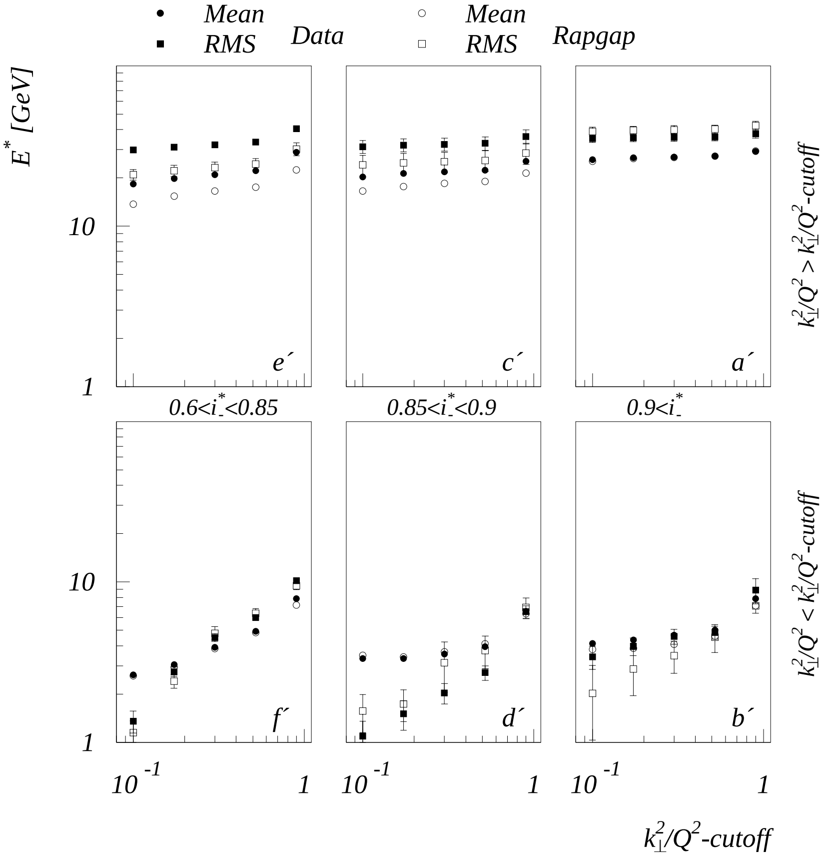

Figure D.2: The mean value and RMS spread in the energy of the backward jet as a function of the $k_\perp^2/Q^2$-cutoff at high energy-flows.

value and an RMS spread which are between 1% and 5% lower than the data. The for us most important bin, a', is very well described.

D.3 The β distribution.

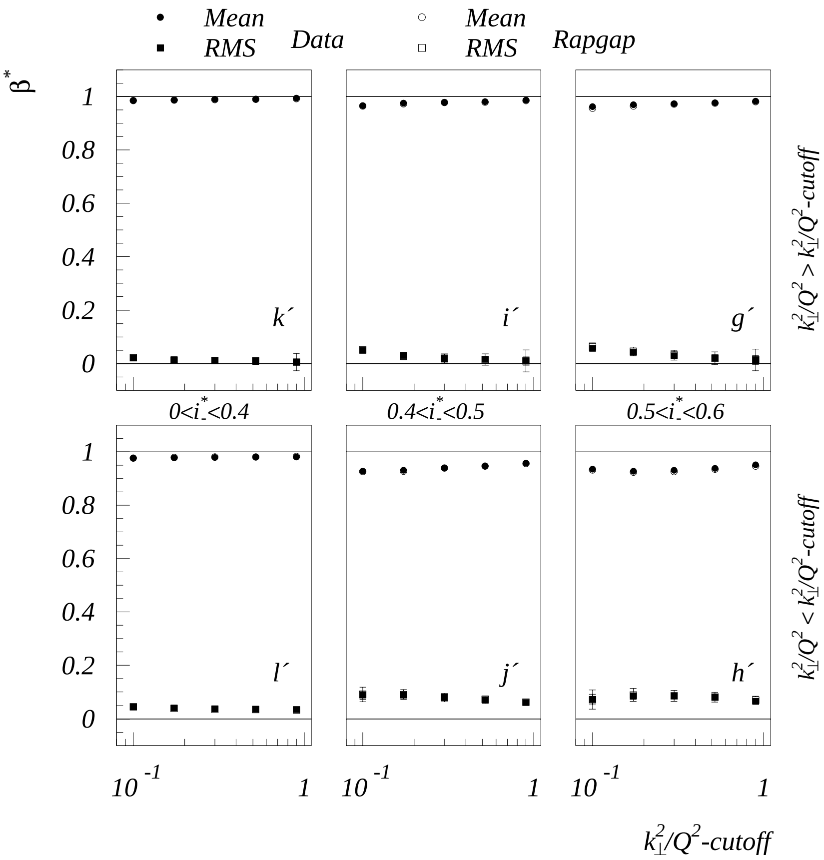

Figure D.3: The mean value and RMS spread in β^* of the backward jet as a function of the $k_\perp^2/Q^2$-cutoff at low energy-flows.

The velocity of the backward jet, defined as $\beta^* = P^*/E^*$, is shown on detector level in figs. D.3-D.4 as a function of the $k_\perp^2/Q^2$-cutoff . No difference between the data and Monte Carlo can be observed. In those cases where only one filled circle or square can be seen the Monte Carlo and the data points are overlapping.

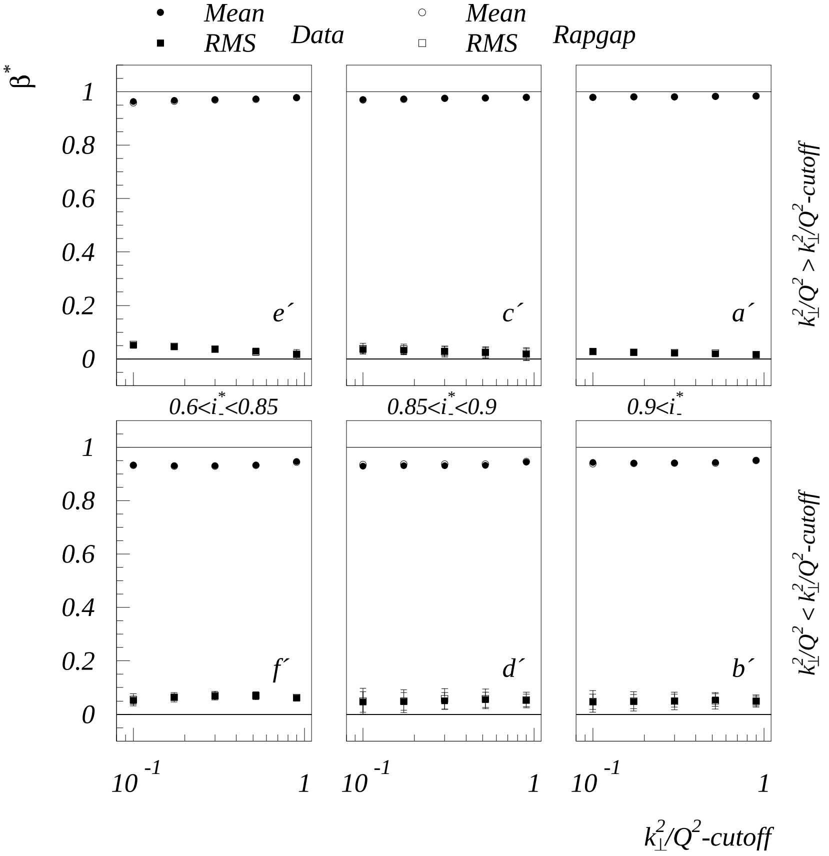

Figure D.4: The mean value and RMS spread in β^* of the backward jet as a function of the $k_\perp^2/Q^2$-cutoff at high energy-flows.

D.4 The rapidity distribution.

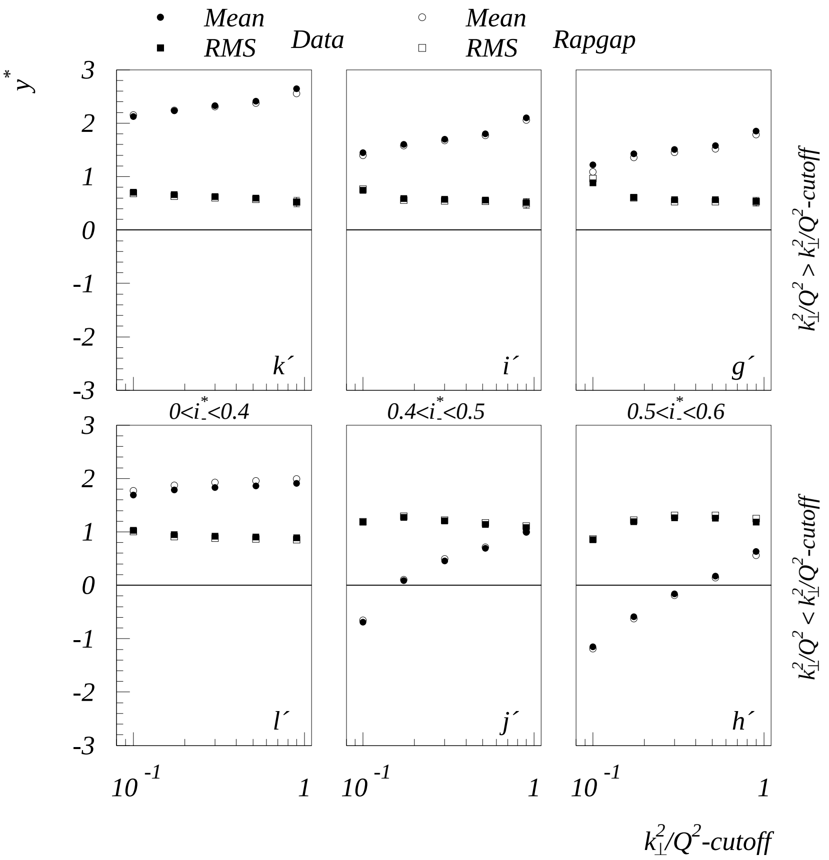

Figure D.5: The mean value and RMS spread in the rapidity of the backward jet as a function of the $k_\perp^2/Q^2$-cutoff at low energy-flows.

The rapidity of the backward jet on detector level is shown in figs. D.5-D.6 as a function of the $k_\perp^2/Q^2$-cutoff . No significant difference between the data and Monte Carlo can be observed in any bin.

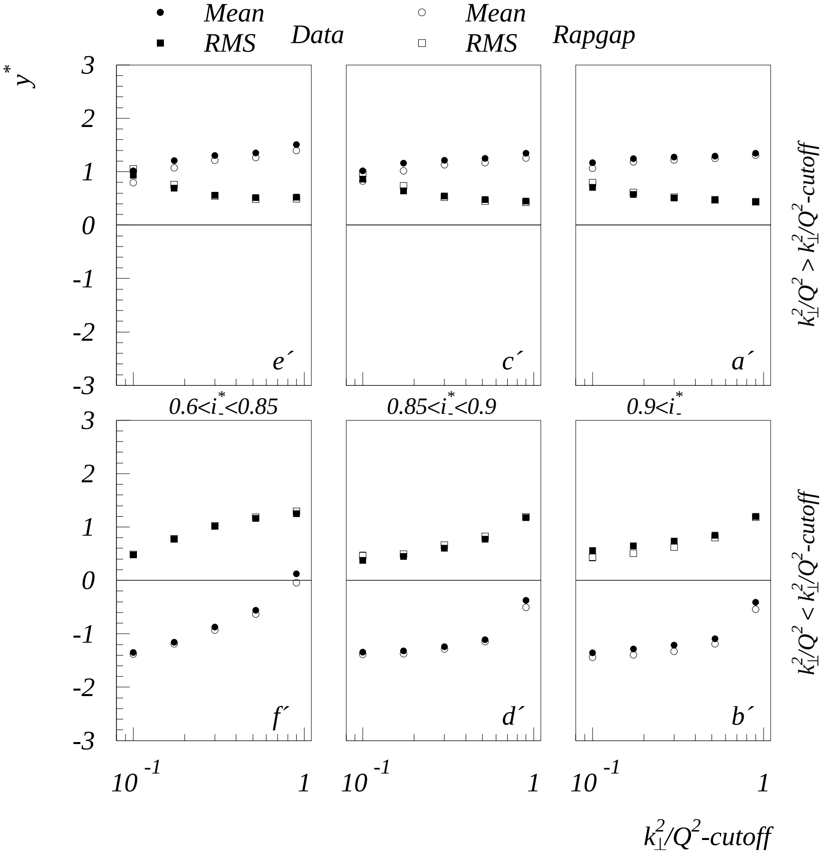

Figure D.6: The mean value and RMS spread in the rapidity of the backward jet as a function of the $k_\perp^2/Q^2$-cutoff at high energy-flows.

D.5 The multiplicity.

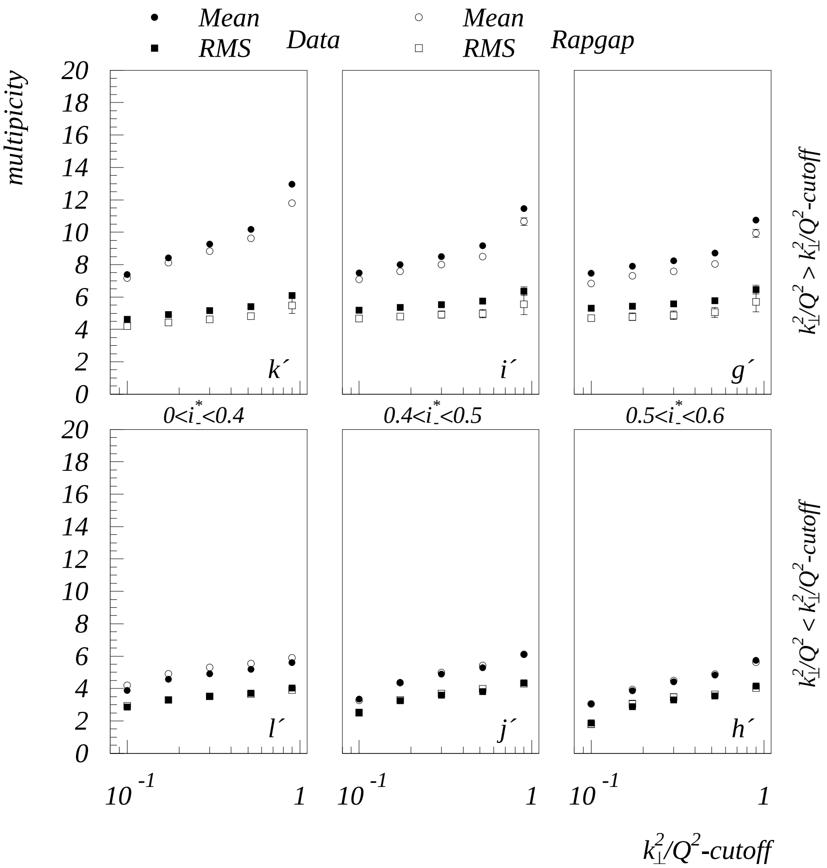

Figure D.7: The mean value and RMS spread in the multiplicity of the backward jet as a function of the $k_\perp^2/Q^2$-cutoff at low energy-flows.

The number of measured four-vectors clustered on detector level to obtain the backward jet, abbreviated multiplicity, is shown in figs. D.7-D.8 as a function of the $k_\perp^2/Q^2$-cutoff . The only regions where any significant difference can be observed are, just as for the energy distribution, the bins i', g', e', c'. These are the regions with medium energy flow, $0.4 < i^*_- < 0.9$, above the $k_\perp^2/Q^2$-cutoff. The mean value of the

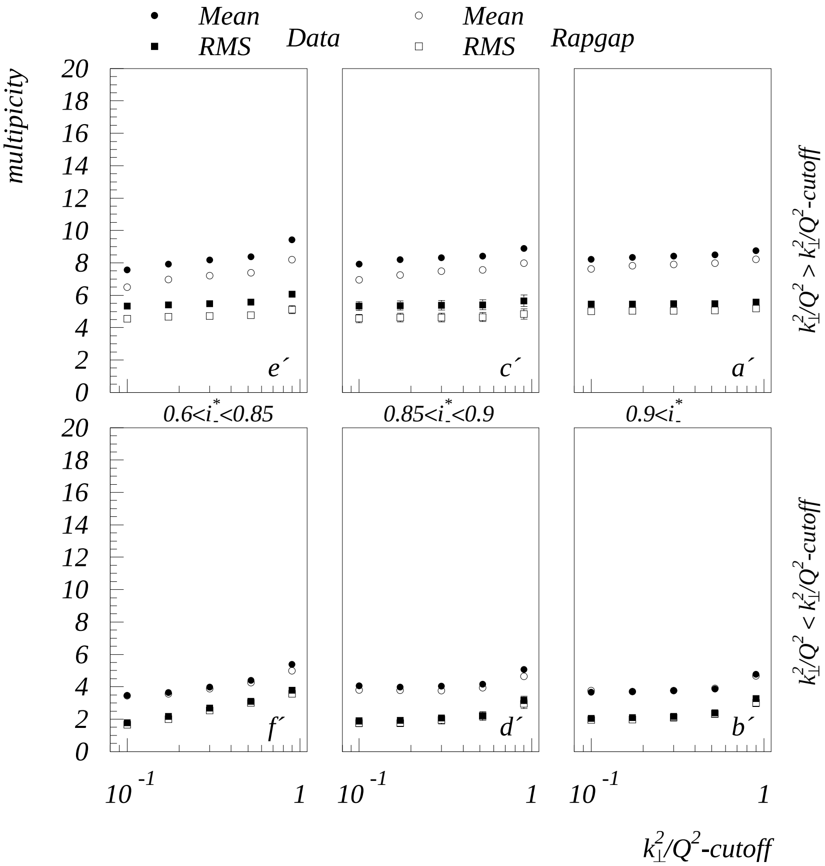

Figure D.8: The mean value and RMS spread in the multiplicity of the backward jet as a function of the $k_\perp^2/Q^2$-cutoff at high energy-flows.

hadron multiplicity in the Monte Carlo data is, in the worst case, one unit smaller than in the measured data and the RMS spread is 0.5 units smaller.

D.6 Conclusions.

The Rapgap Monte Carlo model gives an accurate description of the jets, which gives us confidence in using it for calculating corrections due to detector effects.

Bibliography

Abt, I. et al. (1997), 'The H1 detector at HERA. (Updated version)', *Nucl. Instrum. Meth.* **A386**, 310–396.

Adams, M. R. et al. (1993), 'Perturbative QCD effects observed in 490-GeV deep inelastic muon scattering', *Phys. Rev.* **D48**, 5057–5066.

Arneodo, M. et al. (1987), 'Measurement of hadron azimuthal distributions in deep inelastic muon proton scattering', *Z. Phys.* **C34**, 277.

Bartels, J., Ewerz, C., Lotter, H., Wusthoff, M. & Diehl, M. (1995), 'Quark - anti-quark jets in DIS diffractive dissociation'.

Bassler, U. & Bernardi, G. (1999), 'Structure function measurements and kinematic reconstruction at HERA', *Nucl. Instrum. Meth.* **A426**, 583–598.

Blobel, V. (1984), 'Unfolding methods in high-energy physics experiments', in *CERN Comp.School*, CERN. DESY preprint 84-118.

Boer, D., Jakob, R. & Mulders, P. J. (1999), 'Angular dependences in electroweak semiinclusive leptoproduction', hep-ph/9907504.

Cahn, R. N. (1978), 'Azimuthal dependence in lepto-production: A simple parton model calculation', *Phys. Lett.* **78B**, 269.

Cahn, R. N. (1989), 'Critique of parton model calculations of azimuthal dependence in lepto-production', *Phys. Rev.* **D40**, 3107.

Callan, C. G. & Gross, D. J. (1969), 'High-energy electroproduction and the constitution of the electric current', *Phys. Rev. Lett.* **22**, 156–159.

Catani, S., Dokshitzer, Y. L. & Webber, B. R. (1992), 'The $k_\perp$-clustering algorithm for jets in deep inelastic scattering and hadron collisions', *Phys. Lett.* **B285**, 291–299.

Catani, S., Dokshitzer, Y. L. & Webber, B. R. (1994), ‘Average number of jets in deep inelastic scattering’, *Phys. Lett.* **B322**, 263–269.

Catani, S. & Seymour, M. H. (1997), ‘A general algorithm for calculating jet cross sections in NLO QCD’, *Nucl. Phys.* **B485**, 291–419.

Charchula, K., Schuler, G. A. & Spiesberger, H. (1994), ‘Combined QED and QCD radiative effects in deep inelastic lepton - proton scattering: The Monte Carlo generator DJANGO6’, *Comput. Phys. Commun.* **81**, 381–402.

Chay, J., Ellis, S. D. & Stirling, W. J. (1991), ‘Azimuthal asymmetry in lepton - photon scattering at high- energies’, *Phys. Lett.* **B269**, 175–182.

Chay, J., Ellis, S. D. & Stirling, W. J. (1992), ‘Azimuthal asymmetry in lepton - photon scattering at high- energies’, *Phys. Rev.* **D45**, 46–54.

Dakin, J. T. et al. (1972), ‘Measurement of the inclusive electroproduction of hadrons’, *Phys. Rev. Lett.* **29**, 746.

Ellis, R. K., Stirling, W. J. & Webber, B. R. (1996), *QCD and collider physics*, Vol. 8 of *Cambridge monographs on particle physics, nuclear physics and cosmology*, Cambridge Univ. Pr.

Hagiwara, K., Hikasa, K. & Kai, N. (1983), ‘Time reversal odd asymmetry in semi-inclusive lepto-production in quantum chromodynamics’, *Phys. Rev.* **D27**, 84.

Halzen, F. & Martin, A. D. (1984), *Quarks and leptons: An introductory course in modern particle physics*, Wiley.

Ingelman, G., Edin, A. & Rathsman, J. (1997), ‘LEPTO 6.5: A Monte Carlo generator for deep inelastic lepton - nucleon scattering’, *Comput. Phys. Commun.* **101**, 108–134.

Jacobsson, C. (1994), Jet azimuthal angle asymmetries in deep inelastic scattering as a test of QCD, PhD thesis, Lunds universitet.

John E. Dennis, J. & Schnabel, R. B. (1996), *Numerical methods for optimization and nonlinear equations*, Classics in applied mathematics, Society for Industrial and Applied Mathematics (SIAM).

Jones, H. F. (1965), 'Pion-nucleon resonances and the angular distribution in pion electroproduction', *Nuovo Cim.* **40**, 1018.

Jung, H. (1995), 'Hard diffractive scattering in high-energy e p collisions and the Monte Carlo generator RAPGAP', *Comp. Phys. Commun.* **86**, 147–161.

Knowles, I. G. (1988), 'Angular correlations in QCD', *Nucl. Phys.* **B304**, 767.

König, A. & Kroll, P. (1982), 'A realistic calculation of the azimuthal asymmetry in semi-inclusive deep inelastic scattering', *Z. Phys.* **C16**, 89.

Kramer, G. (2000), Private communication.

Kwiatkowski, A., Spiesberger, H. & Mohring, H. J. (1992), 'HERACLES: An event generator for e p interactions at HERA energies inclusing radiative processes: version 1.0', *Comp. Phys. Commun.* **69**, 155–172.

Levelt, J. & Mulders, P. J. (1994), 'Quark correlation functions in deep inelastic semiinclusive processes', *Phys. Rev.* **D49**, 96–113.

Mulders, P. J. & Tangerman, R. D. (1996), 'The Complete tree level result up to order 1/Q for polarized deep inelastic leptoproduction', *Nucl. Phys.* **B461**, 197–237.

Plehn, T. (1998), Private communication.

Press, W. H., Teukolsky, S. A., Vetterling, W. T. & Flannery, B. P. (1992), *Numerical recipes in Fortran*, second edn, Cambridge Univ. Pr.

Ravndal, F. (1973), 'On the azimuthal dependence of semi-inclusive deep inelastic electro-production cross sections', *Phys. Lett.* **43B**, 301–303.

Seymour, M. H. (1995), 'A Simple prescription for first order corrections to quark scattering and annihilation processes', *Nucl. Phys.* **B436**, 443–460.

Sjöstrand, T. (1994), 'High-energy physics event generation with PYTHIA 5.7 and JETSET 7.4', *Comput. Phys. Commun.* **82**, 74–90.